

Master Thesis

Design and Analysis of Superresolution Algorithm and Signal Separation Technique for an OFDM-based MIMO Radar

Thanh Thuy Nguyen

Advisor: Prof. Dr. -Ing. Thomas Zwick

Prof. Dr. Antonio Broquetas

Supervisor: M.Sc. Yoke Leen Sit

Period: 01.05.2012 – 31.10.2012

Karlsruhe, 31.10.2012

Postanschrift: Institut für Hochfrequenztechnik und Elektronik
Kaiserstraße 12
D-76131 Karlsruhe

Gebäude: Engesserstraße 5, Geb. 30.10

Tel.: +49 (0) 721 608 4 2522
Schr.: +49 (0) 721 608 4 2523
Fax: +49 (0) 721 608 4 5027
E-Mail: info@ihe.kit.edu
Web: www.ihe.kit.edu



Declaration

I hereby declare that I wrote my Master Thesis on my own and that I have followed the regulations relating to good scientific practice of the Karlsruhe Institute of Technology (KIT) in its latest form. I did not use any unacknowledged sources or means and I marked all references I used literally or by content.

Karlsruhe, 31.10.2012

Thanh Thuy Nguyen

Abstract

Recently, the concept of MIMO (multiple-input multiple-output) radar has been proposed. MIMO radar has the capability to transmit orthogonal (or incoherent) waveforms at multiple transmit antennas. It offers promising potentials for resolution enhancement, interference suppression and against multipath fading. Many research about MIMO radar in signal processing have been conducted. However, the implementation of MIMO radar in practice is still uncommon. In this thesis, the SISO (single-input single-output) OFDM radar and communication system (RadCom), a previous project at Institut für Hochfrequenztechnik und Elektronik (IHE), KIT, Germany, is extended to MIMO configuration using the idea of spectrally interleaved multi-carrier signals to estimate the direction of arrival (DOA) of objects in 2D and 3D radar. The main aim of this thesis is to implement and evaluate a MIMO OFDM-based radar system.

The thesis consists of two parts, the software and hardware part. In the first part of the thesis, the MIMO radar is studied. A signal modeling is derived along with the analysis of suitable antenna geometries for 2D and 3D radar. The MIMO radar with the ability to form virtual array can increase significantly the resolution of DOA estimation. For that purpose, numerous algorithms based on different mathematical approaches exist. The numerical results show that the MUSIC (Multiple Signal Classification) algorithm based on subspace method is simple to implement and have good resolution. We combine the OFDM-based signal model with MUSIC to perform 2D and 3D radar sensing. The DOA estimation with MUSIC along with the simulation results are presented.

The second half of this thesis focuses on the realization of the hardware design for MIMO radar systems. A RF frontend for four transmitters with direct conversion architecture was considered. One transmitter includes 2 low pass filters (LPFs), an Inphase/Quadrature (I/Q) upconverter, a phase-locked loop (PLL) frequency synthesizer, a 4:1 Wilkinson power divider. Inverse Chebyshev LPFs at 50 MHz with lumped elements were built and measured. In addition, a sufficient 4:1 Wilkinson divider was simulated and fabricated to feed the local oscillator (LO) signal into the I/Q upconverters. The other individual elements of the transmitter was measured and analyzed. Several measurement have been taken to test one whole transmitter. In addition, the signals generated by the FPGA, which is planned to integrate with the transmitters, are analyzed.

Acknowledgement

Foremost, I would like to thank my supervisor, Yoke Leen Sit, for her excellent guidance, dedication and encouragement during the course of this thesis at IHE. I have learnt from her the skills for presenting ideas and writing papers. My writing skills could not have been improved significantly without her suggestions. I also would like to thank her so much for her advices which are the triggers for many important decisions within the last 2 years of my journey in Europe.

I would like to express my very sincere gratitude to Prof. Thomas Zwick from KIT to give me the opportunity to do Master thesis at IHE. I am also deeply thankful to Prof. Antonio Broquetas at UPC to encourage me to follow the topic i want and make this thesis possible. I am grateful to Prof. Trung Nguyen for enlightening me the first glance of research.

My sincere thanks also goes to Lukasz Zwirello, Xuyang Li, Serdal Ayhan, Steffen Scherr and Hadrien Theveneau at IHE for supporting me with useful guidance in the hardware and measurement part. A big thank you to Ronald Vester for fabricating all the designs.

I thank my labmates Chu Pi, Liu Hao and Ran Hao for the pleasant time we were working together. Also I thank my friends in Germany, Spain, and Vietnam to their support and encouragement.

Last but not least, I would like to thank my parents and my brother for their tremendous love, sacrifice and support spiritually for my entire life. I would like to give a special thanks to Reinhard Gentz for his accompany and love.

Contents

1. Introduction and Motivation	1
1.1. Introduction	1
1.2. Motivation	2
1.3. Outline of the Thesis	2
2. Fundamentals of the OFDM RadCom	5
2.1. Radar Basics	5
2.2. OFDM Theory	7
2.2.1. OFDM Concept	7
2.2.2. OFDM Signal Generation	10
2.2.3. OFDM in Multipath Channels and the Use of Cyclic Prefix	11
2.3. OFDM Radcom Concept	12
2.3.1. OFDM Radar Processing at the Receiver	12
2.3.2. System Parametrization	15
3. MIMO Radar Concepts	17
3.1. Virtual Array Concept	17
3.2. Signal Modeling	20
3.3. Antenna Geometry for MIMO Radar	22
3.3.1. Antenna Geometry for 2D Radar Imaging	27
3.3.2. Antenna Geometry for 3D Radar Imaging	28
3.4. MIMO Signal Waveform and Radar Processing	31
4. DOA Estimation	35
4.1. MUSIC algorithm	35
4.2. Implementation of the Signal Model in Matlab	38
4.2.1. Transmitters	38
4.2.2. Channel	38
4.2.3. Receivers	39
4.2.4. Radar processing	40
4.3. Simulation results	42
4.3.1. 2D Radar Imaging	42
4.3.2. 3D Radar Imaging	44
4.3.3. Conclusion of MUSIC Algorithm's Performace	49

5. Realization of the RF Frontend	51
5.1. Design Considerations	51
5.2. Digital to Analog Converter (DAC)	53
5.3. Low Pass Filter	54
5.4. PLL Synthesizer	57
5.5. Wilkinson Power Divider design	61
5.5.1. Transmission Line Circuit	61
5.5.2. 4:1 Wilkinson Power Divider Simulation Results	63
5.6. I/Q Modulator	66
5.7. Maximum Transmitted Power	67
6. Measurement Setup and Results	69
6.1. Measurement setup for one whole transmitter	69
6.2. Analysis of the Signals from the FPGA	71
6.2.1. Measurement for the Signals from the FPGA	72
6.2.2. Measurement of The Signal Generated by FPGA for Multiple Transmitters	76
7. Conclusion	79
8. Future works	83
8.1. Characteristics of MUSIC algorithms	83
8.2. Improvement for FPGA prototype	83
8.3. Measurement for MIMO radar	84
A. Mathematical Notations	85
A.1. Dot Product	85
A.2. Kronecker Product	85
A.3. Hermitian Transpose	85
A.4. Positive Semidefinite Hermitian Matrix	85
B. Low Pass Filter	87
B.1. Lay out for LPF	87

List of Figures

1.1. Intelligent Transport Systems [8]	1
2.1. A typical radar scene	5
2.2. Geometry of the radar and moving object for the derivation of Doppler frequency .	6
2.3. Time - frequency grid of OFDM signal	8
2.4. OFDM Modulator	9
2.5. Spectra of individual subcarriers	10
2.6. OFDM transmitter with IFFT operation	11
2.7. OFDM receiver with FFT operation	11
2.8. Cyclic Prefix	11
2.9. The operation to estimate Doppler and range for RadCom system	14
3.1. Representation of the unit pointing vector \mathbf{u} in the 3D Cartesian space	18
3.2. MIMO radar system	19
3.3. Examples of antenna geometry to form virtual array	23
3.4. Arbitrary antenna geometry	25
3.5. Antenna geometry for 2D Radar imaging	27
3.6. Beam pattern for $N_T = N_R = 4$ with $d_T = 2\lambda$ and $d_R = \lambda$	29
3.7. Antenna geometry for 3D Radar imaging	30
3.8. Equivalent virtual array	30
3.9. Regular subcarrier assignment to generate orthogonal signals	32
4.1. Geometrical interpretation of the orthogonality of the signal and noise subspaces. .	37
4.2. OFDM basic transmitter scheme	39
4.3. OFDM basic receiver scheme	40
4.4. Representation of covariance matrix of the received signals	41
4.5. Volumetric representation	43
4.6. Radar image for objects at distance $d = 20$ m	44
4.7. Radar image for objects at distance $d = 50$ m	44
4.8. Volumetric representation	45
4.9. Radar image for objects at distance $d = 20$ m	46
4.10. Radar image for objects at distance $d = 35$ m	46
4.11. Radar image for objects at distance $d = 50$ m	47
4.12. Comparison of number of antenna elements	47
4.13. Comparison of number of antenna elements	48
4.14. MUSIC performance in different SNR scenarios	49

5.1. Block diagram of the OFDM-based MIMO Radar	51
5.2. Measurement setup	52
5.3. Block diagram of the direct-conversion transmitter	52
5.4. Basic diagram of a 6-bit DAC in time and frequency domain	53
5.5. Frequency response of an inverse Chebychev filter	55
5.6. Schematic of Low pass filter	56
5.7. Transfer function of the low-pass filter	56
5.8. Reflection coefficient of low-pass filter	57
5.9. The fabricated low-pass filter	57
5.10. Block diagram of classical PLL	58
5.11. Setup of Hittite PLL with integrated VCO	59
5.12. A full span of the frequency spectrum	60
5.13. A close up look to the local oscillator signal	61
5.14. Ideal two-port Wilkinson power divider	62
5.15. Geometry of the microstrip transmission line	62
5.16. ADS transmission line model of 4:1 Wilkinson divider	64
5.17. Fabricated circuit of the 4:1 Wilkinson Power Divider	64
5.18. Simulated and measured results for return loss S_{11}	65
5.19. Simulated and measured results for insertion loss S_{21}	66
5.20. Basic I/Q Modulator Block Diagram	66
5.21. Circuit	67
6.1. Measurement setup for on transmitter	69
6.2. A full span of the output signal from the I/Q upconverter	70
6.3. The signal of interest at 24 GHz, a close up of Fig. 6.2	70
6.4. Unwanted intermodulation product at 18 GHz, a close up of Fig. 6.2	71
6.5. Unwanted intermodulation product at 12 GHz, a close up of Fig. 6.2	71
6.6. The scaling index of IFFT	72
6.7. Measurement setup to measure the signals generated by the FPGA	73
6.8. The I and Q signals from the FPGA in time domain	73
6.9. The OFDM spectrum measured from the spectrum analyzer	74
6.10. The scatter plot of the transmitted QPSK symbols in baseband	75
6.11. The 3D radar image using the signal generated from the FPGA	76
6.12. The I and Q signal from transmitter 1 (out of 4 transmitters)	77
6.13. Spectrum of I and Q analog signals for transmitter 1	77
6.14. The scatter plot of one OFDM symbol from transmitter 1	78
8.1. Nyquist sampling vs. Oversampling	84
B.1. Layout for LPF	87

List of Tables

2.1. RadCom system parameters	16
3.1. MIMO OFDM-based system parameters	34
4.1. List of objects in the simulation scenario of 2D radar imaging	42
4.2. List of objects in the simulation scenario of 3D radar imaging	45
5.1. The signals from the local oscillator	60
5.2. Roger4003C substrate specification	64
5.3. Specification of HMC815LC5 I/Q Upconverter	67
6.1. Available scaling factor for 1024 IFFT and the corresponding loss in amplitude . .	72
6.2. MIMO OFDM-based system parameters	73

List of Notations

a_t	Amplitude response of the object
d_T	Spacing of the transmit antennas
d_r	Spacing of the receive antennas
\mathbf{E}	Interference-and-noise matrix
f_c	Center frequency
f_n	Individual subcarrier frequency
f_D	Doppler frequency
\mathbf{I}	Identity matrix
N_c	Number of subcarriers used
N_{sym}	Number of symbols used
N_{ch}	Number of subchannels
N_T	Number of transmit antennas
N_R	Number of receive antennas
T	Elementary OFDM symbol duration
T_{CP}	Length of cyclic prefix
Δf	Subcarrier spacing
\otimes	Kronecker product
\mathbf{r}_k	Position vector of k^{th} object in Cartesian space
\mathbf{R}_{xx}	Covariance matrix of transmitted signals
\mathbf{R}_{yy}	Covariance matrix of the received signals
$\mathbf{v}_{rel,k}$	Relative velocity vector of the k^{th} object in Cartesian space
v_{rel}	Relative velocity
\mathbf{v}_T	Transmit steering vector
\mathbf{v}_R	Receive steering vector
\mathbf{v}	Virtual array steering vector
\mathbf{u}	Unit pointing vector in Cartesian space
$\mathbf{x}_{T,m}$	Position of m_{th} transmit antennas in Cartesian space
$\mathbf{y}_{R,n}$	Position of n_{th} receive antennas in Cartesian space
$\mathbf{x}_m(t)$	Transmitted signal
$\mathbf{y}_n(t)$	Received signal
\mathbf{X}	Matrix of transmitted signals
\mathbf{Y}	Matrix of received signals
σ	Radar cross section
ϕ	Azimuth angle
θ	Elevation angle

List of Abbreviations

OFDM	Orthogonal Frequency Division Multiplexing
QPSK	Quadrature Phase Shift Keying
QAM	Quadrature Amplitude Modulation
ITS	Intelligent Transport Systems
MIMO	Multiple Input and Multiple Output
SISO	Single Input Single Output
RCS	Radar Cross Section
FFT	Fast Fourier Transform
IFFT	Inverse Fast Fourier Transform
DFT	Discrete Fourier Transform
IDFT	Inverse Discrete Fourier Transform
DAC	Digital-to-Analog converter
LPF	Low Pass Filter
CP	Cyclic Prefix
MUSIC	MUltiple SIgnal Classification
SNR	Signal to Noise Ratio
ML	Maximum Likelihood
FPGA	Field Programmable Gate Array
RF	Radio Frequency
PLL	Phase-Locked Loop

1. Introduction and Motivation

1.1. Introduction

Nowadays, radar applications play a key role in many fields where the need for position information, such as the bearing, range and velocity of objects, is crucial. One of these applications is automotive radar in an *Intelligent Transport System (ITS)*. ITS is an advanced system defined by European Telecommunications Standards Institute (ETSI), including telematics and all type of communications in vehicles, between vehicles, and between vehicles and fixed locations. The purpose of it is to establish an intelligent network to provide network management, such as emergency vehicle notification, automatic road enforcement and so on. The scenarios of some basic communications in ITS is demonstrated in Fig. 1.1. In order to do that, the locations of individual vehicles in the network must be determined and transmitted to control stations. Therefore, the idea of a combining radar and communications in one signal system platform has been introduced.

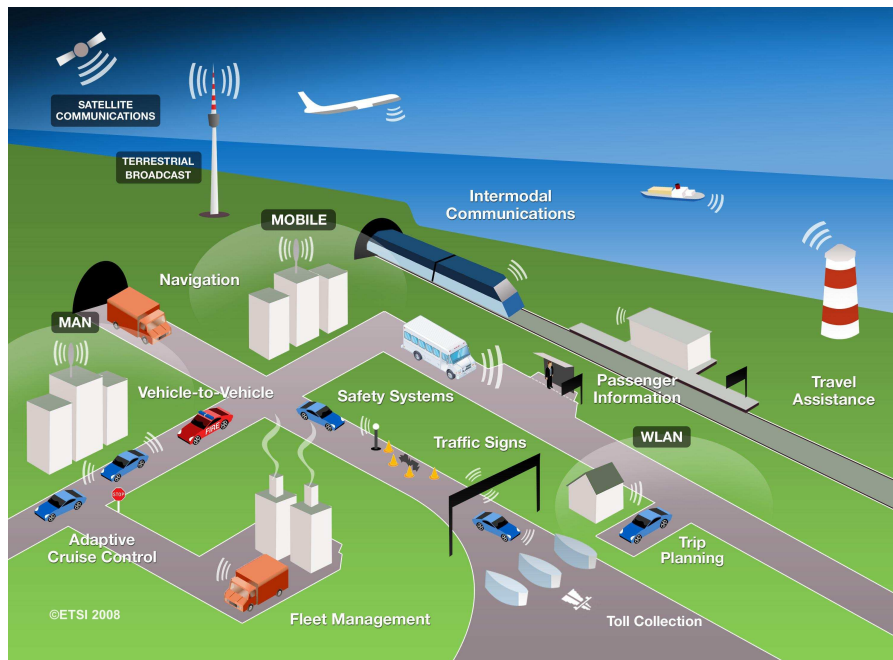


Fig. 1.1.: Intelligent Transport Systems [8]

In the previous project from Institut für Hochfrequenztechnik und Elektronik (IHE), a joint radar and communications applications (RadCom) has been proposed [20]. The orthogonal frequency-division multiplexing (OFDM) signal has been chosen because it offer several advantages, espe-

cially the robustness against Doppler shift and multipath fading. A single radar system at 24 GHz has been built and measured to prove the ability of the system to carry user data and to sense the information of range and velocity [24].

1.2. Motivation

Since the RadCom has been proved to be very promising for range and velocity estimation, the current idea is to improve a step further for direction-of-arrival (DOA) estimation. The single system is extended to multiple-input multiple output (MIMO) antenna systems. A MIMO system, unlike standard phased-array radar, can transmit, via its antennas, multiple signals which can be correlated or uncorrelated with each other [9]. It has received increasing attention from researchers because of the potential to improve target detection performance.

In order to generate uncorrelated signals for each transmit antenna, a signal modification from the original OFDM signal has been introduced in [21]. The modified signals, called the *spectrally interleaved multi-carrier signals*, have been patented [25]. The functionality of the MIMO OFDM-based radar for the DOA estimation has only been proven for the 2D radar imaging without velocity estimation. Therefore it is in the scope of this work to implement the velocity estimation together with the 2D and 3D radar imaging to come up with a robust radar system which could also do target localization. Since target localization requires multiple transmit and receive antennas as well as the use of a superresolution algorithm, a strategy to minimize the computing effort through the optimization of the simulation codes within reasonable time is also within the scope of this work.

Additionally, we seek to build the RF frontend for the multiple transmitters to verify the signal separation techniques in hardware. This analysis of a good and robust RF frontend design along with the necessary sub-blocks must be done. Although the full integration for the RF frontend might not be possible within this limited time frame, its analysis will nevertheless be a step towards the integration of the system.

1.3. Outline of the Thesis

The main contribution of this thesis is to study the concept of MIMO radar and apply MUSIC (Multiple Signal Classification), a high-resolution DOA estimation algorithm, for sensing the azimuth and elevation information of objects. A RF front end will be designed and build to integrate with the FPGA, which generates OFDM-based signals at baseband. Measurement will then be done to test the RF front end along with the algorithms.

The thesis is organized as follows. The second chapter introduces the fundamentals of radar

system and OFDM signal. The joint radar and communications application (RadCom) is also presented. In the third chapter, MIMO radar is discussed, including the concept and theory of MIMO radar, signal modeling, antenna geometry for the 2D and 3D radar imaging. Finally, the signal modification for MIMO OFDM-based radar will be explored. The fourth chapter is about DOA algorithms for the 2D and 3D radars. The MUSIC algorithm is explored. The simulation for the MIMO OFDM-based radar system is demonstrated along with the results of 2D and 3D radar imaging

In the fourth chapter, a realization of hardware design for the RF front end is discussed. Chapter 5 presents various measurements for the final transmitter and the analysis of the baseband OFDM-based signal generated by the FPGA. Finally, chapter 6 and chapter 7 give the conclusions to the work which have been done and point out the possible future works.

2. Fundamentals of the OFDM RadCom

In this chapter, the basic concepts of radars and OFDM signal are presented. Then, the overview of SISO OFDM radar and communications system (RadCom) developed by [26] is discussed. Finally, the system parameterization of the single radar system is explored.

2.1. Radar Basics

Radar is an electromagnetic system to detect and locate reflecting objects as shown in Fig. 2.1. After emitting the electromagnetic waveform, the radar receives the reflected signal from object. To detect the object, it is necessary to distinguish between the signal reflected from the object and the signal containing noise. Next, the signal can be processed to estimate the range and other parameters by comparing the received signals with the transmitted ones.

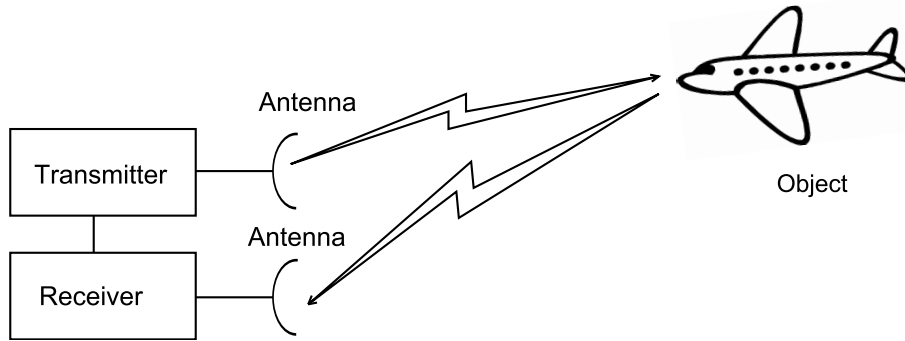


Fig. 2.1.: A typical radar scene

Range and delay

The relationship between the delay τ and range R is given by:

$$R = \frac{1}{2}c\tau \quad (2.1)$$

where c is the propagation velocity. The factor 2 is due to the round trip travel time.

Velocity and Doppler effect

Fig. 2.2 shows the geometry of radar and moving object where v is the relative velocity of the moving object. The Doppler shift is related to relative velocity as follows:

$$f_D = \frac{2f_c v_r}{c} = \frac{2f_c v \cos \phi}{c} \quad (2.2)$$

where f_c is the center frequency of the transmitted signal. The term $\cos \phi$ considers the projection of the velocity vector along the radial direction of the receiver and moving object.

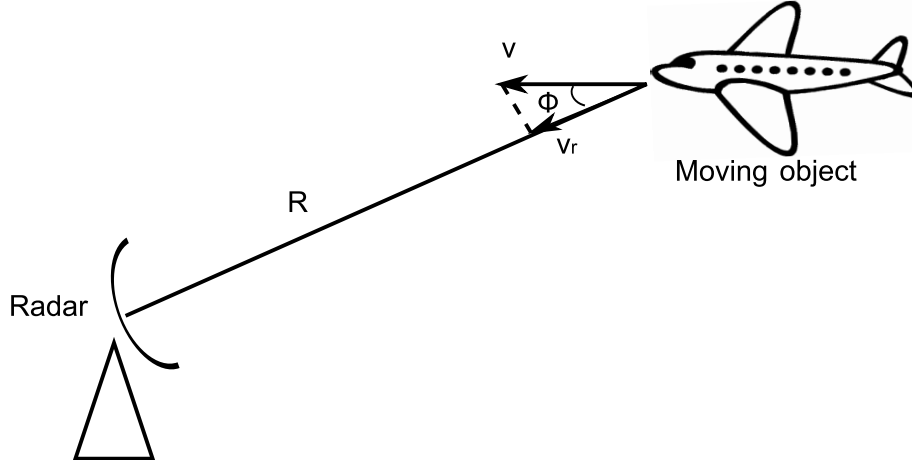


Fig. 2.2.: Geometry of the radar and moving object for the derivation of Doppler frequency

Radar equation

If a radar transmitter sends a signal with transmitted power P_t and G_t is the gain of the antenna, the power density S_t at a object of distance R from the antenna is given as:

$$S_t = \frac{P_t G_t}{4\pi R^2} \quad (2.3)$$

The power which is reflected back to the radar is given as:

$$P_s = \sigma S_t \quad (2.4)$$

where σ is the radar cross section (RCS) of the object. The received power density at the radar after reflecting on the object, S_r , is:

$$S_r = \frac{P_s}{4\pi R^2} = \frac{P_t G_t \sigma}{(4\pi R^2)^2} \quad (2.5)$$

And the received power at the radar is:

$$P_r = S_r A_{eff} \quad (2.6)$$

where:

- $A_{eff} = \frac{\lambda^2}{4\pi} G_r$ is the antenna effective area
- λ is the wavelength of transmitted signal
- G_r is the gain of the received antenna.

Thus, the received power at the radar can be obtained as:

$$P_r = \frac{P_t G_t G_r \sigma \lambda^2}{(4\pi)^3 R^4} \quad (2.7)$$

The maximum range of the radar R_{max} is the maximum distance the radar can detect objects. It happens when the received power P_r just equals the minimum detectable signal P_{rmin} . Rearranging terms in Eq. 2.7 gives:

$$R_{max} = \sqrt[4]{\frac{P_t G^2 \sigma \lambda^2}{P_{rmin} (4\pi)^3}} \quad (2.8)$$

This is the fundamental form of radar equation.

Radar cross section

This is the property of a scattering target to represent the magnitude of the reflected signal to the radar by the object.

A definition of radar cross section (RCS) in [22] is:

$$\sigma = 4\pi R^2 \frac{|E_r|^2}{|E_i|^2} \quad (2.9)$$

where

- R is the distance to the object
- E_r is the electric field strength of the reflected signal at the radar
- E_i is the electric field strength incident on the object

SNR in radar

The typical equation of SNR in radar is given as [22]:

$$SNR = \frac{P_t G_t G_r \sigma \lambda^2}{(4\pi)^3 R^4 k (T_s + T_e) B L} \quad (2.10)$$

where:

- k is Boltzmann constant
- T_s is the noise temperature at the receiver input (antenna and attenuation from cables)
- T_e is the receiver noise noise temperature including all receiver stages
- B is the receiver bandwidth
- L is loss from other factors

2.2. OFDM Theory

2.2.1. OFDM Concept

OFDM is a method of using parallel orthogonal carries to modulate the data. OFDM can be seen as a multiplexing technique rather than a modulation technique. It is mostly used as a communication

signal. The time domain OFDM transmitted signal is expressed by [20]:

$$x(t) = \sum_{\mu=0}^{N_{sym}-1} \sum_{n=0}^{N_c-1} d_{Tx}(\mu N + n) \exp(j2\pi f_n t) \text{rect}\left(\frac{t - \mu T}{T}\right) \quad (2.11)$$

where:

- N_{sym} is the number of subcarriers used
- N_c is the number of consecutive symbols evaluated
- μ is the index of OFDM symbols
- n is the carrier index in one OFDM symbol
- f_n is the individual subcarrier frequency
- T is the OFDM symbol duration
- $d_{Tx}(\mu, n)$, called the 'complex modulation symbol', is the arbitrary data modulated with a digital modulation technique e.g., quadrature amplitude modulation (QAM), phase-shift keying (PSK).

The OFDM signal in time-frequency grid is depicted in Fig. 2.3 for a clear understanding of the definitions of subcarriers and symbols. In the RadCom system, one OFDM frame consists of 1024 subcarriers and 256 OFDM symbols.

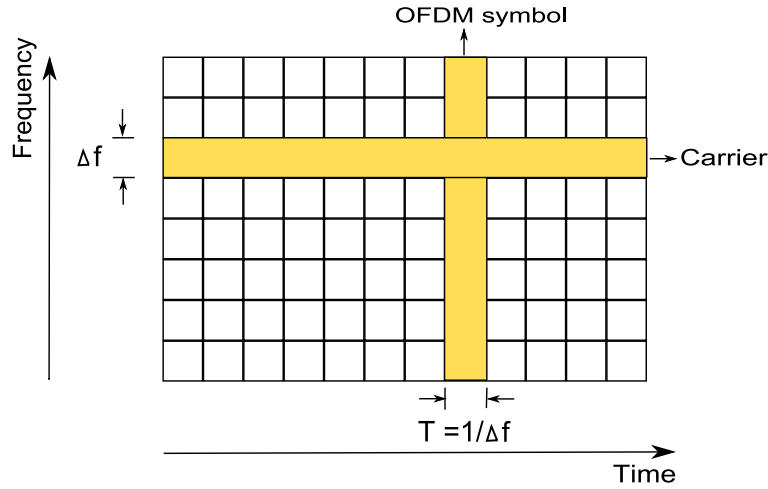


Fig. 2.3.: Time - frequency grid of OFDM signal

Fig. 2.4 shows the operation of the OFDM modulator in a block diagram. The modulated data is then demultiplexed into N_c parallel streams and multiplied with exponential functions before being summed.

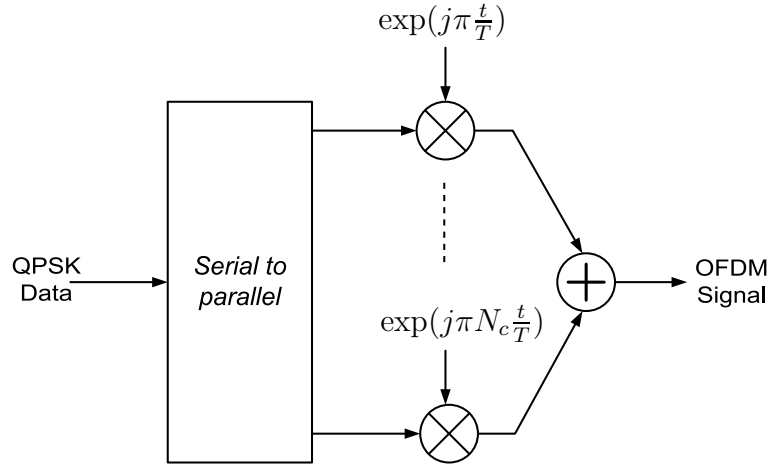


Fig. 2.4.: OFDM Modulator

The condition of orthogonality is:

$$\int_{-\infty}^{\infty} x_n(t)x_m^*(t)dt = \int_0^{T_0} x_n(t)x_m^*(t)dt = \begin{cases} 1 & m = n \\ 0 & m \neq n \end{cases} \quad (2.12)$$

where:

$$x_n(t) = \sum_{\mu=0}^{N_{sym}-1} d_{Tx}(\mu N + n) \exp(j2\pi f_n t) \text{rect}\left(\frac{t - \mu T}{T}\right)$$

Thus, in order to remain the orthogonality between individual subcarriers, the subcarrier spacing Δf must satisfy that,

$$f_n = n\Delta f = \frac{n}{T}, \quad n = 0, \dots, N - 1 \quad (2.13)$$

The frequency spectrum of the transmitted signal in equation (2.11) is:

$$X(f) = \sqrt{T} \sum_{n=0}^{N_c-1} d_{Tx}(n) \frac{\sin(\pi(f - f_n)T)}{\pi(f - f_n)T} \quad (2.14)$$

Fig. 2.5 represents the frequency spectrum of OFDM signals. In the frequency domain, the *sinc* function side lobes produce overlapping spectra. However, since the individual peaks of subcarriers all line up with the zero crossing of other subcarriers, the overlap of spectral energy does not interfere with the ability to recover the original signal.

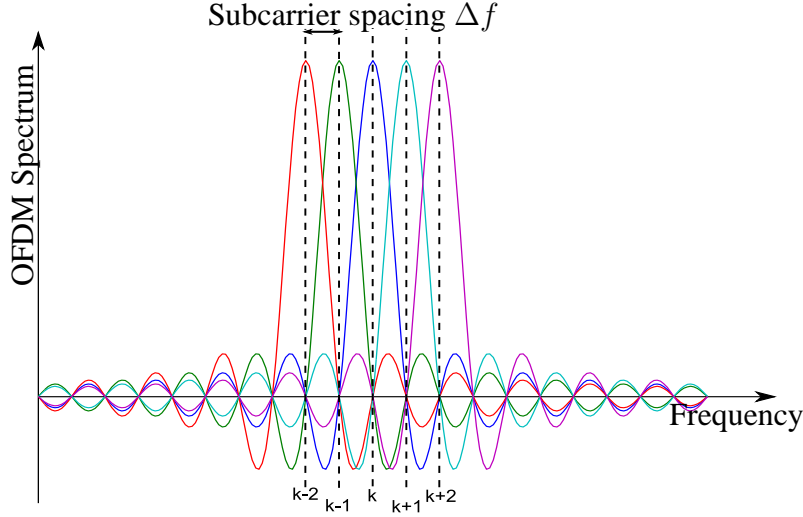


Fig. 2.5.: Spectra of individual subcarriers

2.2.2. OFDM Signal Generation

Consider one OFDM symbol, the baseband transmitted signal is given by:

$$x(t) = \sum_{n=0}^{N_c-1} d_{Tx}(n) \exp(j2\pi \frac{n}{T} t) \text{rect} \left(\frac{t}{T} - \frac{1}{2} \right) \quad (2.15)$$

In fact, considering the case of time discrete signal by replacing the time t by a sample number k , the complex baseband OFDM is nothing more than the inverse discrete Fourier Transform (IDFT) on N_c input modulation symbols. It means that, for each time interval of length T , OFDM signals is created by using a IDFT and its counterpart, DFT for demodulation at receiver.

In practice, a combination of fast Fourier Transform (FFT) and inverse fast Fourier Transform (IFFT) are implemented because of their efficiency to reduce the calculation time. Fig. 2.6 and Fig. 2.7 depict a typical OFDM system with transmitter and receiver. At the transmitter, the sources symbols are divided into blocks of length N_c and used as the inputs of an IFFT blocks with FFT length N_{FFT} . N_{FFT} should be chosen to be significantly large than N_c so that the edge effects are negligible at half the sampling frequency and the shape of the reconstruction filter of the digital-to-analog converter (DAC) does not effect the significant part of the spectrum [11]. The $N_{FFT} - N_c$ remaning coefficients can be set to zero.

At the receiver, an FFT block with length N_{FFT} is used to process the received signal, and the N_c useful coefficients will be extracted for further data processing.

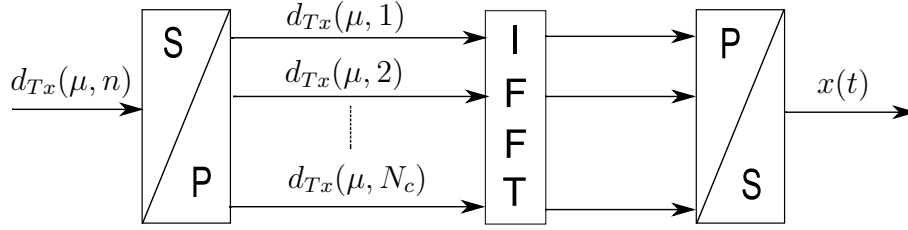


Fig. 2.6.: OFDM transmitter with IFFT operation

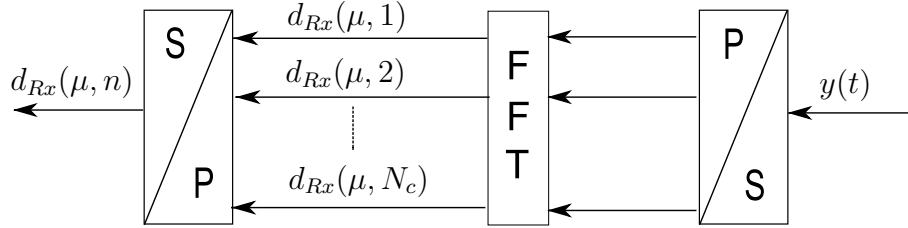


Fig. 2.7.: OFDM receiver with FFT operation

2.2.3. OFDM in Multipath Channels and the Use of Cyclic Prefix

In OFDM system, intersymbol interference (ISI) occurs when the received OFDM symbol is distorted by the previously transmitted OFDM symbol. To prevent from ISI, a guard interval can be implemented by using a cyclic prefix (CP). The CP is simply the replica of a piece of length T_{CP} from the end of the symbol. The reason is to keep one of the signals periodic over the range of the convolution in time domain. A lack of periodicity would lead to intrasymbol interference, which causes the OFDM symbol to interfere with itself. Since the CP contains redundant information, it is discarded at the receiver. Fig. 2.8 shows the method of introducing the cyclic prefix by coping a piece of length T_{CP} from the the end of the symbol and put it in front of the signal.

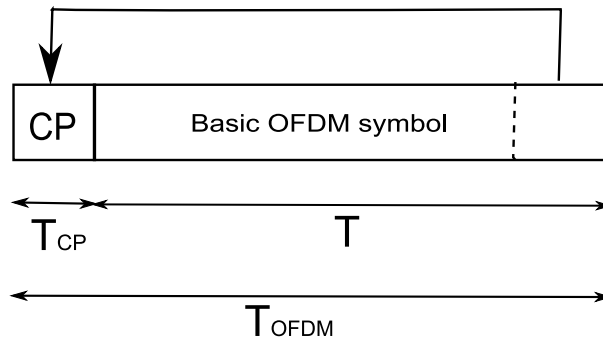


Fig. 2.8.: Cyclic Prefix

2.3. OFDM Radcom Concept

OFDM has been recently gained attention for radar application because of the numerous advantages offered by OFDM signal. Furthermore, OFDM signals have been proved to be suitable for radar applications [20], [23], [24], [21]. In this section, the SISO OFDM-based radar system (RadCom) will be explored.

2.3.1. OFDM Radar Processing at the Receiver

As mentioned in section 2.2.1, the OFDM transmitted signal is represented as in (2.11).

Transmitted OFDM symbols can be represented as a matrix with N_c rows and N_{sym} columns.

$$\mathbf{D}_{Tx} = \begin{pmatrix} d_{Tx}(0, 0) & d_{Tx}(0, 1) & \cdots & d_{Tx}(0, N_{sym} - 1) \\ d_{Tx}(1, 0) & d_{Tx}(1, 1) & \cdots & d_{Tx}(1, N_{sym} - 1) \\ \vdots & \vdots & \ddots & \vdots \\ d_{Tx}(N_c - 1, 0) & d_{Tx}(N_c - 1, 1) & \cdots & d_{Tx}(N_c - 1, N_{sym} - 1) \end{pmatrix} \quad (2.16)$$

Every row of the matrix is related to the information on one subcarrier and every column is related to the information on one OFDM symbol.

In the presence of a reflecting object at the distance R from the radar with the relative velocity of v_{rel} , which results in the Doppler frequency of f_D , the received OFDM signal in noiseless case becomes

$$y(t) = \sum_{\mu=0}^{N_{sym}-1} \sum_{n=0}^{N_c-1} a(\mu, n) d_{Tx}(\mu N_c + n) \exp \left(j2\pi(f_n + f_D) \left(t - \frac{2R}{c_0} \right) \right) \cdot \text{rect} \left(\frac{t - \frac{2R}{c_0} - \mu T}{T} \right) \quad (2.17)$$

In the above model, the transmitted signal $x(t)$ is a narrowband signal of overall bandwidth $B \ll f_c$ so that each subcarrier experiences the same Doppler shift f_D . In addition, $f_D \ll f_c$, thus the term regarding to the coupling between Doppler effect and range $\exp(-j2\pi f_D 2R/c_0)$ is insignificant and can be neglected. The received OFDM signal can be rewritten as follows:

$$y(t) = \sum_{\mu=0}^{N_{sym}-1} \sum_{n=0}^{N_c-1} a(\mu, n) d_{Tx}(\mu N_c + n) \exp \left(j2\pi f_n \left(t - \frac{2R}{c_0} \right) \right) \exp(j2\pi f_D t) \text{rect} \left(\frac{t - \frac{2R}{c_0} - \mu T}{T} \right) \quad (2.18)$$

Define d_{Rx} as the complex received symbol, we have:

$$y(t) = \sum_{\mu=0}^{N_{sym}-1} \sum_{n=0}^{N_c-1} d_{Rx}(\mu N_c + n) \exp(j2\pi f_n t) \text{rect} \left(\frac{t - \frac{2R}{c_0} - \mu T}{T} \right) \quad (2.19)$$

and

$$d_{Rx}(\mu, n) = a(\mu, n)d_{Tx}(\mu, n) \exp \left(-j2\pi f_n \left(\frac{2R}{c_0} \right) \right) \exp(j2\pi f_D t) \quad (2.20)$$

It means that the received symbol d_{Rx} contains the information of the transmitted one d_{Tx} , the attenuation a along with the phase rotation caused by range and Doppler effect. The received OFDM symbols can also be represented as matrix \mathbf{D}_{Rx} which has the same size as \mathbf{D}_{Tx} . Thus, a complex element-wise division can be operation can be performed between \mathbf{D}_{Rx} and \mathbf{D}_{Tx} to remove the original transmit modulation symbols:

$$\mathbf{D}_{div} = \frac{\mathbf{D}_{Rx}}{\mathbf{D}_{Tx}} = \begin{pmatrix} d(0, 0) & d(0, 1) & \cdots & d(0, N_{sym} - 1) \\ d(1, 0) & d(1, 1) & \cdots & d(1, N_{sym} - 1) \\ \vdots & \vdots & \ddots & \vdots \\ d(N_c - 1, 0) & d(N_c - 1, 1) & \cdots & d(N_c - 1, N_{sym} - 1) \end{pmatrix} \quad (2.21)$$

For specific values of μ, n , we have one elements $d(n, \mu)$ of the matrix as follows

$$d(n, \mu) = \frac{d_{Rx}(n, \mu)}{d_{Tx}(n, \mu)} = a(\mu, n) \exp \left(-j2\pi f_n \left(\frac{2R}{c_0} \right) \right) \exp(j2\pi f_D t) \quad (2.22)$$

The Doppler shift will cause a phase shift of $\mu f_D T$ on the μ -th symbol on every carrier. In case CP is implemented, the entire OFDM symbol duration T_{OFDM} including the CP must be considered. Equation (2.21) can be rewritten as

$$d(n, \mu) = \frac{d_{Rx}(n, \mu)}{d_{Tx}(n, \mu)} = a(\mu, n) \exp \left(-j2\pi n \Delta f \left(\frac{2R}{c_0} \right) \right) \exp(j2\pi \mu T_{OFDM} f_D) \quad (2.23)$$

It is obvious that the phase difference between the transmitted and received symbols, which contains the information of distance and velocity, can be calculated from $d(n, \mu)$. Thus, a novel method has been proposed to provide the radar image from the transmitted and received modulation symbols without the need for correlation operations [20], [23], [24]. Fig. 2.9 describes the new method to estimate the distance and velocity of the object and it can be summarized as follows,

1. Calculate the FFT of length N_{sym} on every row of \mathbf{D}_{div} .
2. Calculate the IFFT of length N_c on every column.

The result is a two-dimensional matrix as follows:

$$\mathbf{I}_{k,l} = \text{IFFT}(l) [\text{FFT}(k)[\mathbf{D}_{div}]] \quad (2.24)$$

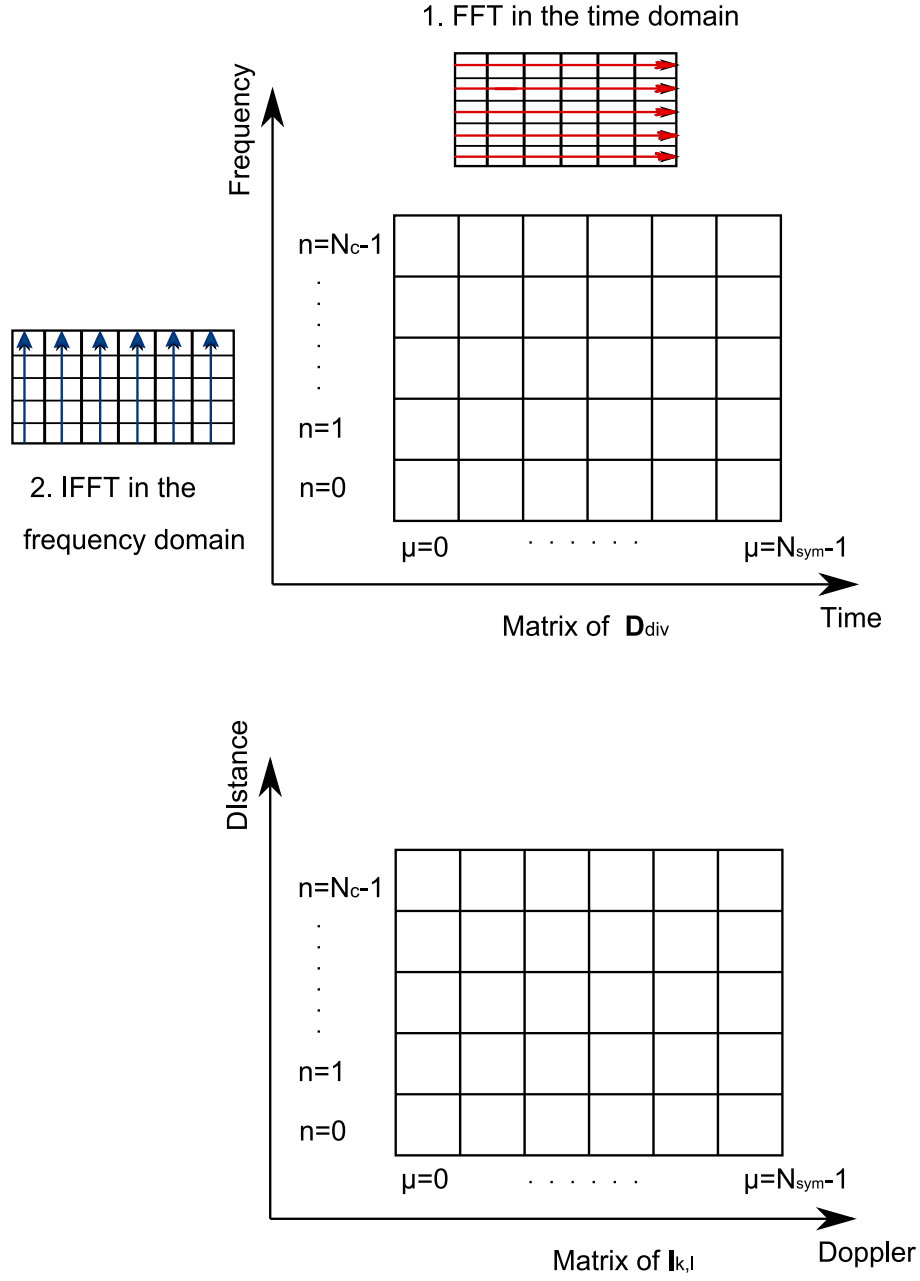


Fig. 2.9.: The operation to estimate Doppler and range for RadCom system

For every reflecting object, there is a peak in $|\mathbf{I}_{k,l}|^2$ at index (k, l) .

$$\hat{k} = \left\langle \frac{2R\Delta f N_c}{c_0} \right\rangle, k = 0, \dots, N_c - 1 \quad (2.25)$$

and

$$\hat{l} = \left\langle \frac{2v_{rel} f_c T_{OFDM} N_{sym}}{c_0} \right\rangle, l = 0, \dots, N_{sym} - 1 \quad (2.26)$$

where the operation $\langle k \rangle$ means the nearest or equal integer to k .

Therefore, the index values (\hat{k}, \hat{l}) also correspond to the estimated distance \hat{R} and relative velocity \hat{v}_{rel} as

$$\hat{R} = \frac{\hat{l}c_0}{2N_c\Delta f} \quad (2.27)$$

and

$$\hat{v}_{rel} = \frac{\hat{k}c_0}{2f_c N_{sym} T_{OFDM}} \quad (2.28)$$

2.3.2. System Parametrization

The process of deciding and defining the parameters for a system is one of the most important phase to build any system. The 24 GHz ISM (industrial, scientific, and medical) band from 24.05 GHz-24.25 GHz is chosen since the ISM band is license free and suitable for radar research.

Subcarrier Spacing and Symbol Duration

Doppler shift

The Doppler shift in radar system can be described as follows

$$f_D = \frac{2v_{rel}}{\lambda} \quad (2.29)$$

where f_D is the Doppler frequency and v_{rel} is the relative velocity between radar and object. In order to avoid the distortion of the orthogonality of the subcarriers, the subcarrier spacing Δf must satisfy the condition

$$\Delta f > 10f_{D,max} \quad (2.30)$$

where $f_{D,max}$ is the maximum Doppler shift. Assuming a maximum relative velocity for typical traffic scenarios to be $v_{rel} = 200 \text{ km/h} = 55.6 \text{ m/s}$, this would yield the maximum Doppler shift of $f_{D,max} = 8.9 \text{ kHz}$ for $f_c = 24 \text{ GHz}$. Thus it requires a minimum subcarrier spacing $\Delta f > 89 \text{ kHz}$

Range ambiguity

The maximum unambiguous distance of radar system is equal to

$$d_{max} = \frac{c_0}{2\Delta f} = \frac{T_0 c_0}{2} \quad (2.31)$$

where c_0 is the propagation velocity, T_0 is the OFDM symbol duration. For automotive uses, the maximum detectable distance is set to be 200 m. For practical reasons, the symbol duration and subcarrier spacing have to satisfy that $T_0 > 1.33 \mu\text{s}$ and $\Delta f < 750 \text{ kHz}$.

Cyclic Prefix

As mentioned in section 2.2.3, each transmitted OFDM symbol has to be added with a CP to avoid ISI. Since there is a direct coupling between transmit antenna and receive antenna of RadCom system [27], the CP has to be at least equal to the propagation time of the longest path between radar and the object. Assuming that the maximum distance R is 200 m, the condition for CP is that $T_{CP} > 1.33 \mu\text{s}$.

Symbol	Parameter	Value
f_c	Carrier frequency	24 GHz
N	Number of subcarriers	1024
Δf	Subcarrier spacing	90.909 kHz
T	Elementary OFDM symbol duration	11 μs
T_{CP}	Cyclic prefix duration	1.365 μs
T_{sym}	Transmit OFDM symbol duration	12.375 μs
B	Total signal bandwidth	93.1 MHz
Δr	Range resolution	1.61 m
r_{max}	Maximum unambiguous range	1650 m
v_{max}	Maximum unambiguous velocity	$\pm 252.5 \text{ m/s}$
M	Number of evaluated symbols	256
Δv	Velocity resolution	1.97 m/s

Table 2.1.: RadCom system parameters

Final System Parametrization

In the RadCom system, the final parameters are fixed for a suitable OFDM radar and communication system. The OFDM symbol duration is chosen to be $T_o = 11 \mu\text{s}$, which leads to $\Delta f = 1/T_o = 90.909 \text{ kHz}$. The CP length $T_{CP} = 1/8 T_o = 1.375 \mu\text{s}$

Since the OFDM signal can be generated by performing a IFFT operation, it is efficient to choose a number of subcarriers which is the power of 2. With a subcarrier spacing of $\Delta f = 1/T_o = 90.909 \text{ kHz}$, a number of subcarriers of $N_c = 1024$ will result a bandwidth of $B = 93.09 \text{ MHz}$, so that the radar range resolution will be equal to $\Delta r = 1.61 \text{ m}$. A summary of all system parameter is provided in table (2.1).

3. MIMO Radar Concepts

In this chapter, we first introduce the concept of MIMO radar and virtual steering vector. The steering vector is used in the MUSIC algorithm to estimate the position of the objects, as will be discussed in the next chapter. Next, the general signal modeling and antenna geometry are derived. Finally, the modification of the original OFDM-based signal from the SISO RadCom for use in the MIMO radar is discussed.

3.1. Virtual Array Concept

The MIMO radar system allows the transmitting of orthogonal (or incoherent) waveforms at each transmit antennas. The phase differences caused by the different transmit antennas along with ones caused by different receive antennas form a new *steering vector*. In this section, we will discuss briefly the virtual array concept. The detailed studies can be found in [5], [6], [9].

The steering vector represents the set of phase delays of plane wave experiences [3]. This is then evaluated at set of antenna array elements (especially at the receiver). By using an array-based DOA estimation techniques, the receive signals along with the steering vectors are evaluated to estimate the position of the objects. Depending on the steering vector, the azimuth or elevation position of the objects, or even both can be estimated.

A *virtual array* refers to the technique whereby the number of receiver antennas become more than the physical number of the antennas through the use of special antenna geometries and signal processing. Therefore the steering vector developed for such a virtual array is called the *virtual steering vector*. Before establishing the virtual array concept, a few assumptions and definitions need to be clarified:

1. The MIMO radar system is a monostatic one. It means that the transmitter and receiver are located on the same platform.
2. The objects described in this work are in the far-field region of the antenna arrays of the MIMO radar.
3. The distance between the radar and the objects are much larger than the dimensions of the transmit and receive antennas. Therefore, the unit pointing vectors from the object to the transmitter and receiver are coincident and can be defined as a vector $\mathbf{u} \in \mathbb{R}^3$, where \mathbb{R}^3 defines a 3-dimensional (3D) Cartesian space. The coordinates of \mathbf{u} is (x_u, y_u, z_u) as shown in Fig. 3.1.

4. The 3D Cartesian space applies for all other position vectors, which will be defined in the following sections. This means that the point of origin as well as the x , y and z axis directions are the same for all of these vectors.

Consider a MIMO radar system using antenna arrays for its transmitter and receiver with the mathematical notations as follows:

- N_T is the number of elements at the transmit antenna array
- N_R is the number of elements at the receive antenna array
- The m^{th} transmit antenna is located at $\mathbf{x}_{T,m} \in \mathbb{R}^3$, where the subscript T stands for transmitter and m is the index of the transmit antenna, with $m = 0, 1, \dots, N_T - 1$
- The n^{th} receive antenna is located at $\mathbf{x}_{R,n} \in \mathbb{R}^3$, where the subscript R stands for receiver and n is the index of the receive antenna, with $n = 0, 1, \dots, N_R - 1$

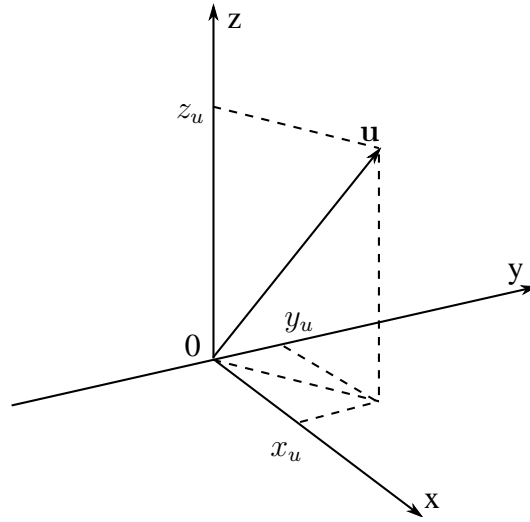


Fig. 3.1.: Representation of the unit pointing vector \mathbf{u} in the 3D Cartesian space

Now the separate arrays of transmit and receive antennas pointing at one object in the far field are considered. Fig. 3.2(a) shows an example of a MIMO radar system with $N_T = 3$ and $N_R = 4$ at arbitrary positions with the same pointing vector \mathbf{u} to the same object in the far-field region. The transmit array and the receive array are collocated but are pictured side by side for illustration. At one point, the m^{th} transmit antenna transmits the waveform $x_m(t)$. Since the transmitted signals from each transmitter are orthogonal, the signals fulfill the condition of orthogonality as given by

$$\int x_m(\tau) x_{m'}^*(\tau) d\tau = \delta_{mm'} \quad (3.1)$$

where the integration of the signal x_m with the conjugate of the signal from another transmitter (in the same array) $x_{m'}^*$ over time will result in $\delta_{mm'} = 1$ if and only if $m = m'$.

At each receive antenna, the reflected orthogonal waveforms from the object can be extracted by correlating the transmitted signals with the received ones. This correlation process is actually a

matched filter process. The total number of received signals at all receivers is then equal to $N_T N_R$. Ignoring all effects of the channel (e.g. phase rotations due to range and Doppler) and considering only the effect due to the geometry of the transmit and receive positions, the received signal from the m^{th} transmit antenna the n^{th} receive antenna can be expressed as [4],

$$y_{m,n}(t) = a_t \exp(-jk\mathbf{u} \cdot (\mathbf{x}_{T,m} + \mathbf{x}_{R,n})) \quad (3.2)$$

where:

- (\cdot) is the notation of dot product. The details of dot product can be found in the appendix.
- $k = 2\pi/\lambda$ is the wavenumber therefore $k\mathbf{u}$ is the wave vector.
- a_t is the amplitude of the signal reflected from the object.

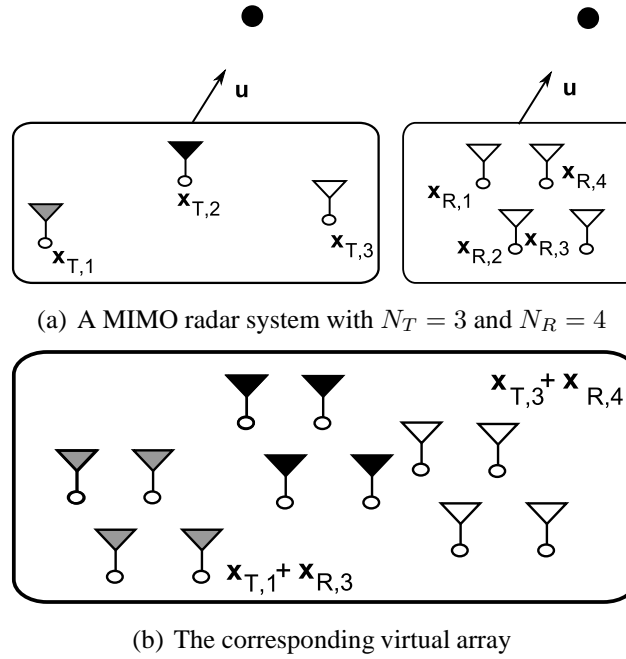


Fig. 3.2.: MIMO radar system

From (3.2), it can be seen that the phase differences are created by both the transmit and receive antenna positions. Fig. 3.2(b) illustrates the corresponding virtual antenna formed from the transmit and receive arrays as seen at the receiver. The received signal in (3.2) is then equivalent to the object response received by a receive array with $N_T N_R$ virtual antenna elements located at the positions of the transmitters plus the positions of the receivers, which can be expressed as:

$$\{\mathbf{x}_{T,m} + \mathbf{x}_{R,n} \mid n = 0, 1, \dots, N - 1; m = 0, 1, \dots, M - 1\} \quad (3.3)$$

This can be seen as replicating the receive antenna array at every individual transmitter, which in mathematical notation is the Kronecker product.

With the information about the virtual array positioning, the steering vectors for the transmit and receive array can be built. Defining $\mathbf{v}_T(\mathbf{u})$ as the transmit steering vector with dimension $N_T \times 1$ and $\mathbf{v}_R(\mathbf{u})$ as the receive steering vector with dimension $N_R \times 1$, $\mathbf{v}_T(\mathbf{u})$ and $\mathbf{v}_R(\mathbf{u})$ are given respectively as follows.

$$(\mathbf{v}_T)_m = \exp(-jk\mathbf{u} \cdot \mathbf{x}_{T,m}) \quad (3.4)$$

$$(\mathbf{v}_R)_n = \exp(-jk\mathbf{u} \cdot \mathbf{x}_{R,n}) \quad (3.5)$$

For the case of arbitrary transmitter and receiver positions whose virtual array is as described by (3.3), the virtual steering vector $\mathbf{v}(\mathbf{u})$ can be written as

$$\mathbf{v}(\mathbf{u}) = \mathbf{v}_T(\mathbf{u}) \otimes \mathbf{v}_R(\mathbf{u}) \quad (3.6)$$

where \otimes is the notation of the Kronecker product. The dimension of $\mathbf{v}(\mathbf{u})$ is $N_T N_R \times 1$. It can be concluded that from $N_T + N_R$ physical antenna elements, a virtual array with $N_T N_R$ elements can be generated. This concept is important in order to define an appropriate antenna geometry for MIMO radar in section 3.3.

3.2. Signal Modeling

In this section, the signal modeling for the MIMO radar will be derived. The idea of the signal modeling is to represent the received signal taking into account the channel parameters (e.g. range and Doppler) and antenna positioning for a better understanding.

Consider a MIMO system with the transmit antennas and receive antennas as discussed in section 3.1. An object located at the position vector $\mathbf{r} \in \mathbb{R}^3$ is moving with a relative velocity vector \mathbf{v}_{rel} to the radar. The signals transmitted by the transmit array are reflected from the object and the received signal at the n^{th} receive antenna at time t from the m^{th} transmit antenna can be represented by the far-field approximation. The phase rotation due to the moving object and its distance to the radar can be expressed as

$$\text{phase rotation} \approx \exp\left(-j\frac{2\pi f_c}{c}\mathbf{u} \cdot 2\mathbf{r}\right) \exp\left(-j\frac{2\pi f_c}{c}\mathbf{u} \cdot 2\mathbf{v}_{rel}t\right) \exp\left(-j\frac{2\pi f_c}{c}\mathbf{u} \cdot [\mathbf{x}_{T,m} + \mathbf{x}_{R,n}]\right) \quad (3.7)$$

In (3.7), the first term is due to the range (transmitted and reflected), the second term is due to the relative velocity of the object to the radar, and the last term takes the position of the antenna array into account.

Consider the n^{th} receive antenna out of N_R receive antennas, the received signal from all the transmit antennas without considering the type of waveform used can be expanded from (3.2) and written

as

$$y_n(t) = a_t \exp \left(-j \frac{2\pi f_c}{c} \mathbf{u} \cdot 2\mathbf{r} \right) \exp \left(-j \frac{2\pi f_c}{c} \mathbf{u} \cdot 2\mathbf{v}_{rel} t \right) \cdot \sum_{m=1}^{N_T} x_m(t) \exp \left(-j \frac{2\pi f_c}{c} \mathbf{u} \cdot [\mathbf{x}_{T,m} + \mathbf{x}_{R,n}] \right) \quad (3.8)$$

Next, consider all transmitters and receivers. To come to a general expression for all of the antennas within the antenna arrays, we define \mathbf{X} and \mathbf{Y} as the matrices for the signals at the transmit and receive antennas respectively. The signals here are considered as time-discrete signals. The \mathbf{X} and \mathbf{Y} matrices are expressed as

$$\mathbf{X} = [\mathbf{x}_1 \quad \mathbf{x}_2 \quad \cdots \quad \mathbf{x}_{N_T}]^T \quad (3.9)$$

and

$$\mathbf{Y} = [\mathbf{y}_1 \quad \mathbf{y}_2 \quad \cdots \quad \mathbf{y}_{N_R}]^T \quad (3.10)$$

Substituting the matrix notations into (3.8), the equivalent received signal at the n^{th} receive antenna is

$$\mathbf{y}_n = a_t \cdot \exp \left(-j \frac{2\pi f_c}{c} \mathbf{u} \cdot 2\mathbf{r} \right) \exp \left(-j \frac{2\pi f_c}{c} \mathbf{u} \cdot 2\mathbf{v}_{rel} t \right) \exp \left(-j \frac{2\pi f_c}{c} \mathbf{u} \cdot \mathbf{x}_{R,n} \right) \mathbf{v}_T^T(\mathbf{u}) \mathbf{X} \quad (3.11)$$

where \mathbf{v}_T is the transmit steering vector defined in section 3.1 and \mathbf{v}_T^T is the transpose of \mathbf{v}_T .

Reducing all receivers into the matrix form, we have:

$$\mathbf{Y} = a_t \exp \left(-j \frac{2\pi f_c}{c} 2\mathbf{u} \cdot \mathbf{r} \right) \exp \left(-j \frac{2\pi f_c}{c} \mathbf{u} \cdot 2\mathbf{v}_{rel} t \right) \mathbf{v}_R(\mathbf{u}) \mathbf{v}_T^T(\mathbf{u}) \mathbf{X} \quad (3.12)$$

where $\mathbf{v}_R(\mathbf{u})$ and $\mathbf{v}_T(\mathbf{u})$ are the receive and transmit steering vector defined in (3.6) respectively. Vector $\mathbf{v}_R(\mathbf{u})$ has dimension $n_R \times 1$ and vector $\mathbf{v}_T(\mathbf{u})$ has dimension $n_T \times 1$. The multiplication product of $\mathbf{v}_R(\mathbf{u}) \mathbf{v}_T^T(\mathbf{u})$ is a matrix with dimension $n_R \times n_T$.

Consider the case of K objects at positions \mathbf{r}_k and velocity $\mathbf{v}_{rel,k}$, the received signal matrix \mathbf{Y} in a noisy channel can be modified to accommodate K objects and is expressed as

$$\mathbf{Y} = \sum_{k=1}^K a_{tk} \exp \left(-j \frac{2\pi f_c}{c} 2\mathbf{u}_k \cdot \mathbf{r} \right) \exp \left(-j \frac{2\pi f_c}{c} \mathbf{u}_k \cdot 2\mathbf{v}_{rel,k} t \right) \mathbf{v}_R(\mathbf{u}_k) \mathbf{v}_T^T(\mathbf{u}_k) \mathbf{X} + \mathbf{E} \quad (3.13)$$

where \mathbf{E} is the interference-plus-noise matrix.

Equation (4.13) can then be rewritten as

$$\mathbf{Y} = \mathbf{S}\mathbf{X} + \mathbf{E} \quad (3.14)$$

where \mathbf{S} is a matrix defined as

$$\mathbf{S} = \sum_{k=1}^K a_{tk} \exp\left(-j\frac{2\pi f_c}{c} 2\mathbf{u}_k \cdot \mathbf{r}\right) \exp\left(-j\frac{2\pi f_c}{c} \mathbf{u}_k \cdot 2\mathbf{v}_{rel}t\right) \mathbf{v}_R(\mathbf{u}_k) \mathbf{v}_T^T(\mathbf{u}_k) \quad (3.15)$$

Matrix \mathbf{S} consist of the steering vector, which defines the signal subspace and will be used for the MUSIC algorithm in section 4.1.

Since the transmitted signal from each receiver are orthogonal to each other, the received signals can be separated by N_T matched filters as explained in section 3.1. The N_R *real* antennas are now equivalent to $N_R N_T$ *virtual* antennas. The modified received signal matrix $\hat{\mathbf{Y}}$ is used to accommodate to the virtual array as follows:

$$\hat{\mathbf{Y}} = \sum_{k=1}^K a_{tk} \exp\left(-j\frac{2\pi f_c}{c} 2\mathbf{u}_k \cdot \mathbf{r}\right) \exp\left(-j\frac{2\pi f_c}{c} \mathbf{u}_k \cdot 2\mathbf{v}_{rel}t\right) \mathbf{v}_T \otimes \mathbf{v}_R \hat{\mathbf{X}} + \hat{\mathbf{E}} \quad (3.16)$$

where

$$\hat{\mathbf{X}} = \mathbf{I}_{N_R} \otimes \mathbf{X} \quad (3.17)$$

where \mathbf{I}_{N_R} is the identity matrix with dimension $N_R \times 1$.

3.3. Antenna Geometry for MIMO Radar

Until now, we have only introduced the virtual array and the signal modeling for an arbitrary antenna geometry. Another important aspect of MIMO radar is the antenna geometry since different geometries of receive and transmit arrays can lead to different virtual array geometries. Many studies have been conducted to optimize the antenna geometry for specific applications such as in [18]. The purpose of this section is to provide a general way to represent the virtual array and to form the steering vector for any antenna system geometry.

The MIMO virtual array positions are the convolution of the original transmit and receive array element positions as explained in [4], [6]. The antenna geometry can be visualized as a Dirac function. Defining $h_T(\mathbf{x})$ and $h_R(\mathbf{x})$ as the functions characterizing the antenna positions of the transmitter and receiver respectively, $h_T(\mathbf{x})$ and $h_R(\mathbf{x})$ can be described as

$$h_T(\mathbf{x}) = \sum_{m=0}^{N_T-1} \delta(\mathbf{x} - \mathbf{x}_{T,m}) \quad (3.18)$$

and

$$h_R(\mathbf{x}) = \sum_{n=0}^{N_R-1} \delta(\mathbf{x} - \mathbf{x}_{R,n}) \quad (3.19)$$

Thus, the function to characterize the antenna positions in the virtual array is

$$h(\mathbf{x}) = (h_T * h_R)(\mathbf{x}) \quad (3.20)$$

where $(*)$ is the convolution operation.

Given here is an example of a MIMO system with uniform linear array (ULA), where the antenna element are separated by the multiples of half wavelength $\lambda/2$. An array with the notation $\{1 \ 1 \ 1\}$ means that there are 3 antennas with the element distance of $\lambda/2$ on a linear grid. Using this array for both the transmitter and receiver as depicted in Fig. 3.3 (top), the corresponding MIMO virtual array is

$$\{1 \ 1 \ 1\} * \{1 \ 1 \ 1\} = \overbrace{\{1 \ 2 \ 3 \ 2 \ 1\}}^5 \quad (3.21)$$

This means that some virtual antennas are over represented. Therefore the MIMO virtual array contains only 5 elements despite having 6 transmitter and receiver elements.

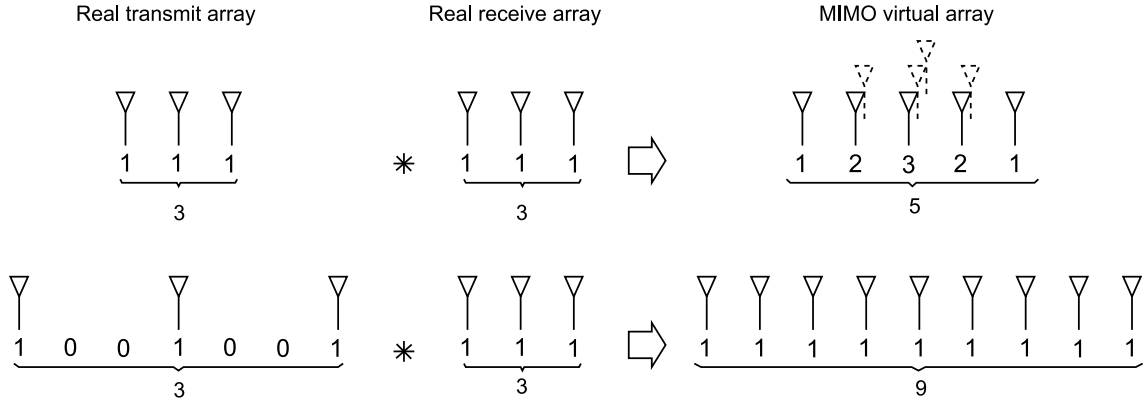


Fig. 3.3.: Examples of antenna geometry to form virtual array

Now the geometry of the transmit antennas is changed as depicted in Fig. 3.3 (bottom) with a notation of $\{1 \ 0 \ 0 \ 1 \ 0 \ 0 \ 1\}$ and the receive array is $\{1 \ 1 \ 1\}$. These notations are equivalent to a MIMO system with $N_T = 3$ and $N_R = 3$. Here, $d_T = 3d_R$ where d_T and d_R are the element spacing of the transmit and receive antennas respectively. In this case, a MIMO virtual array with full $N_T N_R = 9$ elements is formed and this is the basis of the classical virtual antenna array which has the largest nonzero contiguous region.

In DOA estimation, the number of elements in transmit and receive array plays an important role in increasing the angular resolution. Despite the classical virtual array having the largest contiguous

region, it might not be optimized for the DOA angular resolution. There are many ongoing work on such optimization, namely for the 2D configuration, which can be found in [18]. However, the optimized virtual array is not in the scope of this work, therefore the classical virtual antenna array is used for the 2D imaging case. For the 3D imaging case, a simple geometry, where all element spacing is $\lambda/2$ is used.

In next step, a general antenna geometry is taken into consideration a set of equations to estimate the virtual steering vector. This equation is a general equation with no particular antenna geometry and is thus for any MIMO radar system.

Considering a MIMO system as presented in section 3.1, the additional notations for this part are defined as follows:

- The m^{th} transmit antenna is located at $\mathbf{x}_{T,m} \in \mathbb{R}^3$ with the coordinates

$$\mathbf{x}_{T,m} = \begin{pmatrix} x_{T,m} \\ y_{T,m} \\ z_{T,m} \end{pmatrix}$$

- The n^{th} receive antenna is located at $\mathbf{x}_{R,n} \in \mathbb{R}^3$ with the coordinates:

$$\mathbf{x}_{R,n} = \begin{pmatrix} x_{R,n} \\ y_{R,n} \\ z_{R,n} \end{pmatrix}$$

- The position of the k^{th} object is the vector $\mathbf{r}_k \in \mathbb{R}^3$ with the coordinates:

$$\mathbf{r}_k = \begin{pmatrix} R_k \cos \theta_k \sin \phi_k \\ R_k \cos \theta_k \cos \phi_k \\ R_k \sin \theta_k \end{pmatrix}$$

where R_k is the distance of objects to the origin of the Cartesian coordinate system.

- d_T is the spacing of the transmit antennas in case the transmit array is an ULA.
- d_R is the spacing of the receive antennas in case the receive array is an ULA.

The geometry of one arbitrary transmit antenna, one arbitrary receive antenna and one object is shown in Fig. 3.4. The DOA of k^{th} object is estimated by a set of angle value (ϕ_k, θ_k) , where ϕ_k is the azimuth angle and θ_k is the elevation angle.

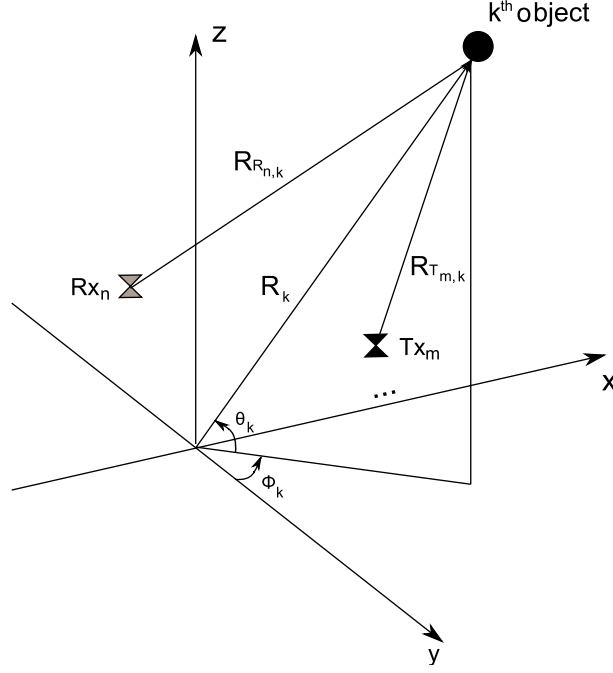


Fig. 3.4.: Arbitrary antenna geometry

In order to find the steering vector, the distance from the transmitters to object and back to the receivers has to be estimated. We start by calculating the distance between the m^{th} transmit antenna and the k^{th} object, where

$$\begin{aligned}
 R_{Tm,k} &= |-\mathbf{x}_{T,m} + \mathbf{r}_k| = \left| -\begin{pmatrix} x_{T,m} \\ y_{T,m} \\ z_{T,m} \end{pmatrix} + \begin{pmatrix} R_k \cos \theta_k \sin \phi_k \\ R_k \cos \theta_k \cos \phi_k \\ R_k \sin \theta_k \end{pmatrix} \right| \\
 &= (R_k^2 - 2R_k x_{T,m} \cos \theta_k \sin \phi_k - 2R_k y_{T,m} \cos \theta_k \cos \phi_k - 2R_k z_{T,m} \sin \theta_k + \\
 &\quad + x_{T,m}^2 + y_{T,m}^2 + z_{T,m}^2)^{1/2}
 \end{aligned} \tag{3.22}$$

Using the binomial theorem as explained in [1] to expand (3.22), $R_{Tm,k}$ can be approximated as

$$R_{Tm,k} \approx R_k - x_{T,m} \cos \theta_k \sin \phi_k - y_{T,m} \cos \theta_k \cos \phi_k - z_{T,m} \sin \theta_k + \frac{x_{T,m}^2 + y_{T,m}^2 + z_{T,m}^2}{2R_k} \tag{3.23}$$

The last term at the right hand side of (3.23) can be neglected due to the assumption that the object is in the far-field region, making $r_k \gg |\mathbf{x}_{T,m}|, |\mathbf{x}_{R,n}|$. Therefore, we have the estimated distance between m^{th} transmit antenna and the k^{th} object $\tilde{R}_{Tm,k}$ as:

$$\tilde{R}_{Tm,k} = R_k - x_{T,m} \cos \theta_k \sin \phi_k - y_{T,m} \cos \theta_k \cos \phi_k - z_{T,m} \sin \theta_k \tag{3.24}$$

Using the same analysis, the distance between the object and the n^{th} receiver can be obtained as

$$\tilde{R}_{Rn,k} = R_k - x_{R,n} \cos \theta_k \sin \phi_k - y_{R,n} \cos \theta_k \cos \phi_k - z_{R,n} \sin \theta_k \quad (3.25)$$

Therefore, the total traveling distance of the signal is

$$\begin{aligned} \tilde{R}_{Tm,k} + \tilde{R}_{Rn,k} = 2R_k - (x_{T,m} + x_{R,n}) \cos \theta_k \sin \phi_k - (y_{T,m} + y_{R,n}) \cos \theta_k \cos \phi_k - \\ - (z_{T,m} + z_{R,n}) \sin \theta_k \end{aligned} \quad (3.26)$$

The second to the fourth terms of the right hand side of (3.26) are actually the dot product of vectors $\mathbf{x}_{T,m}$ and $\mathbf{x}_{R,n}$ with the unit pointing vector \mathbf{u} from the radar system to the object in the three coordinates of the Cartesian system. Compared (3.3) and (3.26), again we can see clearly that the position of virtual antenna will be at $\mathbf{x}_{T,m} + \mathbf{x}_{R,n}$.

Now, the transmit steering vector \mathbf{v}_T depends on the the DOA of the received signals which is defined by (ϕ, θ) for the general case. Therefore, it can be written as a function dependent on (ϕ, θ) ,

$$\mathbf{v}_T(\phi, \theta) = \begin{pmatrix} \exp(-jk(x_{T,1} \cos \theta \sin \phi + y_{T,1} \cos \theta \cos \phi + z_{T,1} \sin \theta)) \\ \exp(-jk(x_{T,2} \cos \theta \sin \phi + y_{T,2} \cos \theta \cos \phi + z_{T,2} \sin \theta)) \\ \vdots \\ \exp(-jk(x_{T,N_T} \cos \theta \sin \phi + y_{T,N_T} \cos \theta \cos \phi + z_{T,N_T} \sin \theta)) \end{pmatrix} \quad (3.27)$$

Analyzing the receive steering vector \mathbf{v}_R in the same way, we have:

$$\mathbf{v}_R(\phi, \theta) = \begin{pmatrix} \exp(-jk(x_{R,1} \cos \theta \sin \phi + y_{R,1} \cos \theta \cos \phi + z_{R,1} \sin \theta)) \\ \exp(-jk(x_{R,2} \cos \theta \sin \phi + y_{R,2} \cos \theta \cos \phi + z_{R,2} \sin \theta)) \\ \vdots \\ \exp(-jk(x_{R,N_R} \cos \theta \sin \phi + y_{R,N_R} \cos \theta \cos \phi + z_{R,N_R} \sin \theta)) \end{pmatrix} \quad (3.28)$$

The virtual steering vector as defined in section 3.1 now becomes:

$$\mathbf{v}(\phi, \theta) = \mathbf{v}_T(\phi, \theta) \otimes \mathbf{v}_R(\phi, \theta) \quad (3.29)$$

In the following sections, the antenna geometry for the 2D radar is introduced, followed by the antenna geometry for the 3D radar. The virtual steering vector in both cases are also derived.

To avoid confusion of several categories of radar, in this project, two-dimensional, or 2D radars are referred to as the radar sets that provide only range and bearing (azimuth) information. The radar sets that provide range, bearing, and height (elevation) are called three-dimensional, or 3D radars. In the 3D radars, the information of height can be provided by the elevation angle.

3.3.1. Antenna Geometry for 2D Radar Imaging

Since 2D radar needs only the azimuth angle information, transmit and receive array can simply lie on one axis of the coordinate system. The geometry of receive and transmit antennas are demonstrated in Fig. 3.5. Here, the receive and transmit antennas are located on the x -axis of Cartesian coordinate. The antenna system and objects are on the $x - y$ plane.

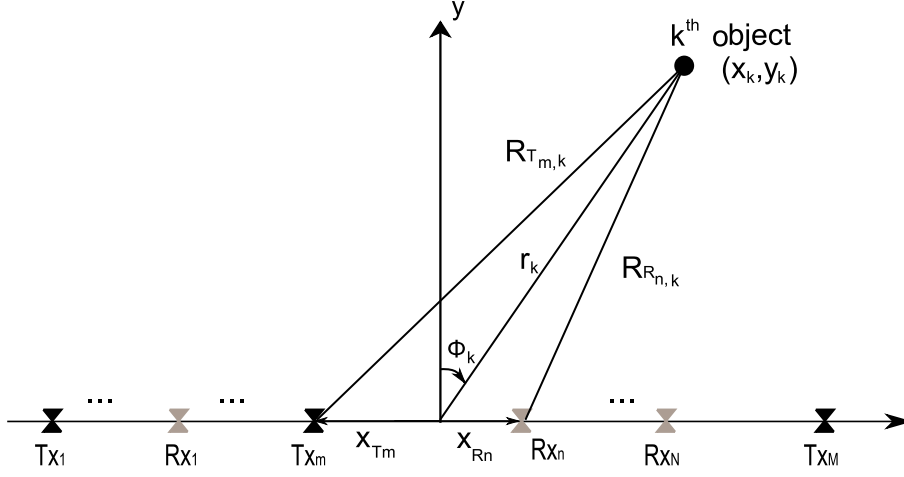


Fig. 3.5.: Antenna geometry for 2D Radar imaging

From the explanation in section 3.3 about the choice of antenna geometry for transmit and receive array, to achieve the highest number of virtual antennas and a contiguous region for the antenna aperture, we chose transmit and receive ULAs with $d_T = N_R d_R$ and $d_R = \lambda/2$, where λ is the wavelength of the transmitted signal. This correspond to the classical virtual array, which gives the largest basis as discussed in the previous section.

Fig. 3.6 shows the antenna pattern of the transmit, receive, and virtual arrays for the case $N_T = N_R = 4$. The receive antenna pattern has 1 main lobe and 2 side lobes within 180° . According to the antenna theory, grating lobes appear when the element spacing $d > \lambda/2$. It can be seen from Fig. 3.6 that the grating lobes appear in the transmit antenna pattern where $d_T = 4d_R = 2\lambda$. The position of the transmit antennas is organized in such a way that the grating lobes fall at the null of the receive antennas' radiation pattern. This means that the virtual array is the transmit radiation pattern shaped by the receive radiation pattern. It can also be seen that the 3dB beamwidth of the virtual array is much narrower than one of the receive array. This narrower beamwidth leads to a higher angular resolution. The detailed studies for this antenna geometry can be founded in [18].

In this antenna geometry, the elevation angle θ is equal to 0. The coordinate of the m^{th} transmit

antenna is:

$$\begin{pmatrix} \left(\frac{N_T+1}{2} - m\right) d_T \\ 0 \\ 0 \end{pmatrix}$$

The coordinate of the n^{th} receive antenna is:

$$\begin{pmatrix} \left(\frac{N_R+1}{2} - n\right) d_R \\ 0 \\ 0 \end{pmatrix}$$

Substituting the coordinates of the transmit and receive antennas and $\cos \theta = 1$ into (3.27) and (3.28) respectively, the virtual steering vector can be expressed as

$$\mathbf{v}(\phi) = \left(1 \quad \exp\left(j\frac{f_c}{c}d_R \sin \phi\right) \quad \cdots \quad \exp\left(j(N_T N_R - 1)\frac{f_c}{c}d_R \sin \phi\right) \right)^T \quad (3.30)$$

3.3.2. Antenna Geometry for 3D Radar Imaging

In the case of the 3D radar imaging approach, the transmit and receive antenna arrays are arranged orthogonally to each other [10] as shown in Fig. 3.7. The element spacing of the transmit and receive array is chosen as $d_T = d_R = \lambda/2$. The equivalent virtual array is shown in Fig. 3.8. Note that the element numbers of transmit and receive arrays should be equal to have the same angular resolution for azimuth and elevation angle estimation. For the 3D radar, the antenna geometry or the d_T and d_R can be optimized to achieve a better angular resolution for DOA estimation, however this optimization work is not in the scope of this thesis.

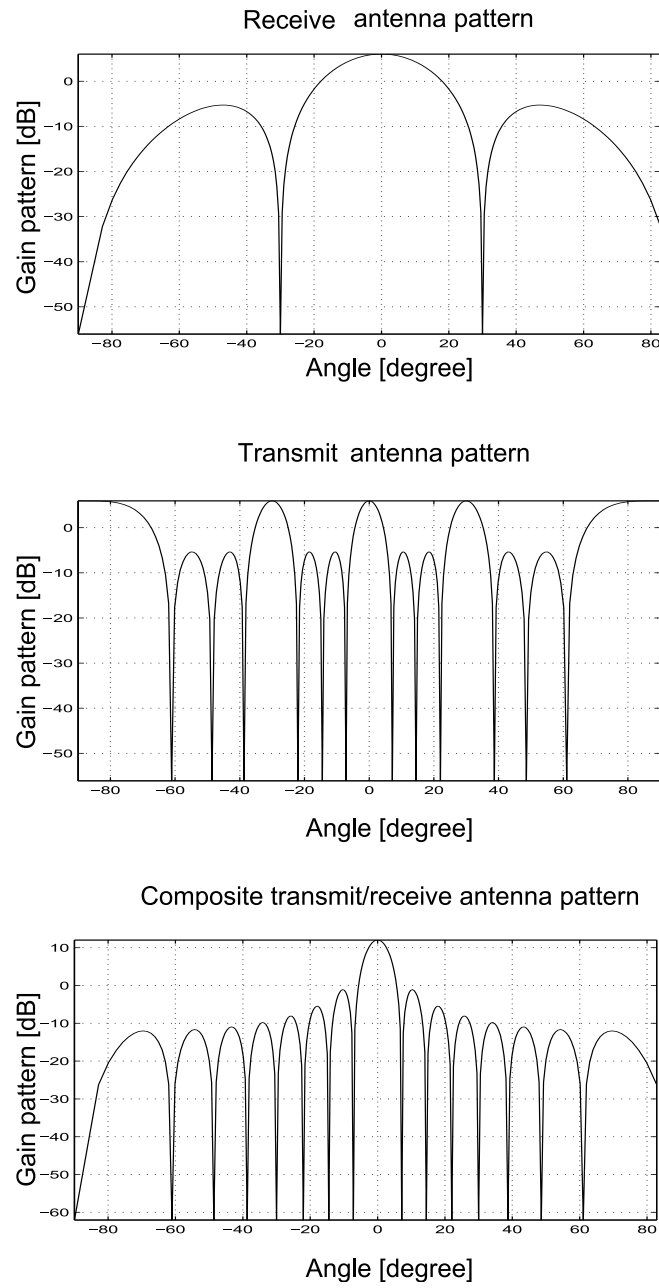


Fig. 3.6.: Beam pattern for $N_T = N_R = 4$ with $d_T = 2\lambda$ and $d_R = \lambda$

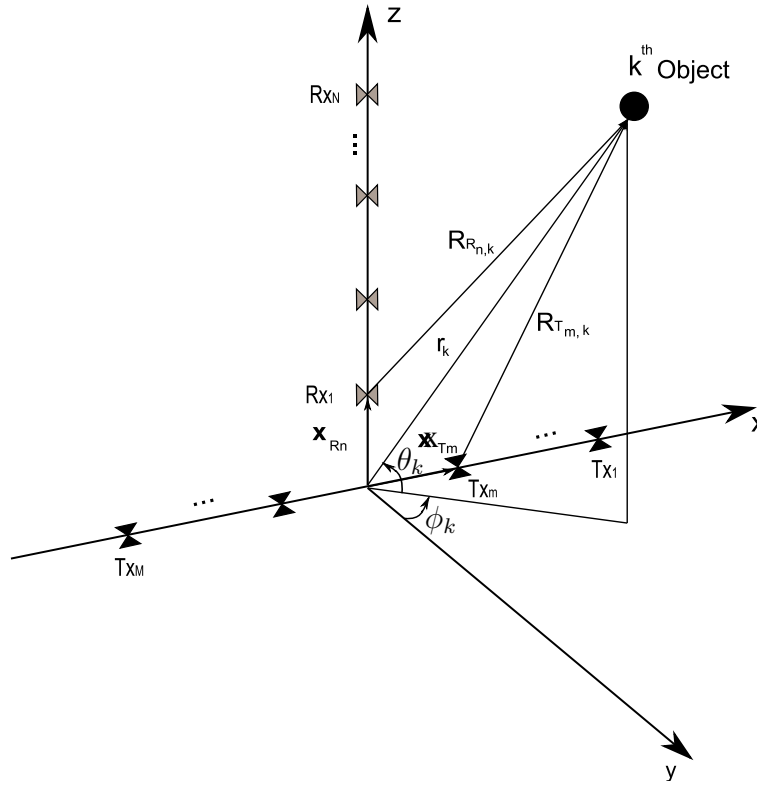


Fig. 3.7.: Antenna geometry for 3D Radar imaging

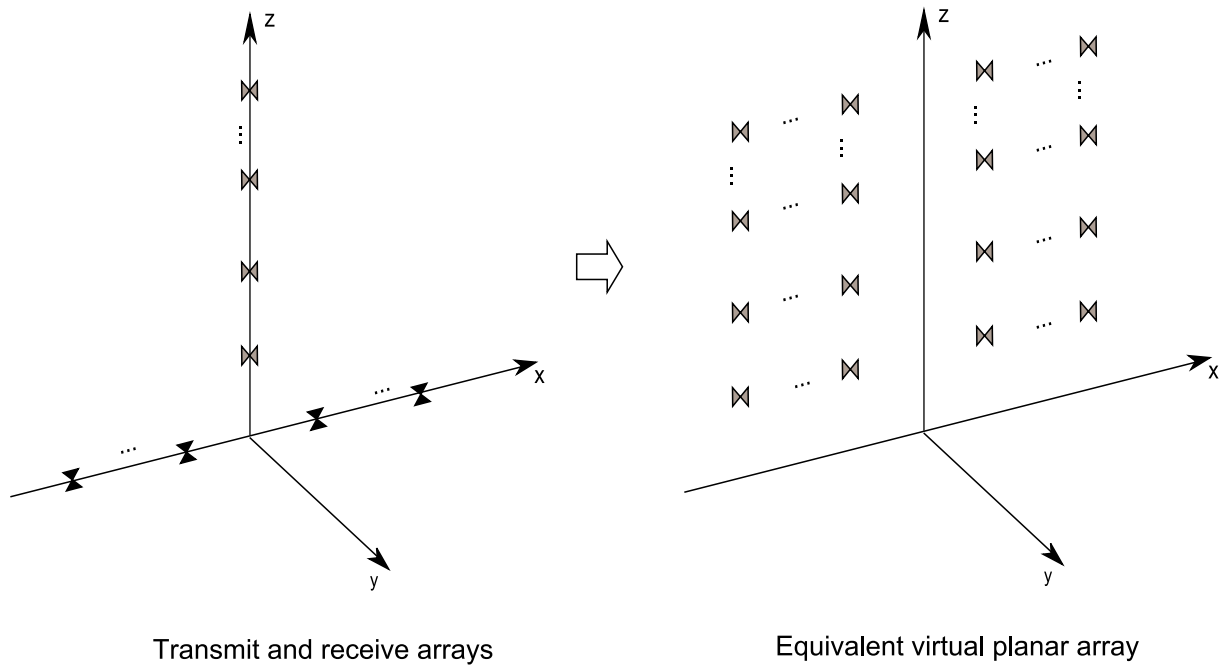


Fig. 3.8.: Equivalent virtual array

The coordinates of the m^{th} transmit antenna is

$$\begin{pmatrix} \left(\frac{N_T+1}{2} - m\right) d_T \\ 0 \\ 0 \end{pmatrix}$$

The coordinate of the n^{th} receive antenna is:

$$\begin{pmatrix} 0 \\ 0 \\ (N_R + 1 - n)d_R \end{pmatrix}$$

The transmit steering vector can be generated as

$$\mathbf{v}_T(\phi, \theta) = \left(1 \quad \exp\left(j\frac{f_c}{c}d_T \cos \theta \sin \phi\right) \quad \cdots \quad \exp\left(j(N_T - 1)\frac{f_c}{c}d_T \cos \theta \sin \phi\right)\right)^T \quad (3.31)$$

while the receive steering vector is

$$\mathbf{v}_R(\phi, \theta) = \left(1 \quad \exp\left(j\frac{f_c}{c}d_R \sin \phi\right) \quad \cdots \quad \exp\left(j(N_R - 1)\frac{f_c}{c}d_R \sin \phi\right)\right)^T \quad (3.32)$$

Hence, the virtual steering array is

$$\mathbf{v} = \mathbf{v}_R \otimes \mathbf{v}_T \quad (3.33)$$

3.4. MIMO Signal Waveform and Radar Processing

In the section 3.1.2, a signal model for MIMO radar has been derived. However, the waveform of the transmitted signal has not taken into account. In order to create a set of uncorrelated transmitted signals, the conventional structure of the OFDM signal used in the SISO RadCom system has to be modified [21]. Instead of sending the whole OFDM carriers, the carriers are distributed among the different users by using a regular carrier assignment scheme.

Fig. 3.9 shows the assignment scheme for a MIMO system with $N_T = 3$. For example, the whole OFDM spectrum consists of only 6 subcarriers/subchannels. These subcarriers have to be divided among 3 transmitters. Therefore, transmitter 1 gets the 1st and 4th, transmitter 2 getting the 2nd and 5th and transmitter 3 gets the 3rd and 6th. In general, the classical OFDM signal have all carriers active while the modified signal has only every N_T^{th} carrier active. This carrier assignment keeps the orthogonality between each transmitters. The new modified signals are called the *spectrally interleaved multi-carrier signals*. This method has been patented in [25].

The transmit signal for case of multiple transmitters using the OFDM spectrally interleaved waveform can be described as

$$x_m(t) = \sum_{\mu=0}^{N_{sym}-1} \sum_{n=0}^{N_{c,mod}-1} d_{Tx}(\mu N_{c,mod} + n) \exp(j2\pi(u + nN_{ch})\Delta f t) \text{rect}\left(\frac{t - \mu T}{T}\right) \quad (3.34)$$

where $N_{c,mod} = N_c/N_{ch}$ is the number of carriers remaining in the modified signal.

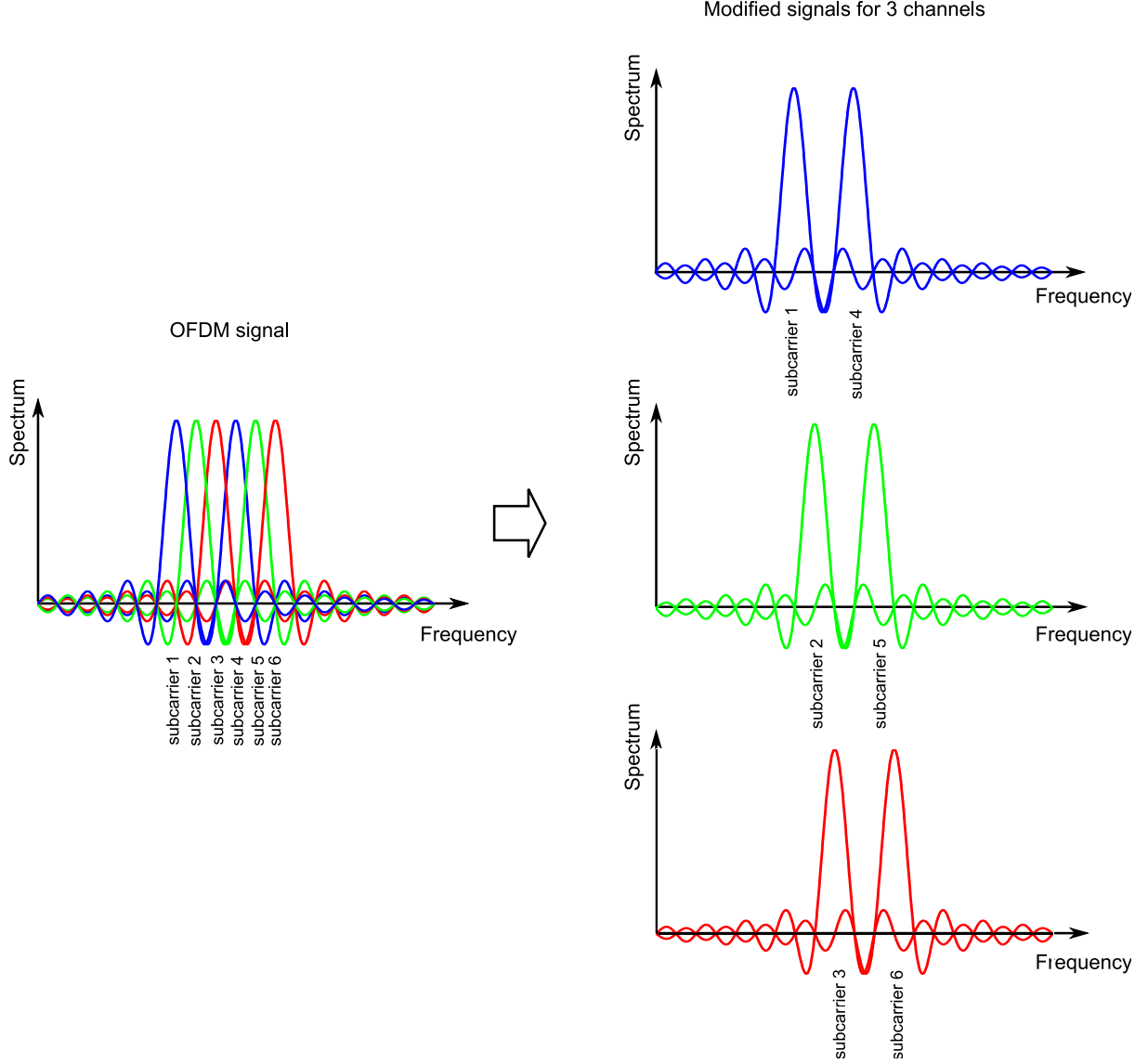


Fig. 3.9.: Regular subcarrier assignment to generate orthogonal signals

If the transmit signal $x_m(t)$ is reflected back from an object in the distance R moving with relative

velocity v_{rel} , the received signal $y(t)$ becomes

$$y(t) = \sum_{\mu=0}^{N_{sym}-1} \sum_{n=0}^{N_{c,mod}-1} a(\mu, n) d_{Tx}(\mu N_{c,mod} + n) \exp \left(j2\pi(u + nN_{ch})\Delta f \left(t - \frac{2R}{c_0} \right) \right) \cdot \exp \left(j2\pi\mu T_{OFDM} \frac{2v_{rel}f_c}{c_0} \right) \text{rect} \left(\frac{t - \mu T}{T} \right) \quad (3.35)$$

The received modulation symbol d_{Rx} , including the amplitude and phase rotation, is expressed as

$$d_{Rx}(\mu N_{c,mod} + n) = a(\mu, n) d_{Tx}(\mu N_{c,mod} + n) \exp \left(j2\pi(u + nN_{ch})\Delta f \left(t - \frac{2R}{c_0} \right) \right) \cdot \exp \left(j2\pi\mu T_{OFDM} \frac{2v_{rel}f_c}{c_0} \right) \quad (3.36)$$

Following (2.21), (2.22) and (2.23), the range and Doppler estimation can be expressed as:

$$d_{div}(\mu N_{c,mod} + n) = \frac{d_{Rx}(\mu N_{c,mod} + n)}{d_{Tx}(\mu N_{c,mod} + n)} = a(\mu, n) \cdot k_R(n) \cdot k_D(n) \quad (3.37)$$

with

$$k_R(n) = \exp \left(-j2\pi\mu\Delta f \frac{2R}{c_0} \right) \exp \left(-j2\pi nN_{ch}\Delta f \frac{2R}{c_0} \right) \quad (3.38)$$

and

$$k_D(n) = \exp \left(j2\pi\mu T_{OFDM} \frac{2v_{rel}f_c}{c_0} \right) \quad (3.39)$$

The second phase term of $k_R(n)$ in (3.38) depends on the index n of the subcarrier and the number of channels N_{ch} . The procedure to determine the distance is unchanged by implementing the inverse discrete Fourier transform. The first term in (3.38) causes a phase rotation along the frequency axis causing a misalignment of the FFT bins from the template FFT bins of the original transmit signal. Therefore the recovered modulation symbol is not a clean signal but also has some contributions from other modulation symbols from the other subcarriers, also called the inter-carrier-interference (ICI). However, this has no effect on the result of the range estimation since the detection of objects only depends on the amplitude or intensity of IFFT result. Without the ICI, the recovered modulation symbol will look sharper due to the impulse like peak. With ICI though, the peak is like a narrow Gaussian pulse therefore causing the artifacts around the actual peak.

Due to the rapid rotation of the phase in k_R , it is obvious that the maximum unambiguous range in the application of the modified waveform is reduced by a factor of N_{ch} . A peak will appear as a result of IDFT in the following condition:

$$k = \left\lceil \frac{N_{ch} 2R \Delta f N_{c,mod}}{c_0} \right\rceil, k = 0, \dots, N_{c,mod} - 1 \quad (3.40)$$

The maximum unambiguous range in this case is

$$R_{u,mod} = \frac{c_0}{2\Delta f N_{ch}} = \frac{c_0 T}{2N_{ch}} \quad (3.41)$$

This means that in practical applications, the number of channels N_{ch} should be chosen correctly to fit the desired detectable range. In the next step, we will consider the effect of the modified signal on the processing gain and SNR. The processing gain in the SISO RadCom system is the product of the lengths of the two discrete Fourier transforms. Since the number of subcarriers for each channel is reduced, the gain processing is reduced accordingly and is equal to

$$G_{p,mod} = N_{c,mod} N_{sym} = \frac{G_p}{N_{ch}} \quad (3.42)$$

The SNR from the radar equation in this case is equal to

$$\begin{aligned} SNR_{mod} &= \frac{P_{Rx} G_{p,mod}}{P_N} = \frac{P_{Tx,EIRP} G_{Rx} G_{p,mod} \lambda^2 \sigma}{(4\pi)^3 R^4 k T_{abs} (B/N_{ch}) F} \\ &= \frac{P_{Tx,EIRP} G_{Rx} G_p \lambda^2 \sigma}{(4\pi)^3 R^4 k T_{abs} B F} \end{aligned} \quad (3.43)$$

The SNR is equivalent to the result of the SISO OFDM signal. This means that, using the modified signal leads to no reduction in the SNR. Table 3.1 summarizes all the parameters in the MIMO radar system for $N_R = 4$.

Symbol	Parameter	Value
f_c	Carrier frequency	24 GHz
N_{ch}	Number of channels	4
$N_{c,mod}$	Number of carriers per user	256
Δf	Subcarrier spacing	90.909 kHz
T	Elementary OFDM symbol duration	11 μ s
T_{CP}	Cyclic prefix duration	1.365 μ s
T_{sym}	Transmit OFDM symbol duration	12.375 μ s
B	Total signal bandwidth	93.1 MHz
Δr	Range resolution	1.61 m
r_{max}	Maximum unambiguous range	412.5 m
v_{max}	Maximum unambiguous velocity	± 252.5 m/s
M	Number of evaluated symbols	256
Δv	Velocity resolution	1.97 m/s
$G_{p,mod}$	Processing gain	45.2 dB

Table 3.1.: MIMO OFDM-based system parameters

4. DOA Estimation

There are several classes of array-based DOA estimation techniques. Among them, the two most common techniques are the subspace based techniques and the maximum likelihood (ML) techniques. Each technique has its own advantages and disadvantages [14]. Although the ML techniques offer improved performance under low SNR over subspace-based ones, they are usually hard to implement and are computationally very intensive. The subspace-based techniques, on the other hand, are simple to implement with many modified algorithms to fit the scenario while providing a high resolution of DOA estimation.

Within the subspace based techniques, MUSIC is one of the most widely studied. In a performance evaluation [17], MIT's Lincoln Laboratory concluded that among high-resolution algorithms, MUSIC is one of the most promising. In this chapter, the MUSIC algorithm is introduced and analyzed. Next, a complete MIMO radar system simulation in Matlab is described. The MUSIC algorithm is implemented to estimate the bearing information for the 2D and 3D radars. The results are then analyzed.

4.1. MUSIC algorithm

In this section, we incorporate the signal model as described in section 3.2 into the MUSIC algorithm. The original MUSIC algorithm was proposed by Schmidt in [17]. This technique is based on separating the eigenstructure of the covariance matrix of the received signals with the assumption that the noise is orthogonal to the signals. Therefore, first, consider the signal as described in section 3.2:

$$\mathbf{Y} = \mathbf{S}\mathbf{X} + \mathbf{E}$$

where \mathbf{Y} has dimension of $N_R \times 1$. We form the $N_R \times N_R$ covariance matrix of \mathbf{Y} as:

$$\mathbf{R}_{yy} = E\{\mathbf{Y}\mathbf{Y}^H\} = \mathbf{S}E\{\mathbf{X}\mathbf{X}^H\}\mathbf{S}^H + E\{\mathbf{E}\mathbf{E}^H\} = \mathbf{S}\mathbf{R}_{xx}\mathbf{S}^H + \sigma_n^2\mathbf{I} \quad (4.1)$$

where

- $E()$ denotes the expected value (or expectation) of the matrix
- Matrix \mathbf{S}^H is the Hermitian transpose of matrix \mathbf{S} as explained in section A.3.
- \mathbf{R}_{xx} is the signal correlation matrix $E\{\mathbf{X}\mathbf{X}^H\}$
- σ_n^2 is the variance of the white Gaussian noise
- \mathbf{I} is an identity matrix

The eigenvalues of \mathbf{R}_{yy} , as defined in matrix algebra are the values $\{\lambda_0, \dots, \lambda_{N_R-1}\}$ that render

$$\det(\mathbf{R}_{yy} - \lambda_i \mathbf{I}) = 0 \quad (4.2)$$

where \det is the determinant of the matrix.

Substituting (4.1) into (4.2), we have

$$\det(\mathbf{S}\mathbf{R}_{xx}\mathbf{S}^H + \sigma_n^2 \mathbf{I} - \lambda_i \mathbf{I}) = \det(\mathbf{S}\mathbf{R}_{xx}\mathbf{S}^H - (\lambda_i - \sigma_n^2) \mathbf{I}) = 0 \quad (4.3)$$

Defining $\nu_i, i = 0, \dots, N_R - 1$, is the eigenvalues of $\mathbf{S}\mathbf{R}_{xx}\mathbf{S}$, the eigenvalues of \mathbf{R}_{yy} are equal to

$$\lambda_i = \nu_i + \sigma_n^2 \quad (4.4)$$

As explained in section 3.3, the matrix \mathbf{S} contains K steering vectors for K different objects. Since the steering vector depends on antenna geometry and object positions, they are linearly independent because none of them can be written as a linear combination of the other vectors. When the number of objects K is less than the number of receive array elements N_R , the $N_R \times N_R$ matrix $\mathbf{S}\mathbf{R}_{xx}\mathbf{S}^H$ is positive semi-definite with the rank of K . Note that a positive semi-definite has non negative eigenvalues. This is one of the properties of a covariance matrix. The rank of the $N_R \times N_R$ matrix $\mathbf{S}\mathbf{R}_{xx}\mathbf{S}^H$ is then equal to the number of linear independent steering vectors as defined in linear algebra. It means that $N - K$ eigenvalues of $\mathbf{S}\mathbf{R}_{xx}\mathbf{S}^H$ are zero. Therefore, by sorting the eigenvalues of \mathbf{R}_{yy} such that λ_0 is the largest eigenvalue, and λ_{N-1} is the smallest eigenvalue, we have

$$\lambda_K, \dots, \lambda_{N-1} = \sigma_n^2 \quad (4.5)$$

The eigenvalues of the covariance matrix \mathbf{R}_{yy} can be divide into two groups: K values related to the signals and $N_R - K$ values related to the noise, which is orthogonal to the signal. In practical cases, all the eigenvalues corresponding to the noise subspace are not identical. By using *a priori* knowledge of the received signal to set some threshold, an estimate of the number of objects \hat{K} can be obtained to separate the eigenstructure of \mathbf{R}_{yy} .

The eigenvector of matrix \mathbf{R}_{yy} associated with a particular eigenvalue, λ_i , is the vector \mathbf{q}_i . The relation between matrix \mathbf{R}_{yy} , the eigenvalue, λ_i , and the eigenvector, \mathbf{q}_i , can be expressed as:

$$(\mathbf{R}_{yy} - \lambda_i \mathbf{I})\mathbf{q}_i = 0 \quad (4.6)$$

For the eigenvectors associated with the $N_R - K$ smallest eigenvelues, subsituting (4.5) into (4.6), we have (4.6) written as follows:

$$(\mathbf{R}_{yy} - \sigma_n^2 \mathbf{I})\mathbf{q}_i = (\mathbf{S}\mathbf{R}_{xx}\mathbf{S}^H + \sigma_n^2 \mathbf{I} - \sigma_n^2 \mathbf{I})\mathbf{q}_i = \mathbf{S}\mathbf{R}_{xx}\mathbf{S}^H \mathbf{q}_i = 0 \quad (4.7)$$

Since $\mathbf{S}\mathbf{R}_{xx}\mathbf{S}^H \neq 0$, we have:

$$\mathbf{S}^H \mathbf{q}_i = 0 \quad (4.8)$$

It means that the eigenvectors related to the noise $N_R - K$ smallest eigenvalues are orthogonal to the K steering vectors that make up the matrix \mathbf{S} . Therefore, by estimating the steering vectors which are most nearly orthogonal to the eigenvectors associated with the $N_R - K$ eigenvalues of \mathbf{R}_{yy} , the DOA can be estimated. The eigenvector of \mathbf{R}_{yy} can be separated into two orthogonal subspaces, the signal subspace and the noise subspace as shown in Fig. 4.1. For example, the one-dimensional noise subspace is spanned by the noise eigenvector q_3 and the signal subspace is spanned by the signal eigenvectors q_1 and q_2 . The steering vectors corresponding to the DOA also lie in the signal subspace. Therefore, they are also orthogonal to the noise subspace. To create the noise subspace, the matrix including the eigenvectors from the noise subspace can be formed as:

$$\mathbf{Q}_n = [\mathbf{q}_K \quad \mathbf{q}_{K+1} \quad \dots \quad \mathbf{q}_{N_R-1}] \quad (4.9)$$

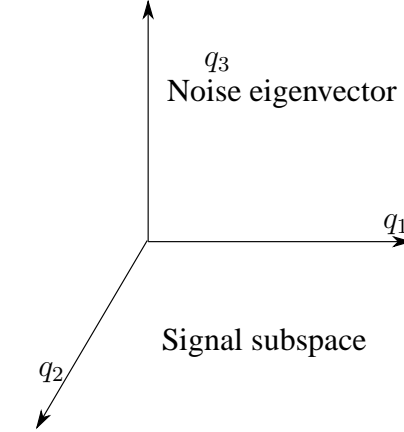


Fig. 4.1.: Geometrical interpretation of the orthogonality of the signal and noise subspaces.

Since the steering vectors corresponding to signal components are orthogonal to the noise subspace eigenvectors, $\mathbf{v}^H(\phi, \theta) \mathbf{Q}_n \mathbf{Q}_n^H \mathbf{v}(\phi, \theta) = 0$ for azimuth angle ϕ and elevation angle θ corresponding to the DOA of the received signal. Thus the DOAs of the multiple incident signals can be estimated by locating the peaks of a MUSIC spatial spectrum given by

$$P_{MUSIC}(\phi, \theta) = \frac{1}{\mathbf{v}^H(\phi, \theta) \mathbf{Q}_n \mathbf{Q}_n^H \mathbf{v}(\phi, \theta)} \quad (4.10)$$

Orthogonality between $\mathbf{a}(\phi)$ and \mathbf{V}_n will minimize the denominator and therefore, it will give rise to peaks in the MUSIC spectrum. The \hat{K} largest peaks in the MUSIC spectrum correspond to the directions of arrival of the signals arriving on the array.

In the case of the MIMO radar, since the received signal can be separated as explained in section 3.1 and section 3.2, the model represented in (3.16) is used. The implementation of the MUSIC algorithm for this model can be explained in the same analysis. However, because virtual array increases the number of antennas significantly, the angular resolution, which is proportional to

the number of receive antennas, also increases. At the same time, since the covariance matrix's dimension of the received signals is larger $N_T N_R \times N_T N_R$, the computation time takes longer than the conventional receive array. The MUSIC spatial spectrum for MIMO radar can be described as:

$$\hat{P}_{MUSIC}(\phi, \theta) = \frac{1}{\mathbf{v}_T^H(\phi, \theta) \otimes \mathbf{v}_R^H(\phi, \theta) \hat{\mathbf{Q}}_n \hat{\mathbf{Q}}_n^H \mathbf{v}_T(\phi, \theta) \otimes \mathbf{v}_R(\theta, \phi)} \quad (4.11)$$

In the next section, the implementation of MUSIC algorithm for the OFDM-based MIMO radar will be explained and analyzed.

4.2. Implementation of the Signal Model in Matlab

To analyze the capability of the system, a complete system model of an OFDM-based MIMO Radar has been implemented in Matlab. The system configuration consists of the OFDM transmitters, receivers, channel model and the radar processing unit. The system parameters are adjustable in all blocks. The structure of individual blocks will be discussed in the following sections.

4.2.1. Transmitters

In this block, the number of transmitters N_T and receivers N_R are adjustable. Fig. 4.2 shows the block diagram of the operational functions for one OFDM symbol in the OFDM transmitters. One OFDM symbol consist of N_c modulation symbols. One OFDM frame consists of N_{sym} OFDM symbols. The first block is a source of random binary bits with the length of $2N_c N_{sym}$. The sequence of bits is then modulated using the quadrature phase shift keying (QPSK) method. QPSK uses four points on the constellation diagram, therefore it can encode two bits per modulation symbol. The individual modulation symbols are then demultiplexed into N_c parallel streams/subchannels. An IFFT with the length of N_c is computed for each of the symbols. After that, a CP is inserted. The sampling rate of the baseband signal is equivalent to the clock of modulation symbol N_c/T . Up to this step, all the subcarriers are active. The subcarriers are then separated to different transmitters using spectral masking to achieve N_T orthogonal transmit signals for N_T transmitters. Finally, each part are upconverted to the carrier frequency of 24 GHz.

4.2.2. Channel

For the modeling of the wave propagation in a channel, a point scatter model is used. Depending on the distance R and the relative velocity v_{rel} of each object, a complex exponential with a phase rotation caused by range and Doppler effect are added to the transmit signals. The Doppler frequency experienced by the reflected signal is twice the amount of a direct signal, which is expressed by

$$f_D = \frac{2v_{rel}}{\lambda} \quad (4.12)$$

Consider the case of K objects at position \mathbf{r}_k and $\mathbf{v}_{rel,k}$, the received signal matrix \mathbf{Y} in a noisy channel is expressed as

$$\mathbf{Y} = \sum_{k=1}^K a_{tk} \exp \left(-j \frac{2\pi f_c}{c} \mathbf{u}_k \cdot \mathbf{r} \right) \exp \left(-j \frac{2\pi f_c}{c} \mathbf{u}_k \cdot 2\mathbf{v}_{rel} t \right) \mathbf{v}_R(\mathbf{u}_k) \mathbf{v}_T^T(\mathbf{u}_k) \mathbf{X} + \mathbf{E} \quad (4.13)$$

From (2.7), the attenuation factor a_t can be expressed as:

$$a_t = \sqrt{\frac{G_T G_R \lambda^2 \sigma_p}{(4\pi)^3 R_p^4}} \quad (4.14)$$

Finally, the noise model at the receiver is modeled as additive white Gaussian noise (AWGN).

4.2.3. Receivers

Fig. 4.3 shows the basic scheme of the receiver. The first step after the receive antennas is the demodulation of the RF signal to baseband. After that, the cyclic prefix is removed. An FFT is then performed to obtain the received symbols. After this part, the received symbols are then compared with the transmitted symbols for radar processing.

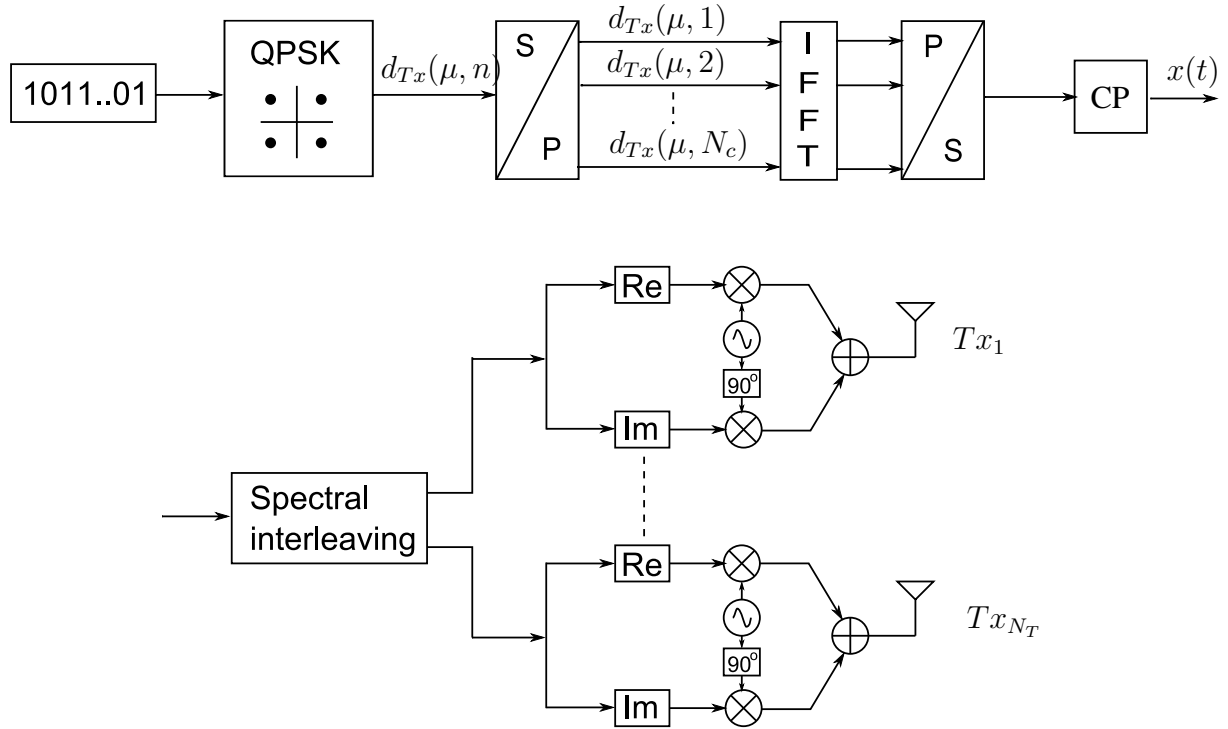


Fig. 4.2.: OFDM basic transmitter scheme

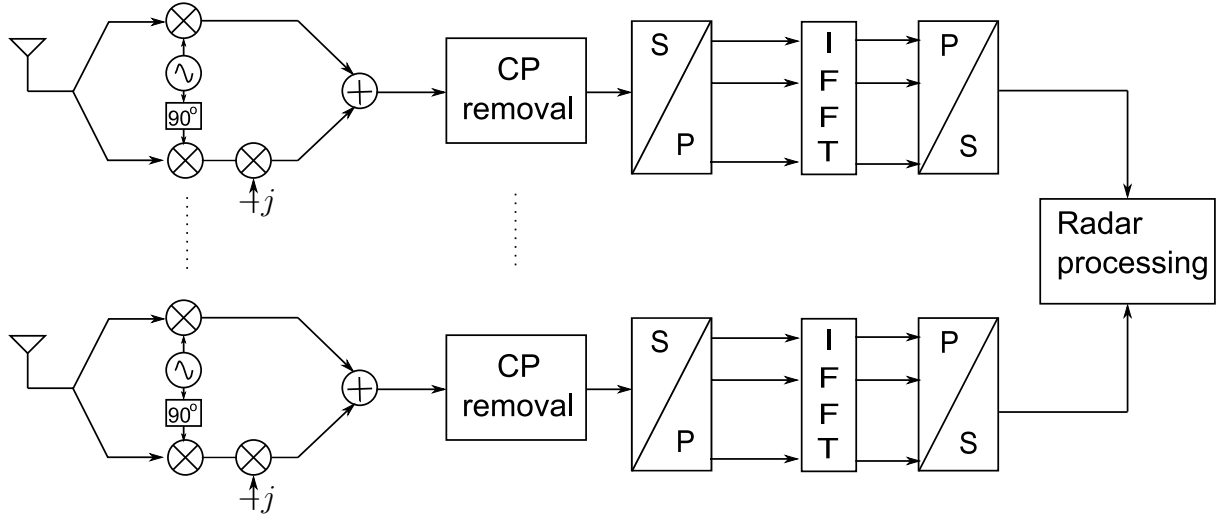


Fig. 4.3.: OFDM basic receiver scheme

4.2.4. Radar processing

The received signal for all the receivers is put in a 3D matrix with the dimension $N_c \times N_{sym} \times N_R$. Since the transmitted signals are orthogonal, signal separation by using the same spectral mask can be applied at each receiver to separate them to N_T signals. That is to say, there are N_T received signals at every receiver. After that, the 3D matrix with the dimension $N_c \times N_{sym} \times N_T N_R$ is formed as shown in Fig. 4.4. The next step is calculate the MUSIC spatial spectrum as described in section 4.1. The calculation to perform the MUSIC algorithm is described step by step.

1. Perform an FFT with length N_{sym} along the row and an IFFT with length N_c along the column. Based on the peak appearing after the operations, the range and velocity profiles of objects can then be estimated. This step has been discussed in section 2.3.
2. Estimate the velocity and range of the objects. The DOA search for objects is only applied in the range and velocity where objects are detected. This estimation is based on the setting of a threshold. If the signal level in each range and velocity is larger than the threshold value, an object is considered to be existing in this cell or the matrix.

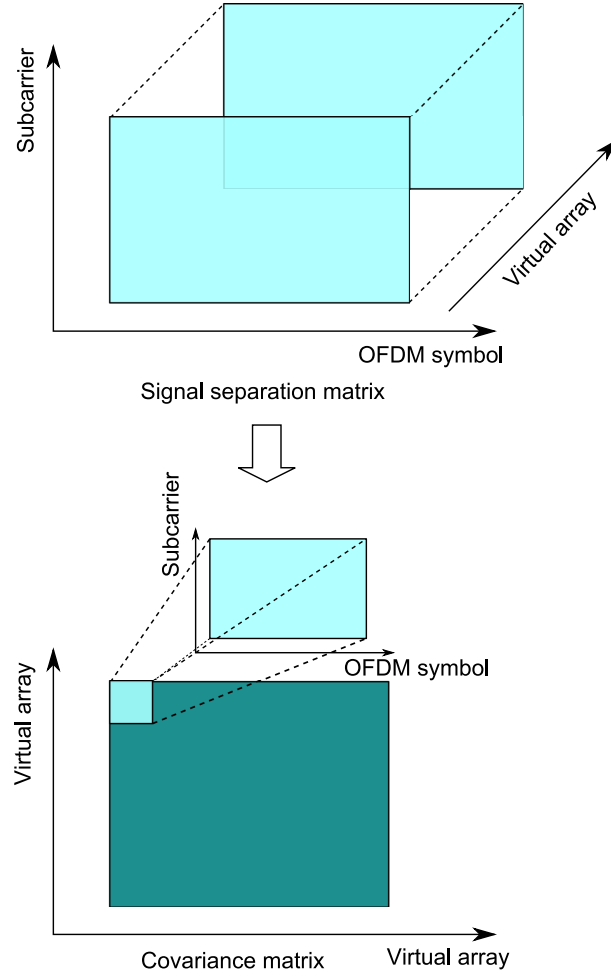


Fig. 4.4.: Representation of covariance matrix of the received signals

3. Calculate the covariance matrix of the received signal matrix between each virtual antennas. The covariance matrix is shown in Fig. 4.4 with the dimension $N_T N_R \times N_T N_R$. Since this is a 4D matrix, we can visualize each element of the 2D matrix as containing one 2D matrix (of range and velocity) with the dimension $N_c \times N_{sym}$.
4. The eigenvalues and eigenvectors of only the detected range and velocity are calculated. In other words only the rows and columns of the OFDM frame that contains the object (in range and velocity) are extracted. As such, depending on the number of objects detected, the matrix $N_c \times N_{sym}$ within the covariance matrix \mathbf{R}_{yy} changes size. However, by estimating first the range and velocity of possible objects, the calculation can be reduced instead of searching DOA in the whole original covariance matrix.
5. A threshold is set to search again among the eigenvalues for the number of possible objects in each distance and velocity.
6. Form the virtual steering vectors as shown in section 3.3. The steering vectors are different for 2D and 3D radars.
7. Compute the MUSIC spectrum as shown in section 4.1 and generate the radar image using

(4.11).

4.3. Simulation results

In this section, the simulation results are given to demonstrate the performance of the MUSIC algorithms presented previously.

4.3.1. 2D Radar Imaging

Consider a $4\text{Tx} \times 4\text{Rx}$ MIMO radar system where Tx stands for transmitter and Rx stands for receiver. The antenna geometry has been mentioned in section 3.3. The element spacing is $d_R = \lambda/2$ and $d_T = N_R d_R = 2\lambda$. All of the objects are point scatterers. The objects are listed in the Table 4.1. The RCS of each point scatterers can be defined separately. For automotive radar applications, the RCS of objects are usually around 10 dBm^2 , therefore, the RCS for all objects are set to be 10 dBm^2 . The time delay, phase shift and attenuation of the reflected signal are calculated. A white Gaussian noise is added and the SNR = 5 dB at the receiver. The step of steering vector used is 0.01 rad or 0.57° .

Object	Distance [m]	Relative velocity [m/s]	Azimuth [deg]
A	20	-10	10
B	20	30	30
C	50	20	-40
D	50	20	-35

Table 4.1.: List of objects in the simulation scenario of 2D radar imaging

Fig. 4.5 shows a volumetric representation of the radar image where the x -axis represents the azimuth in degree, y -axis, the relative velocity in [m/s] and z -axis, the distance of detected objects in [m]. The distances of detected objects can clearly be identified from the slice of the volumetric representation.

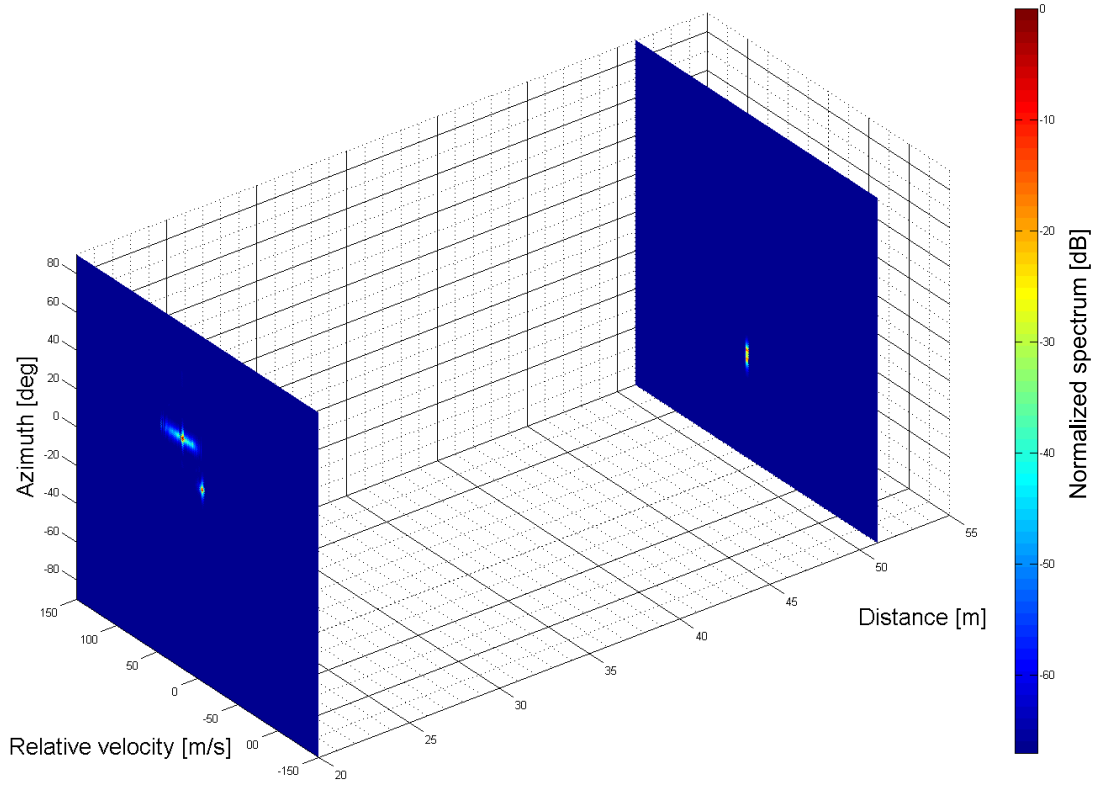


Fig. 4.5.: Volumetric representation

Fig. 4.6 and Fig. 4.7 shows the separate radar images detected at distance 20 m and 50 m respectively. In Fig. 4.6, artifacts appears the image of object A and B along the relative velocity axis due to the typical Fourier transform sidelobes in step 1 of the radar processing as mentioned in section 4.2.4. The grids were plotted from the point with the highest value of MUSIC spectrum within the object representation in the radar image. Since the MUSIC algorithm gives radar image of the objects but not the exact value of estimated parameters, the angular resolution which is dependent on the virtual steering vector plays an important role for the separate visualization of objects located angularly close to each other.

Fig. 4.7 shows the separability of objects at the same distance, with the same relative velocity but with a 5° difference of azimuth angles. The two objects at distance 50 m are fully separable within 5° . A $4\text{Tx} \times 4\text{Rx}$ system performs similarly to a $1\text{Tx} \times 16\text{Rx}$ and provide enough azimuth resolution. The MIMO OFDM-based radar system with the capability to detect range, velocity and azimuth is suitable for automotive radars. In addition, the antenna geometry is also suitable for automotive use due to its compact size at 24 GHz.

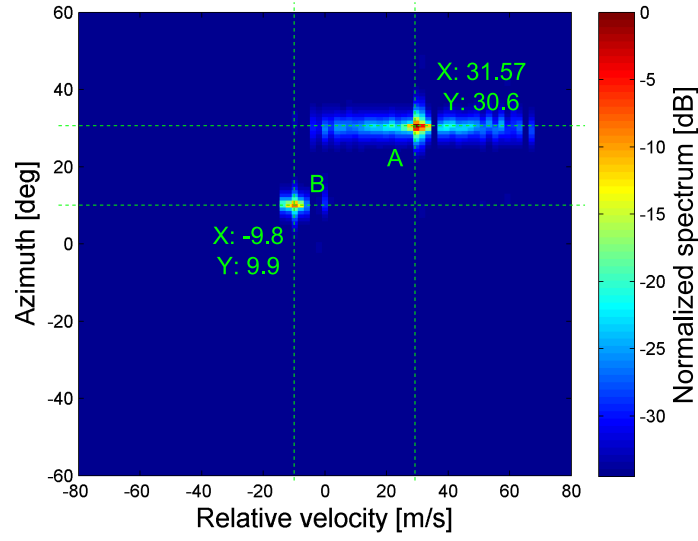


Fig. 4.6.: Radar image for objects at distance $d = 20$ m

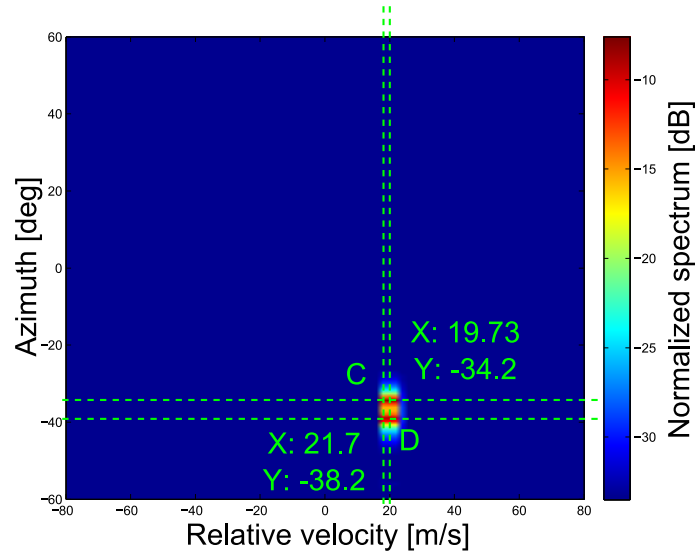


Fig. 4.7.: Radar image for objects at distance $d = 50$ m

4.3.2. 3D Radar Imaging

In this project, the SISO RadCom was initially parameterized for automotive applications. However by extending the configuration to a MIMO system, we try to expand the capability of object localization to other applications. As mentioned in chapter 1, the ITS system also require radars to detect objects with height. Therefore, the 2D radar is modified to become a 3D radar. The $4\text{Tx} \times 4\text{Rx}$ antenna geometry may be sufficient for automotive applications but $8\text{Tx} \times$

8Rx antenna geometry is used here as a reference to compare the performance of MUSIC algorithm.

Consider a $8\text{Tx} \times 8\text{Rx}$ MIMO radar system, where the antenna geometry are arranged as mentioned in 3.3.2. The element spacing of transmit and receive array is chosen to be $d_T = d_R = \lambda/2$. The objects are listed in Table 4.1 and the $\text{SNR} = 5 \text{ dB}$ at the receiver. The step of the steering vector in both the azimuth and elevation angles used is 0.01 rad or 0.57° .

Object	Distance [m]	Azimuth [deg]	Elevation [deg]
A	10	20	10
B	17	25	17
C	35	20	-30
D	35	34	-30
E	50	40	20
F	50	40	34

Table 4.2.: List of objects in the simulation scenario of 3D radar imaging

Fig. 4.8 shows the volumetric representation of the radar image where x -axis represents the estimated elevation angle in degree, y -axis, the azimuth angle in degree and z -axis, the distance of detected objects in [m]. The distances of detected objects can be clearly identified from the slice of the volumetric representation.

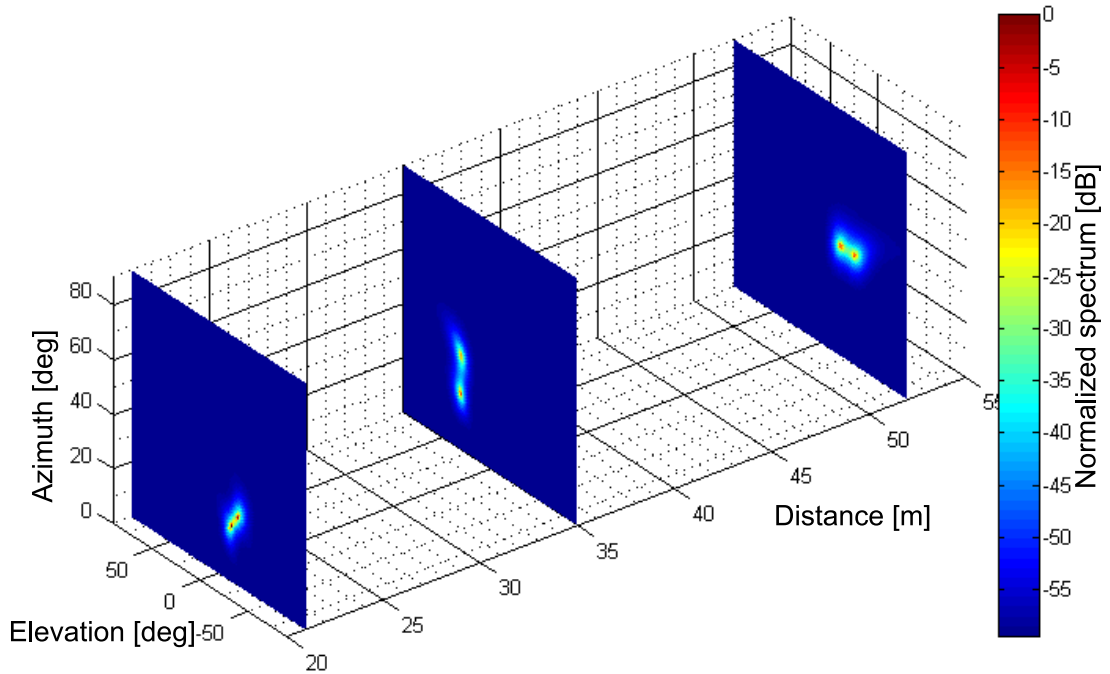


Fig. 4.8.: Volumetric representation

Fig. 4.9, 4.10, 4.11 show the separate detected radar images at the distance 20 m, 35 m and 50 m respectively. Fig. 4.10 shows a separability of objects at the same distance and elevation but with a difference of azimuth angles. The two objects at distance 35 m are fully separable with 14° . Fig. 4.11 shows a separability of objects at the same distance and azimuth but with a difference of elevation angles. The two objects at distance 50 m are fully separable with 14° .

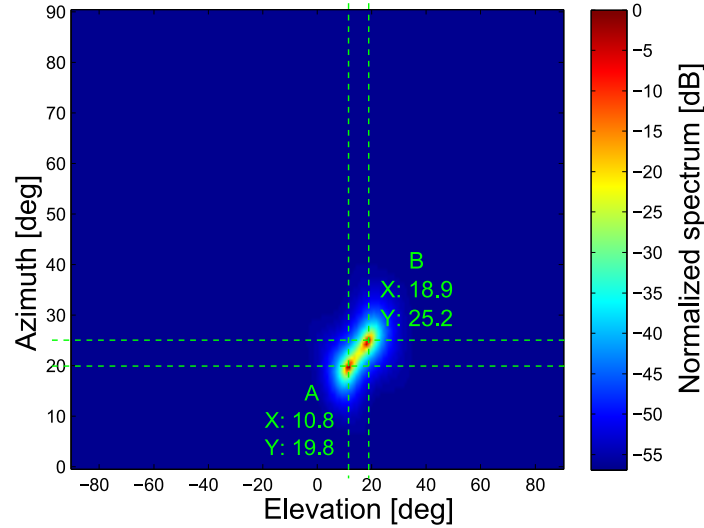


Fig. 4.9.: Radar image for objects at distance $d = 20$ m

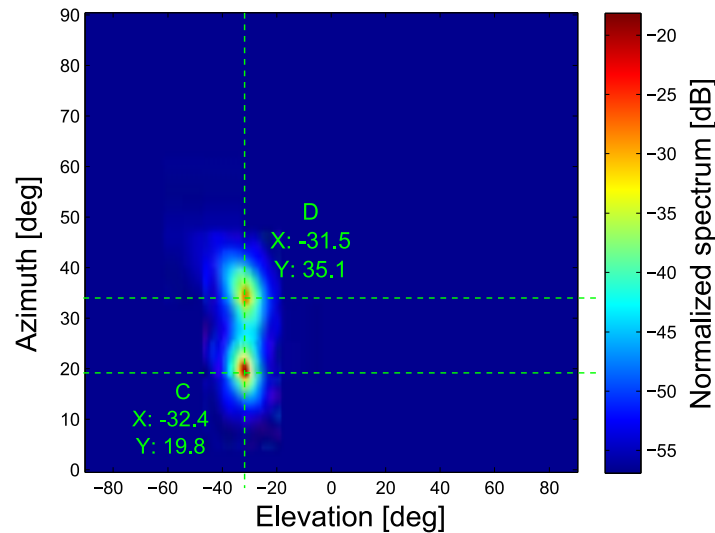
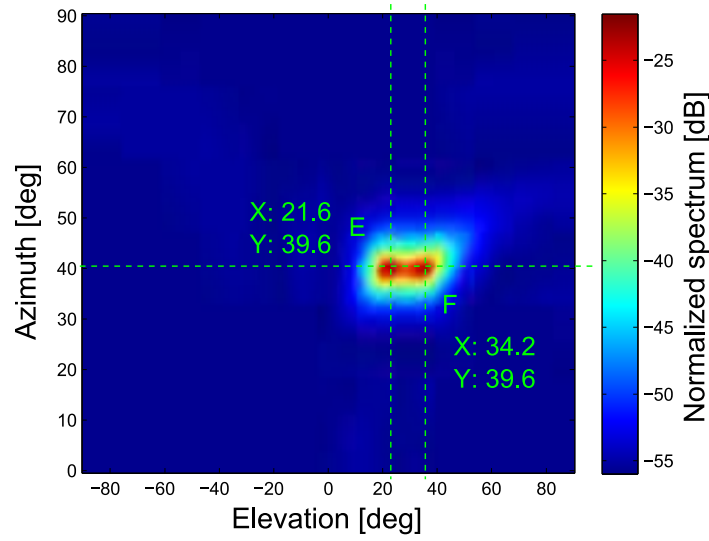


Fig. 4.10.: Radar image for objects at distance $d = 35$ m

Fig. 4.11.: Radar image for objects at distance $d = 50$ m

Effect of Antenna Geometry on the Radar Image

The number of antennas is changed to $4 \text{ Tx} \times 4 \text{ Rx}$ in order to compare the angular resolution of the $4 \text{ Tx} \times 4 \text{ Rx}$ with the one of $8 \text{ Tx} \times 8 \text{ Rx}$ system. The scenario is the same as mentioned at the beginning of this section with 6 objects considered as point scatterers, $\text{SNR} = 5$ dB. Fig. 4.14 depicts the superimposed radar image of objects. It can be seen that all 6 objects are detected. However, compared to the $8 \text{ Tx} \times 8 \text{ Rx}$ configuration in Fig. 4.12(b), the resolution in the $4 \text{ Tx} \times 4 \text{ Rx}$ configuration is not as good. The two objects C and D are not clearly separated.

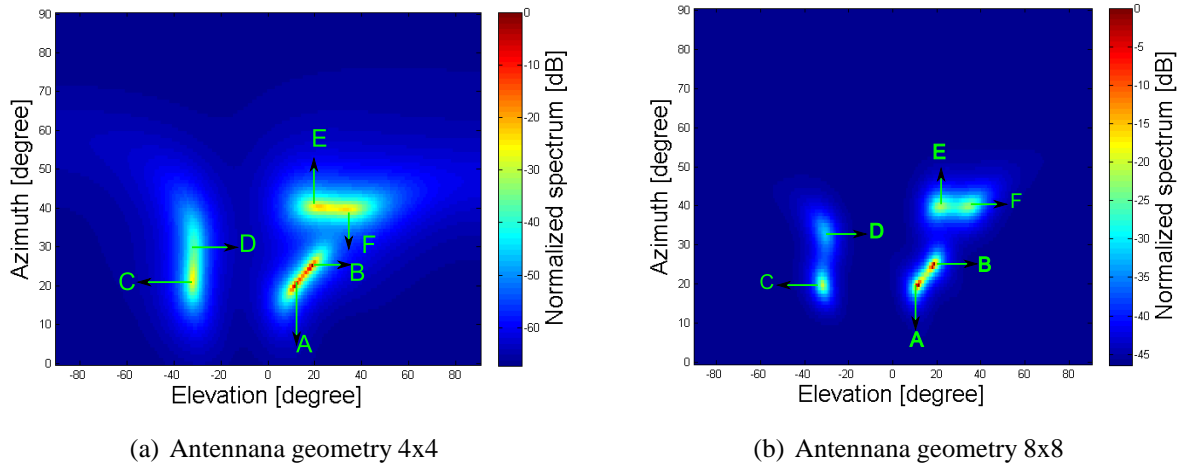


Fig. 4.12.: Comparison of number of antenna elements

The two-dimensional spatial spectra at distance 35 m are shown in Fig. 4.13. These spectra illustrate the positions of objects C and D. In the case of a $4 \text{ Tx} \times 4 \text{ Rx}$ MIMO system, the angular resolution

is lower than that of a $8 \text{ Tx} \times 8 \text{ Rx}$. The spectra of antenna geometry $8 \text{ Tx} \times 8 \text{ Rx}$ configuration shows two sharp peaks. The peak of object C is 20 dB higher than the valley between two peaks while the peak of object D is 10 dB higher although of the same RCS. This is due to the step of the steering vector and can be corrected by choosing a smaller step. In the $4 \text{ Tx} \times 4 \text{ Rx}$ case, the separation of those two peaks is not clear. Therefore, improving the number of elements in the receive and transmit antennas leads to a higher resolution in DOA estimation. However, it also makes the dimension of the radar system larger and the computation time is longer. Thus, depending on specific applications, the dimension should be taken into account.

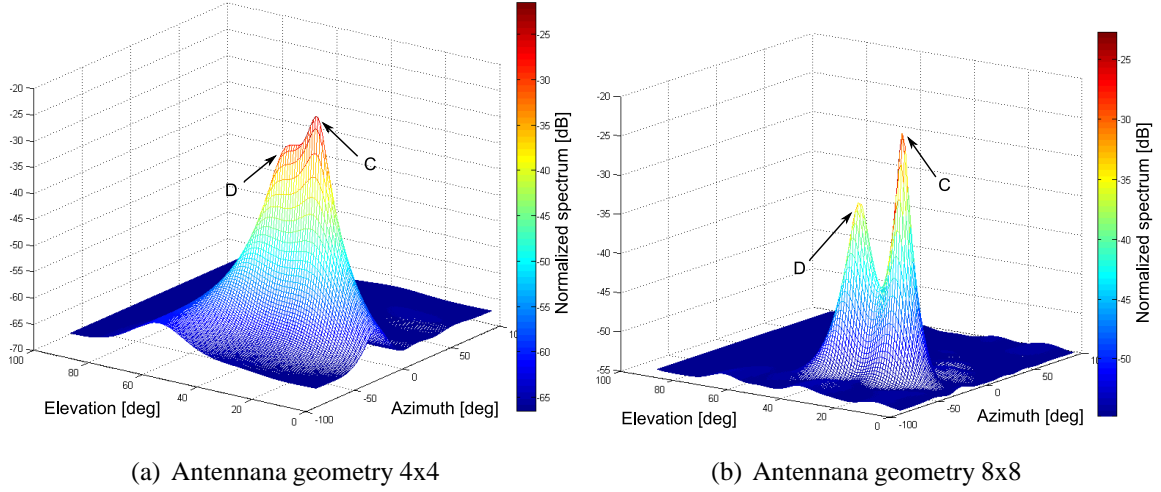


Fig. 4.13.: Comparison of number of antenna elements

Effect of SNR on the Radar Image

Fig. 4.14 shows the superimposed radar images of objects in the $8 \text{ Tx} \times 8 \text{ Rx}$ case for different SNRs. In Fig. 4.14(a) depicting the radar image for $\text{SNR} = -5 \text{ dB}$, there are only two clear objects A and B. Objects C, D, E and F are not separable. Contrary to that for $\text{SNR} = 5 \text{ dB}$ shown in Fig. 4.14(b), the separability of all objects are clear. Therefore, the higher the SNR is, the sharper the peaks becomes. The presence of noise causes a spreading effect on the peaks.

In addition for different SNRs, MUSIC algorithm requires *a priori* knowledge of the background noise and interference field. Objects are only detected correctly with the right setting of the threshold to estimate the eigenvalues which belong to the noise subspace as discussed in section 4.1.

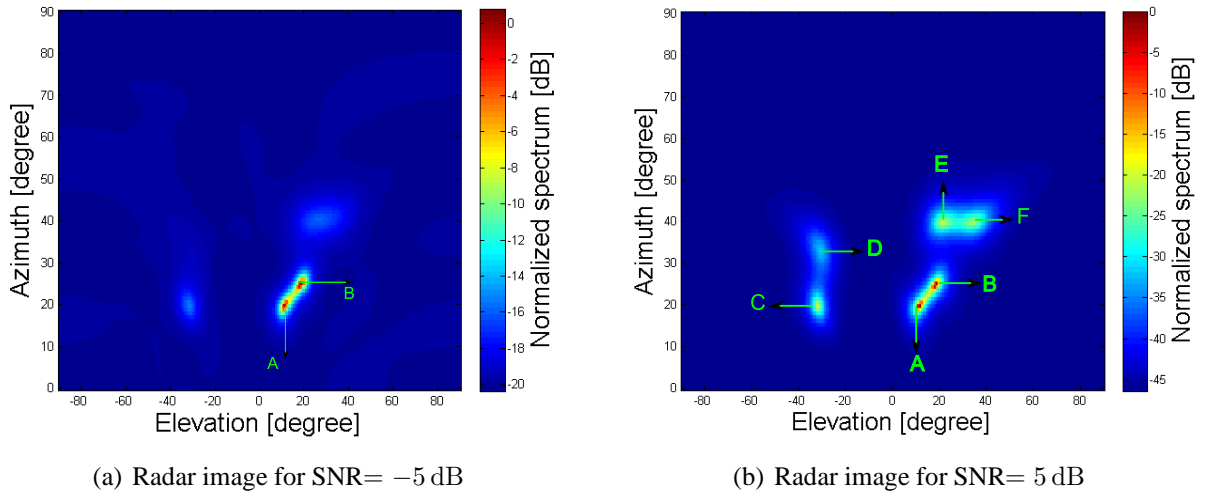


Fig. 4.14.: MUSIC performance in different SNR scenarios

4.3.3. Conclusion of MUSIC Algorithm's Performace

The MUSIC algorithm is a common one since it is applicable to estimate multiple parameters per source for arbitrary arrays with known configuration. In this case, can estimate both azimuth and elevation angle.

The performance of the MUSIC algorithm for 2D and 3D radar is good for an $\text{SNR} \geq -10$ dB. The separation of objects in both azimuth and elevation angle are 5° separable in 2D radar and 14° separable in 3D radar. Its performance is also influenced by a number of parameters such as the SNR, the number of antenna elements, the antenna geometry of receive and transmit antennas. However, the noise statistics must be measured or characterized analytically in order to set the sufficient threshold to detect objects.

In the Matlab simulation, the steering vector resolution of 0.01 rad (0.57°) is not perfect. However, it's chosen since it gives enough resolution and the computing time is short. If the step increases, the angular resolution also increase but the computing time increases.

5. Realization of the RF Frontend

In this chapter, the hardware design of the OFDM-based MIMO radar is presented. First, the direct conversion radio architecture will be discussed. Then, each part of the RF front end, including the digital-to-analog converters (DACs), low pass filters (LPFs), Inphase/Quadrature (I/Q) modulators, PLL frequency synthesizer and Wilkinson divider, will be presented.

5.1. Design Considerations

As mentioned in chapter 1, the final goal of the MIMO Radar project is to build a functionally complete system, consisting of several processing parts such as the signal processing unit, radar processing unit, RF front-end with antennas. The block diagram of the OFDM-based MIMO radar is shown in Fig. 5.1.

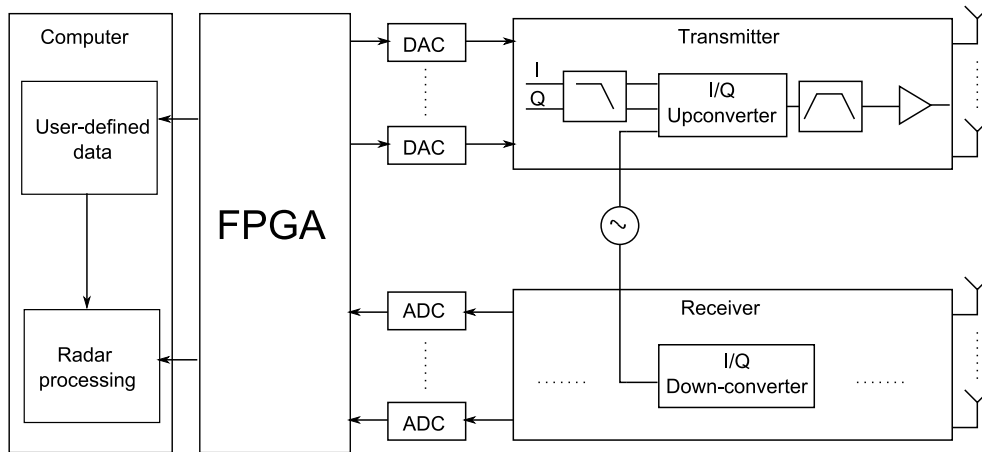


Fig. 5.1.: Block diagram of the OFDM-based MIMO Radar

An FPGA-based platform, performing a part of the baseband signal processing in hardware has been designed in [2]. The FPGA has the capability to generate the digital I/Q signals from the data defined by the user for other stages in transmitters and to demodulate the received signals afterwards for further processing. The implementation has been done on the FPGA for transmitters, but not for the receivers. Since there is still a continuing work of the FPGA for the receivers, only the RF front end for transmitters are considered in this thesis. The measurement setup is thus changed to utilize the Signal Analyzer in place of the receiver as shown in Fig. 5.2. This measurement setup is made to verify the transmitted signals from the FPGA and digital-to-analog converters (DAC), and to test the MIMO radar functionality along with the DOA algorithms. A reference clock from the

FPGA is split to the transmitters and the signal analyzer to prevent frequency offsets, which can lead to the loss of orthogonality in the OFDM signals.

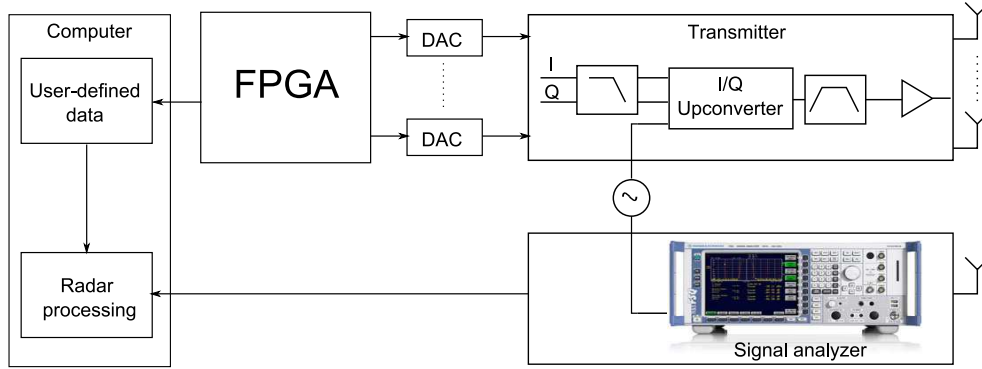


Fig. 5.2.: Measurement setup

In this project, a direct conversion RF frontend is considered. Direct conversion means that the baseband signal is directly converted to the RF signal without any intermediate frequency (IF) stage. Direct conversion eliminates the need of an intermediate IF stage and an associated filtering process, thus reducing the transceiver's complexity, size and cost [7].

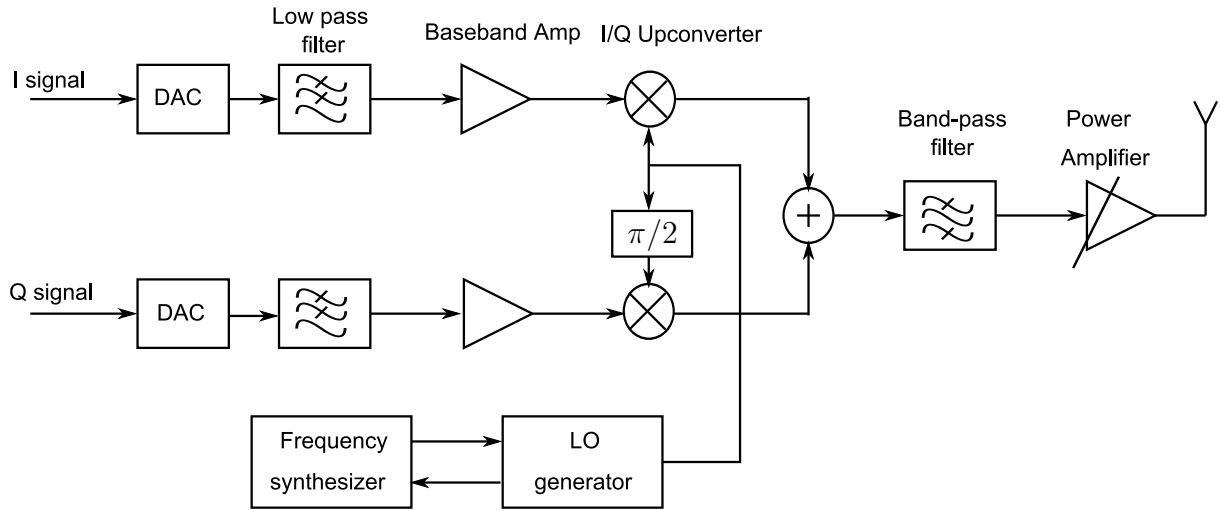


Fig. 5.3.: Block diagram of the direct-conversion transmitter

The I and Q digital baseband signals generated by the FPGA first pass through the DAC. After that, low pass filters are needed to suppress the images due to the sampling rate. The I and Q signals may require baseband amplifiers in the case when the output power of the baseband signals are too low. The filtered and amplitude-amplified signals are then directly up-converted to RF signals, then added together in the I/Q upconverter. An RF bandpass filter is needed to suppress noise and spurs emissions. Towards the end of the transmitter block, the signals are amplified by the RF power amplifier.

In the next sections, each parts of the transmitter will be discussed. The MIMO radar consists of 4 transmitters and operate at 24.15 GHz to suit the frequency regulation (ISM band) in Germany.

5.2. Digital to Analog Converter (DAC)

A DAC is a device which converts a digital signal to an analog waveform. Fig. 5.4 represents the operation of the DAC with a 6-bit resolution in the time and frequency domains, where every 6 bits of the bit stream from the FPGA is applied to the inputs of the DAC and then converted to analog signal at the sampling frequency f_s . In the frequency domain these signals are replicated at multiples of f_s and the amplitude is determined by the $\sin x/x$ function due to the frequency response of the hold function in the DAC. The hold function is a rectangular function in time domain, therefore in the frequency domain it is translated into a *sinc* function. The denominator x also leads to a decrease in amplitude of the output signals. As shown in Fig. 5.4, the multiples of the Nyquist frequency $f_s/2$ determines the Nyquist zones (zone 1, 2, 3...). The multiplication of the signal and the hold function of the DAC in the frequency domain leads to the images in the Nyquist zone.

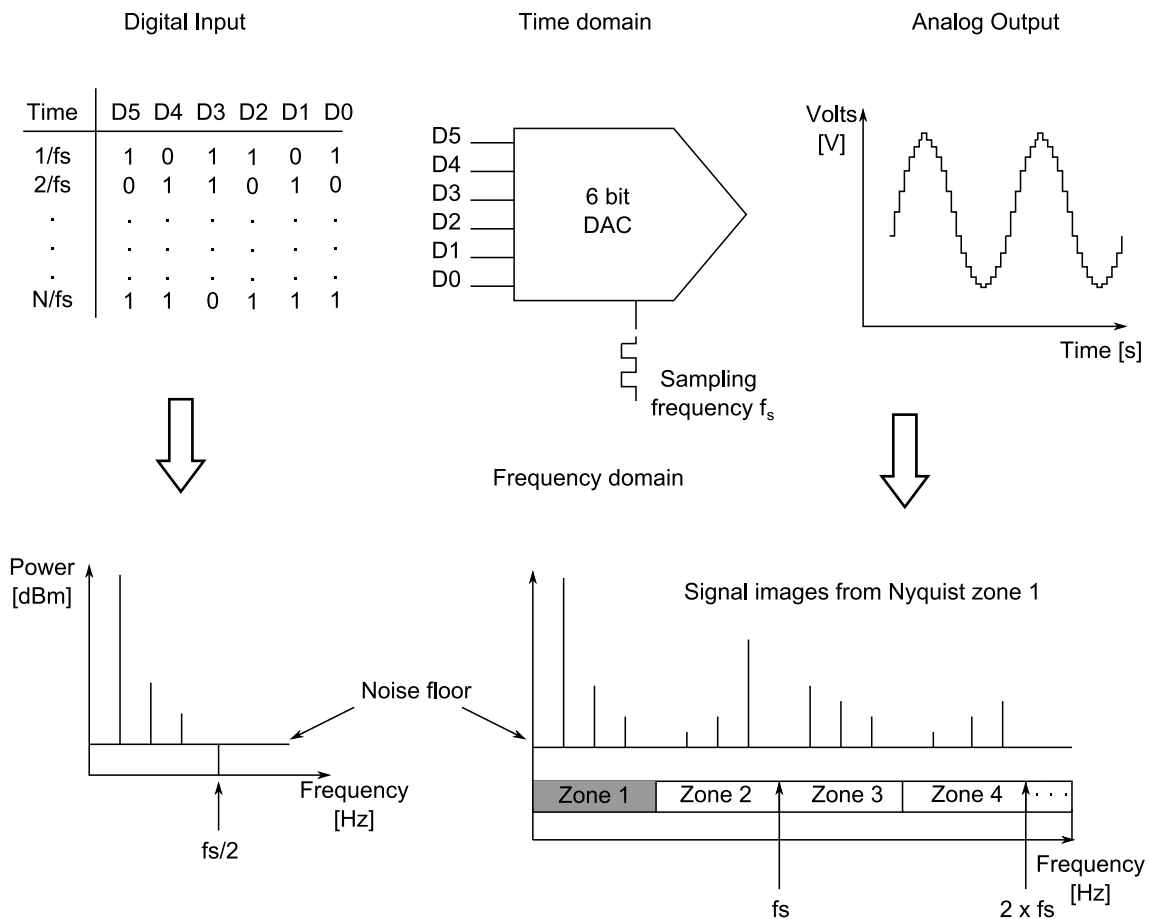


Fig. 5.4.: Basic diagram of a 6-bit DAC in time and frequency domain

The most important characteristics of DACs are:

- **Resolution:** This is the number of possible output levels of the DAC and is equal to 2^n , where n is the number of output bits. In the diagram, a 6-bit DAC is equivalent to $2^6 = 64$ levels.
- **Maximum sampling rate:** This is the maximum speed that the DAC can operate at to produce correct analog signals. The choice of DACs depends on the relationship between the bandwidth of the sampled signal and the sampling rate, which is based on Nyquist-Shannon sampling theorem.

In this project, the DAC2904 evaluation modules from Texas Instruments (TI) are used. Each module has the update rate f_{CLOCK} up to 125 MSPS (MSPS = mega samples per second) and 14-bit resolution. The detailed specifications of this module can be found in [29]. Since the baseband bandwidth of the OFDM signals is less than 100 MHz and oversampling was not performed in the FPGA, the clock frequency f_{CLOCK} is set to be 100 MSPS. The DAC2904 modules are sufficient for the current requirement. However, since the signal of interest occupies almost the entire bandwidth up to $f_s/2$, the requirements for a steep roll-off LPF with cutoff frequency ω_c after each DAC to suppress the images in other Nyquist zones are critical.

5.3. Low Pass Filter

As explained in section 5.2, LPFs are required to suppress the images after the DAC processing. Filters are classified according to the functions they performs, in term of ranges of frequencies. A low-pass filter characteristic is one in which the pass band extends from $\omega = 0$ to $\omega = \omega_c$, where ω_c is the cutoff frequency. There are several forms of lowpass response. However, to meet the requirement that there is no ripple in the passband, we limit our choices to the Butterworth or the Inverse Chebyshev filters. In addition, since the transition band must be very narrow, a high order filter is required to achieve a steep roll-off. Preliminary calculations of the filter order to fulfill the conditions mentioned show that the Butterworth filter requires more elements than Inverse Chebyshev filter. Since the ripple in the stop band is not important, the inverse Chebyshev filter is thus decided upon. Since the LPF has the cut-off frequency at 50 MHz, a lumped element filter is chosen. A microstrip filter is not suitable here because the operating frequency is low, leading to a very large physical size.

The lowpass Chebyshev response can be expressed as follows [30]

$$|T_c(j\omega)|^2 = \frac{1}{1 + \epsilon^2 C_n^2(\omega)} \quad (5.1)$$

where $|T_c(j\omega)|$ is the magnitude response or gain characteristics of the filter, C_n is the Chebyshev polynomials of order n . Subtracting (5.1) from 1, we have

$$1 - |T_c(j\omega)|^2 = \frac{\epsilon^2 C_n^2(\omega)}{1 + \epsilon^2 C_n^2(\omega)} \quad (5.2)$$

Finally, by inverting frequency by replacing ω with $1/\omega$, we have the inverse Chebyshev response

$$\begin{aligned} |T_I C(j\omega)|^2 &= \frac{\epsilon^2 C_n^2(1/\omega)}{1 + \epsilon^2 C_n^2(1/\omega)} \\ &= \frac{1}{1 + 1/\epsilon^2 C_n^2(1/\omega)} \end{aligned} \quad (5.3)$$

The attenuation factor can be expressed as

$$\alpha = 10 \log \left[1 + \frac{1}{\epsilon^2 C_n^2(1/\omega)} \right] \text{ dB} \quad (5.4)$$

A Matlab simulation code has been written to calculate the order of the filter. Fig. 5.5 represents all the parameters which are taken into account when designing the LPF. The 3 dB frequency ω_p is 48 MHz, the stopband or cutoff frequency ω_s is 50 MHz, the passband ripple R_p , which shows the maximum passband loss in decibels, is 3 dB and the stopband attenuation R_s , which is the number of dB the stopband is down from the passband, is 30 dB.

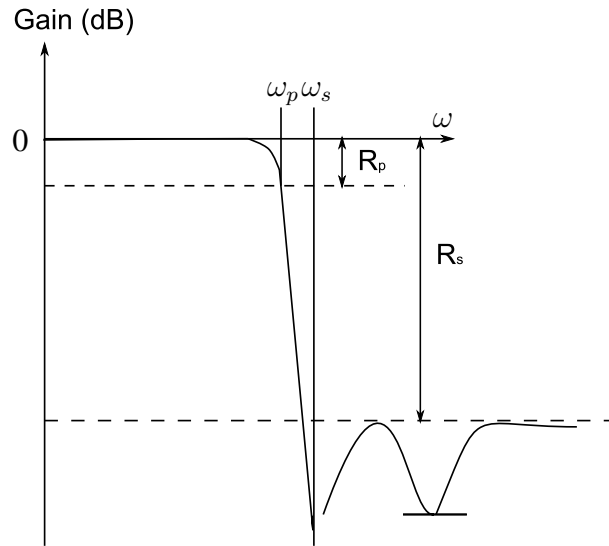


Fig. 5.5.: Frequency response of an inverse Chebyshev filter

The order of the LPF is estimated to be 12 to achieve a steep roll-off. After that, we simulated the magnitude response of the LPF and generated the schematic in ADS Agilent. The parameters of all the lumped elements have been adjusted to fit with the value of those available on the market. Fig. 5.6 shows the schematic of LPF. The printed circuit board (PCB) was designed by using the EAGLE software.

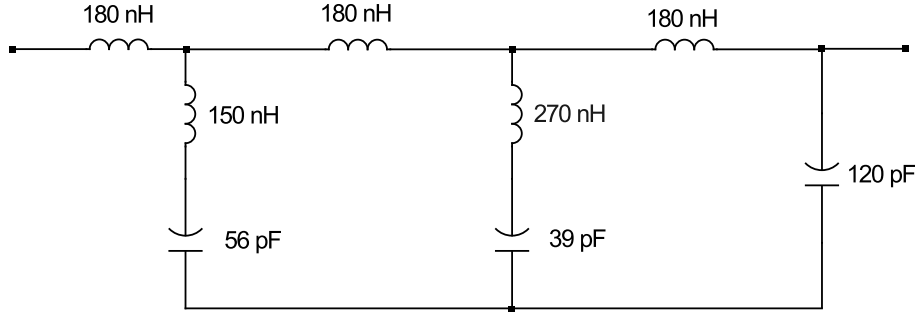


Fig. 5.6.: Schematic of Low pass filter

The designed filters are fabricated on the FR-4 substrate (ϵ_r , conductor thickness=, substrate thickness=). Fig. 5.7 and Fig. 5.8 depict the transfer function and reflection coefficient from the simulation result using Agilent ADS and the measured data from the Network analyzer. The measured S21 result is slightly different from the simulated results due to the non-ideal lumped components otherwise the filter characteristics for the simulated and measured results matches very closely. Since the FPGA can perform carrier suppression to adjust the bandwidth, the designed LPF are sufficient for the current usage.

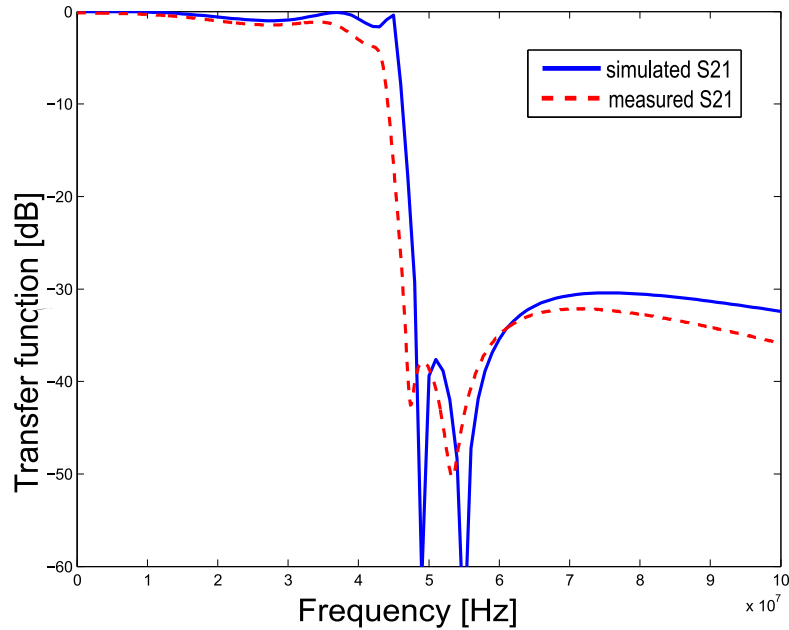


Fig. 5.7.: Transfer function of the low-pass filter

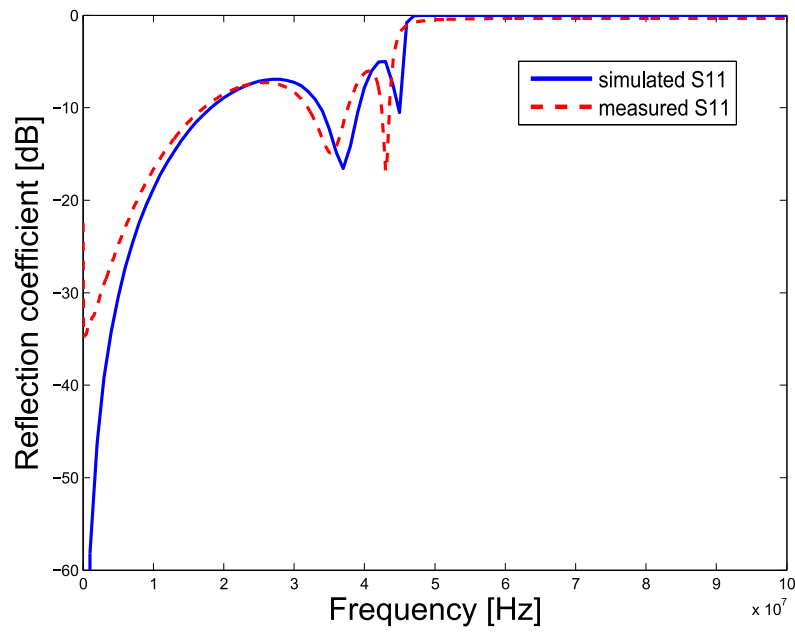


Fig. 5.8.: Reflection coefficient of low-pass filter

The fabricated lowpass filter is shown in Fig. 5.9. The size of the filter board is about $4\text{ cm} \times 1.5\text{ cm}$ and the board is connected to the SMA connectors at both ports. The filter is reciprocal at both ports.

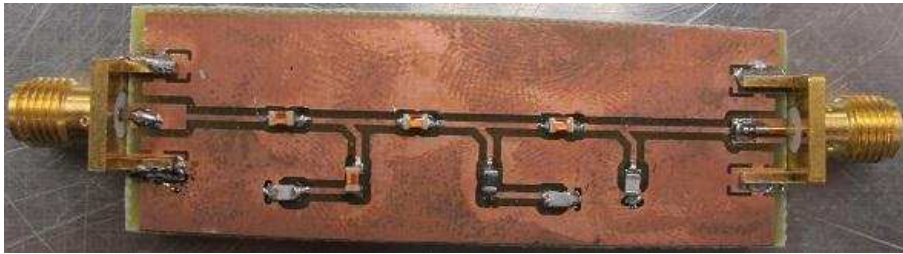


Fig. 5.9.: The fabricated low-pass filter

5.4. PLL Synthesizer

A Phase-locked Loop (PLL) synthesizer is the electronics system to generate multiple signal frequencies from a common reference, such as a crystal oscillator. In this work, a frequency synthesizer is required to generate the local oscillator signals for the I/Q upconverters. The signals after the frequency synthesizer are split into each of 4 I/Q upconverters by a 4:1 Wilkinson divider. Figure 5.10 shows a typical block diagram of a PLL implementation with a master oscillator reference.

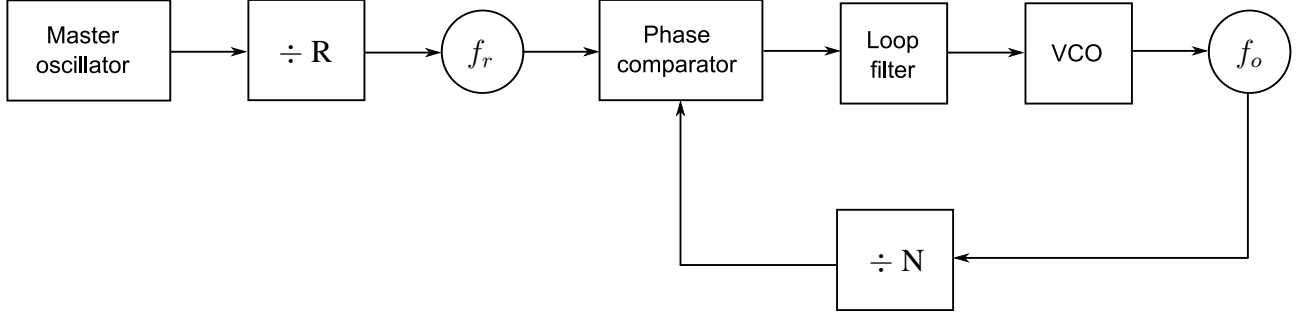


Fig. 5.10.: Block diagram of classical PLL

The PLL circuit performs the frequency multiplication via a negative feedback loop to generate the output frequency, f_0 , in terms of the phase detector comparison frequency, f_r [28].

$$f_{VCO} = N \cdot f_r \quad (5.5)$$

A reference frequency must be provided to the phase detector. Typically, the TCXO frequency, f_x , is divided by R on the PLL chip. The phase detector uses this signal as a reference to tune the VCO and in a "locked state" it is equal to the desired output frequency, f_0 , divided by N .

$$f_0/N = f_x/N = f_r \quad (5.6)$$

Therefore, the output frequency generated by the PLL frequency synthesizer can be changed by changing the divider N to a new value. Consequently, the VCO can be tuned to the frequency of interest. When the PLL is in the unlocked state, the phase detector creates a error voltage based on the phase difference of the two input signals. The error voltage will change the frequency of the VCO so that it satisfies (5.6).

In this work, a HMC783LP6CE PLL with integrated VCO evaluation board is used. The typical setup of the evaluation board is depicted in Fig. 5.11. The evaluation board can be configured with an on-board crystal oscillator or with an external source. The operating frequency is 11.5 – 12.5 GHz. Since there is a frequency multiplier by 2 in the I/Q upconverter, the local oscillator signal needs to be half the value of the carrier frequency $f_c/2 = 12.075$ GHz.

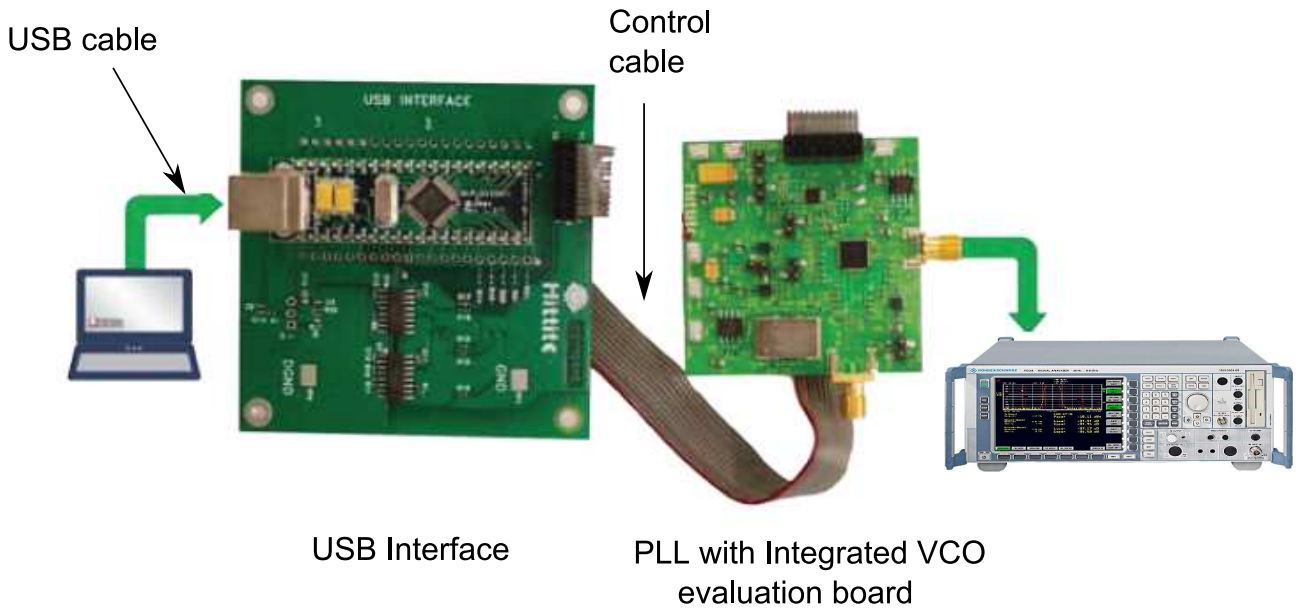


Fig. 5.11.: Setup of Hittite PLL with integrated VCO

A measurement has been conducted to measure the phase noise and spurious signals from the local oscillator, which may distort the desired signal. The output frequency is set to be at $f_c/2 = 12.075$ GHz. The signal is measured by *FSQ26* signal analyzer. Fig. 5.12 depicts the output signals from the PLL synthesizer. Table 5.1 lists all the outputs in the frequency range of 0 – 26.5 GHz. Since the prescaler frequency f_r is $f_r = 6037.5$ MHz, the spurs are actually the harmonics at f_r and appear in the output signals due to the leakage in the VCO. From the measured data, since the spurs generated by the PLL synthesizer have low output power, their interference to the band of interest is negligible.

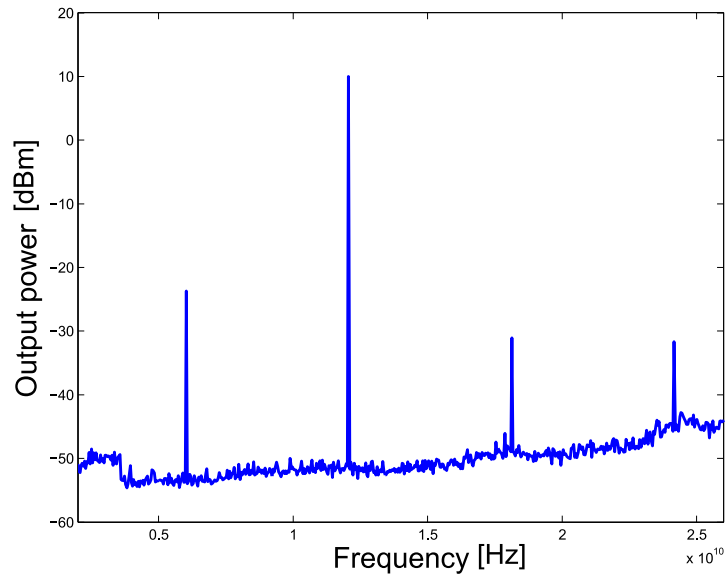


Fig. 5.12.: A full span of the frequency spectrum

Frequency [GHz]	Output power [dBm]
6.03	-24
12.075	10
18.813	-31
24.16	-32

Table 5.1.: The signals from the local oscillator

Fig. 5.13 depicts a close up look of the local oscillator signal in the frequency domain. The output spectrum cannot be modeled by a Dirac delta function at the center frequency f_c but by a broader pulse. Actually, this is a delta function surrounded by phase noise, which is caused by the rapid and random fluctuations in the phase of the waveform. Since phase noise can lead to serious problem in OFDM system, its measurement has also been conducted. The detailed studies for the phase noise can be found in [15]. In practice, phase noise is expressed as the ratio of the 'power spectrum density at a specific offset frequency' to the 'carrier signal level'. The phase noise measurement is a very sensitive one. However, in this thesis, it is simply made by *FSQ26* signal analyzer through the averaging method. The center frequency has been set to be 12.075 GHz and the offset frequency is 10 kHz. The measured phase noise for 10 kHz is -76.7 dBc/Hz. This PLL frequency synthesizer can be considered as a low phase noise device. Since this is not in the scope of this thesis, the effect of phase noise will not be investigated further.

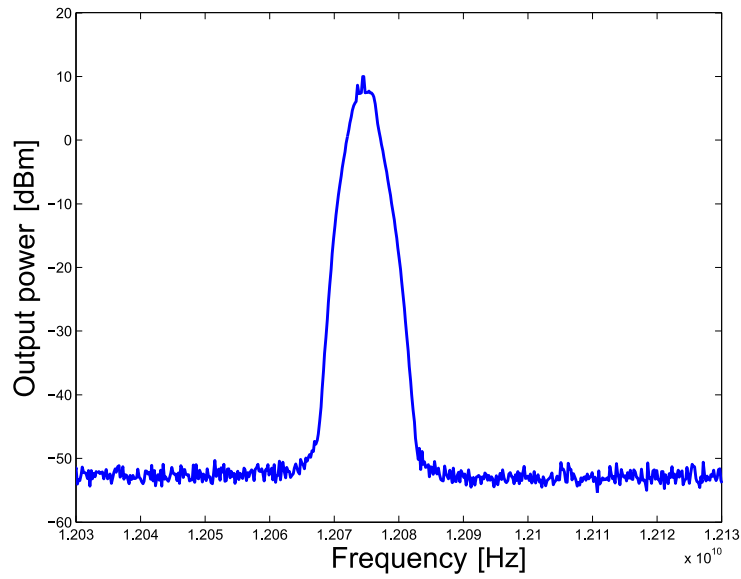


Fig. 5.13.: A close up look to the local oscillator signal

5.5. Wilkinson Power Divider design

As discussed in 5.1, a microstrip 4:1 equal Wilkinson power divider is needed to feed the signal from the local oscillator to I/Q upconverter. In this section, the theory and design of Wilkinson divider will be discussed.

5.5.1. Transmission Line Circuit

In its simplest form, the two-way split Wilkinson power divider is a three-port network shown in Fig. 5.14. It splits an input signal into two in-phase signals with the same amplitude. For a two-way Wilkinson divider using $\frac{1}{4}$ impedance transformers having a characteristic impedance of $\sqrt{2}Z_0$ and a lumped isolation resistor of $2Z_0$ with all three ports matched, high isolation between the output ports can be obtained [31]. The resistor allows all three ports to be matched, as well as fully isolating port 2 from port 3 at the center frequency. The design of an equal-split (3 dB) Wilkinson is often made with microstrip or stripline.

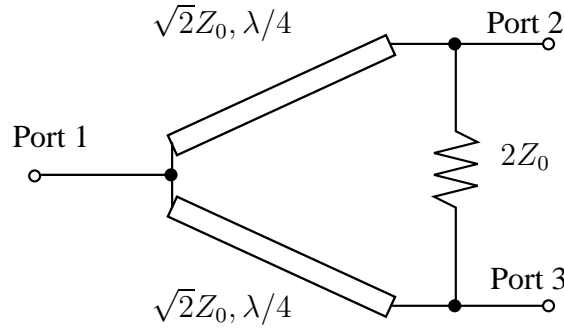


Fig. 5.14.: Ideal two-port Wilkinson power divider

In this work, the design of Wilkinson divider are made with microstrip since it can be fabricated simply by photolithographic process and can be easily integrated with other microwave devices. The design for center frequency of 12.075 GHz and $Z_0 = 50 \Omega$ requires the isolation to be $2Z_0 = 100 \Omega$ and the impedance of the $\lambda/4$ transmission line split section to be $\sqrt{2}Z_0 = 70.71 \Omega$. A Rogers4003 substrate was chosen because of its stable electrical properties and dielectric constant, ϵ_r , at high frequency. The specification of the substrate is as listed in the Table 5.2.

In the next step, the method to calculate the geometry of Wilkinson divider will be discussed.

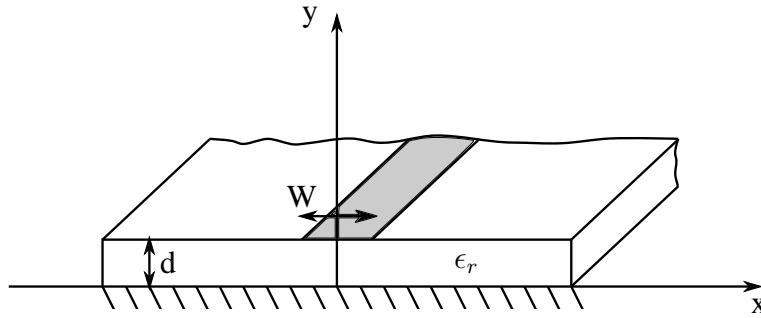


Fig. 5.15.: Geometry of the microstrip transmission line

The geometry of a microstrip line is shown in Fig. 5.15. The phase velocity of the signal traveling in the microstrip line can be expressed as

$$v_p = \frac{c}{\sqrt{\epsilon_e}} \quad (5.7)$$

where:

ϵ_e is the effective dielectric constant of the microstrip line

c is the light velocity in free space.

Given the characteristic impedance of a microstrip line, the thickness and the dielectric constant of the substrate, the width of the microstrip line can be approximated using the equations developed in [13].

For $\frac{W}{d} < 2$

$$\frac{W}{d} = \frac{8e^A}{e^{2A} - 2} \quad (5.8)$$

$$A = \frac{Z_0}{60} \sqrt{\frac{\epsilon_e + 1}{2}} + \frac{\epsilon_e - 1}{\epsilon_e + 1} \left(0.23 + \frac{0.11}{\epsilon_e} \right)$$

For $\frac{W}{d} \geq 2$

$$\frac{W}{d} = \frac{2}{\pi} \left[B - 1 - \ln(2B - 1) + \frac{\epsilon_e - 1}{\epsilon_e} \left(\ln(B - 1) + 0.39 - \frac{0.61}{\epsilon_e} \right) \right] \quad (5.9)$$

$$B = \frac{377\pi}{2Z_0\sqrt{\epsilon_e}}$$

where:

Z_0 is the characteristic impedance

ϵ_e is the dielectric constant of the substrate

W is the width of the microstrip line

d is the thickness of the substrate.

After that, substituting W into equation (5.10) to find the effective dielectric constant of the microstrip line.

$$\epsilon_e = \frac{\epsilon_e + 1}{2} + \frac{\epsilon_e - 1}{2} \frac{1}{\sqrt{1 + 12d/W}} \quad (5.10)$$

The length l of the microstrip line depends on the phase shift, ϕ , and is found as

$$\phi = \beta l = \sqrt{\epsilon_e} k_0 l \quad (5.11)$$

where:

$k_0 = 2\pi f/c$ is the wavenumber

5.5.2. 4:1 Wilkinson Power Divider Simulation Results

Applying the theory discussed in 5.5.1, a simulated circuit for the 4:1 Wilkinson power divider is designed in ADS Agilent. Fig. 5.16 shows the model of the 4:1 Wilkinson divider using microstrip curve segments to model the circular quarter-lambda split section. The ADS model is matched to 50Ω at all ports. The microstrip transmission line segments use microstrip T-junctions, straight transmission lines, curve components. The substrate characteristics for Roger 4003C with thickness 0.508 mm were included in the model as well. The parameters of the substrate used in simulation and fabrication are as listed in Table 5.2. The only difference between the specification parameters and circuit simulation is the value of the dielectric constant of the substrate. This difference has

been specified in the substrate data sheet for use in simulations to account for the losses in the actual fabricated circuit.

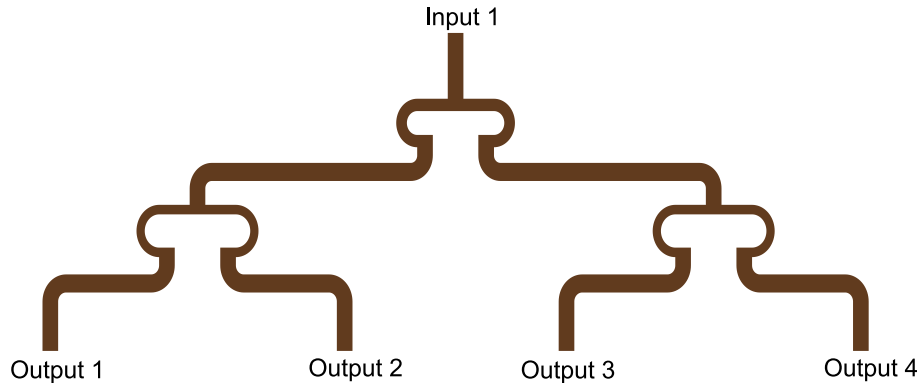


Fig. 5.16.: ADS transmission line model of 4:1 Wilkinson divider

Parameter	Substrate specification	Circuit simulation
Dielectric constant, ϵ_r	3.38 ± 0.05	3.55
Dissipation factor, $\tan\sigma$	0.027	0.027
Substrate thickness, h	0.508 mm	0.508 mm
Conductor thickness, T	17 μm	17 μm
Conductivity	$5.8 \times 10^7 \text{ S}$	$5.8 \times 10^7 \text{ S}$

Table 5.2.: Roger4003C substrate specification

The fabricated circuit is shown in Fig. 5.17. The circuit was measured with a Rohde & Schwarz network analyzer for one output port using 50Ω terminations at the other output ports. The losses in the cable connecting the 4:1 divider and the network analyzer were also calibrated and taken into account.

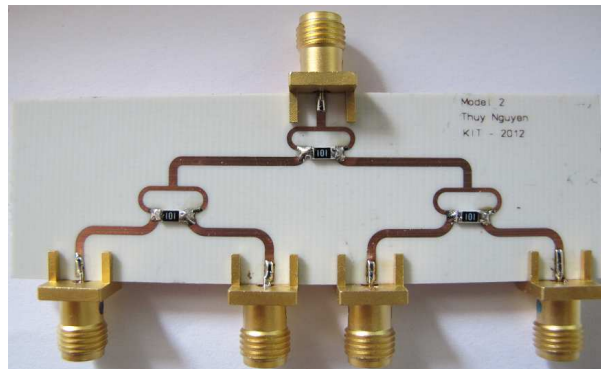


Fig. 5.17.: Fabricated circuit of the 4:1 Wilkinson Power Divider

The simulated results using MOMENTUM ADS and the measured results of the fabricated circuit are shown in Fig. 5.18 and 5.19. As the Wilkinson divider circuit is reciprocal at the output ports

1, 2, 3 and 4, only the results of S_{11} and S_{21} of port 1 are shown. In Fig. 5.18, the measured and simulated return losses are represented by S_{11} are shown. The measured return loss has a shift of approximately 600 MHz in the resonance frequency from the simulated result. The cause of the shift is due to the nonlinear change of the dielectric constant of the substrate at high frequencies and the coupling between transmission line of the circuit which cannot be modeled correctly by ADS.

Fig. 5.19 shows the simulated and measured insertion loss. The insertion loss fluctuates over the measured frequency of 9 GHz to 15 GHz. The measured results have deviations from the simulated due to inaccurate etching, substrate errors, SMA connectors and soldering. There is a peak at 12 GHz in the measured data. Since the frequency of interest is 12.075 GHz, the fluctuation of the insertion loss is not critical. At 12.075 GHz, the insertion loss is -8.8 dB. As discussed in 5.4, since the LO signal power from the PLL synthesizer is around 10 dBm and the average input power of the LO signal to be fed into the I/Q upconverter is 3 dBm, a low phase noise power amplifier may be needed to amplify the LO signal before feeding the signals into the Wilkinson divider.

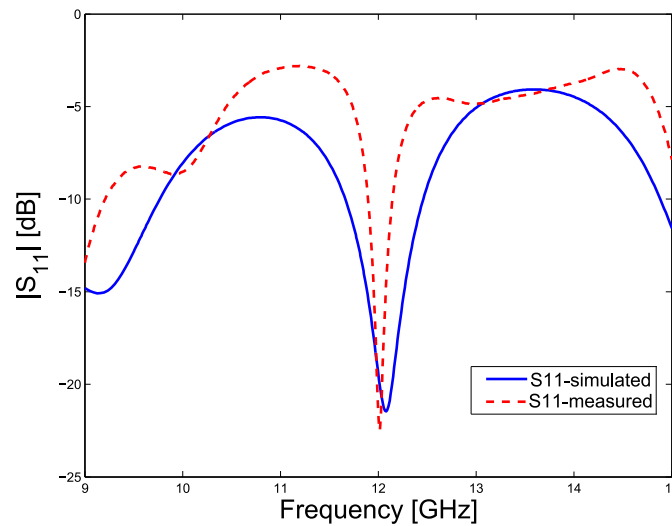


Fig. 5.18.: Simulated and measured results for return loss S_{11}

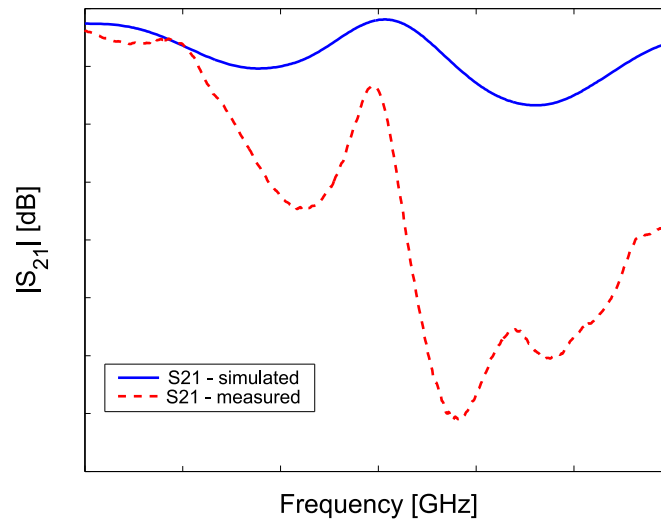


Fig. 5.19.: Simulated and measured results for insertion loss S_{21}

5.6. I/Q Modulator

Since the data is modulated using complex modulation techniques, there is a need of an In-phase/Quadrature (I/Q) modulator to directly upconvert the baseband I/Q data onto an RF carrier. A simple model of an I/Q modulator is shown in Fig. 5.20. At the top mixer, an LO signal $\sin(\omega_c t)$ and a baseband I signal $A\sin(\omega_{bb}t)$ are mixed. At the bottom mixer, a $\cos(\omega_c t)$ LO signal and a baseband Q signal $A\cos(\omega_{bb}t)$ are mixed.

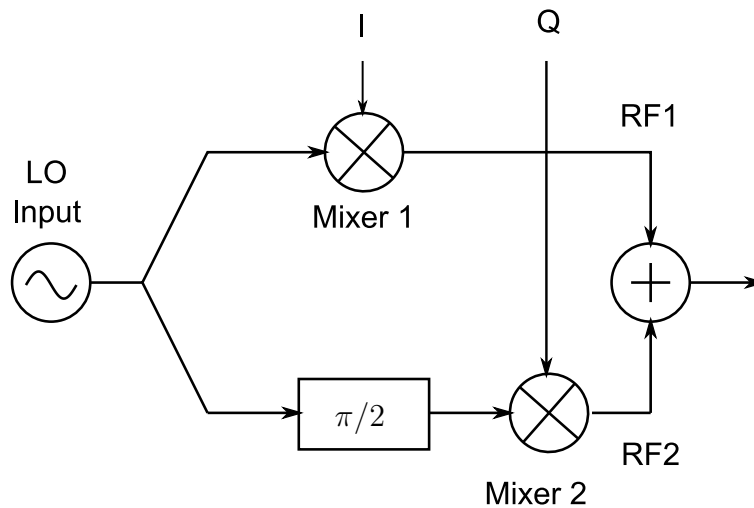


Fig. 5.20.: Basic I/Q Modulator Block Diagram

The output at RF1 includes two terms:

- the positive $\frac{1}{2}A\cos((\omega_c + \omega_{bb})t)$ for the upper sideband
- the negative $\frac{1}{2}A\cos((\omega_c - \omega_{bb})t)$ for the lower sideband.

The out put at the RF2 also includes two terms:

- the positive $\frac{1}{2}A\cos((\omega_c + \omega_{bb})t)$ for the upper sideband
- the positive $\frac{1}{2}A\cos((\omega_c - \omega_{bb})t)$ for the lower sideband.

The output of the two mixers are combined by a sum node, which leads to the results as follows

- The two upper sideband terms are in-phase and produce the desired output $A\cos((\omega_c + \omega_{bb})t)$.
- The two lower sideband terms are out of phase and cancel.

In this project, the HMC815LC5 I/Q upconverter eavaluation board from Hittite is chosen. The LO is driven by an active $\times 2$ frequency multiplier. Therefore, for the PLL synthesizer, the LO signal is just needed to be half of the value of the carrier frequency f_c . The specification of this product can be summarized in the table 5.3.

Parameter	Value
Operating frequency	21 – 27 GHz
Conversion gain	12 dB
Sideband rejection	–20 dBc
2 LO to RF isolation	10 dB
Output IP3	+27 dBm

Table 5.3.: Specification of HMC815LC5 I/Q Upconverter

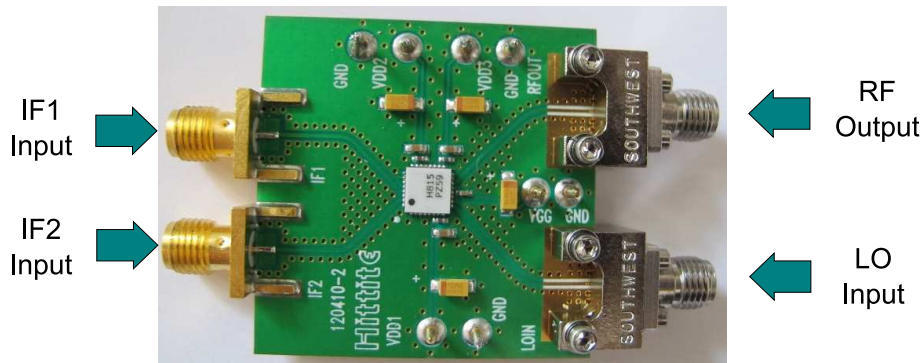


Fig. 5.21.: Circuit

The details of the I/Q upconverter will be discussed later in chapter 5.

5.7. Maximum Transmitted Power

For an automotive radar at the 24 GHz ISM band, the effective isotropic radiated power (EIRP) must not be greater than a value $EIRP \leq 20$ dBm at any point of a specific frequency. As

mentioned in 5.1, only the design of RF frontend for the transmitters is considered.

Consider the antenna gain for a typical patch antenna array is 15 dBi. We have

$$P_{EIRP} [\text{dBm}] = P_{Tx} [\text{dBm}] + G_{Tx} [\text{dB}] \leq 20 \text{ dBm} \quad (5.12)$$

where:

- P_{EIRP} is the effective isotropic radiated power of the system
- P_{Tx} is the transmitted power of each transmitter at a specific frequency
- G_{Tx} is the gain of the antenna

Thus, $P_{Tx} \leq 5 \text{ dBm}$ is needed to satisfy the frequency regulation.

The detailed calculation of the output power before the antenna will not be considered here since the output power of the baseband signal after the DAC is unclear. Note that, the cable loss in total is 3.5 dB, the insertion loss of the LPF is 0.7 dB and the conversion gain from the DAC is 12 dB. An attenuator will be needed if the output power is too high and a power amplifier will be needed if the output power is low.

6. Measurement Setup and Results

6.1. Measurement setup for one whole transmitter

In order to test the functionality of one transmitter, a baseband OFDM signal with $N_c = 1024$, $N_{sym} = 256$, $\Delta f = 90.909$ kHz and $T = 11 \mu s$ is generated in Matlab using random symbols with QPSK modulation. After that, it is converted to a waveform file (file extension *.wv) and then loaded to the *SMU200A* signal generator. The clock rate is set to be equal to the OFDM signal bandwidth $B = 93.1$ MHz. The output power of the generated signal is set to be -10 dBm. The measurement setup is shown in Fig. 6.1. A clock reference signal from the signal analyzer is fed to the PLL synthesizer and the *FSQ26* signal analyzer to synchronize the time base between them. The generated I and Q signal from signal generator will be uploaded to the RF front end and continuously repeated. The PLL synthesizer is controlled by a software through the USB interface module to generate a frequency at $f_c/2 = 12.075$ GHz.

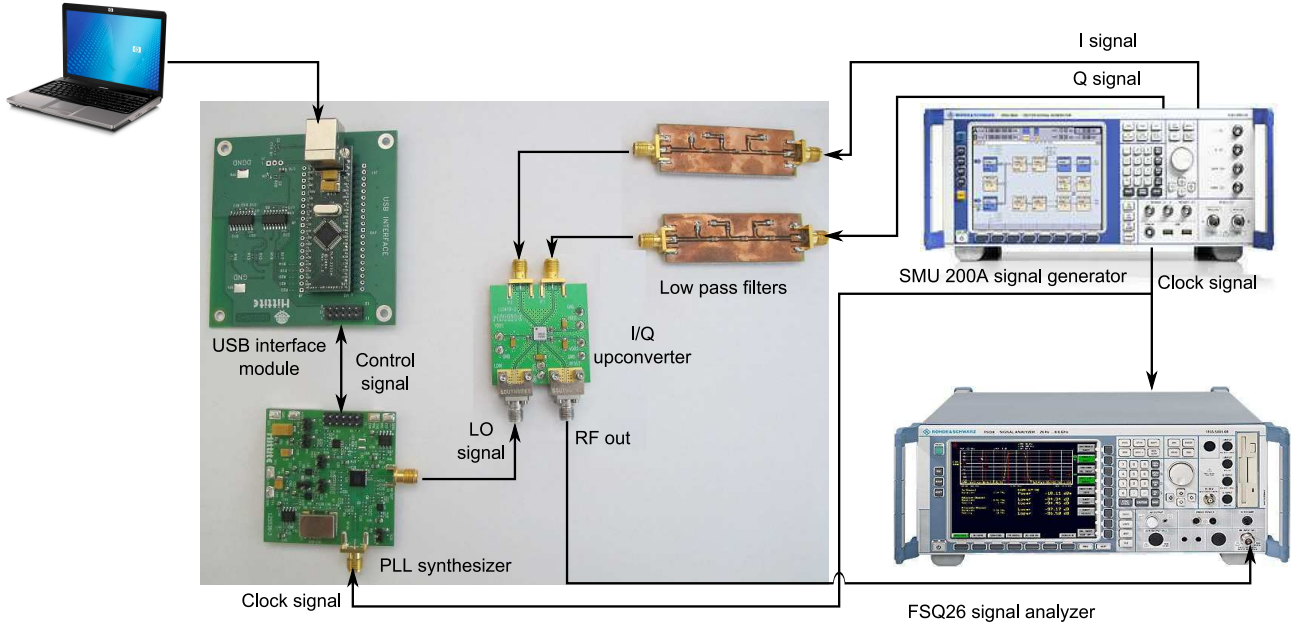


Fig. 6.1.: Measurement setup for on transmitter

Fig. 6.2 depicts the output signals from the I/Q upconverter in the signal analyzer. The frequency span is set to maximum from 10 kHz – 26.5 GHz. In this frequency range, there are three output signals as follows:

- The 1st signal at 24.15 GHz with output power -11 dBm, which is the signal of interest. Fig. 6.2 depicts the upconverted OFDM signal.
- The 2nd signal at 18.12 GHz with output power -52 dBm
- The 3rd signal at 12.07 GHz with output power -36 dBm

The frequency spacing between these signals is around 6.03 GHz, which is equal to the prescaler frequency f_r of the PLL synthesizer. Therefore, the 2nd and 3rd signals are actually generated from the intermodulation of the baseband OFDM signal with the unwanted harmonics from the PLL synthesizers. Fig. 6.4 and Fig. 6.5 show clearly that the bandwidth of the 2nd and 3rd signals are around 93.1 MHz. However, there are still peaks appearing in the spectrum. These peaks are the leakage of the LO signals to the RF output ports.

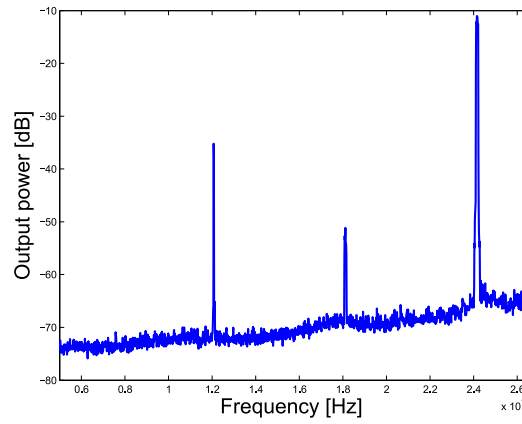


Fig. 6.2.: A full span of the output signal from the I/Q upconverter

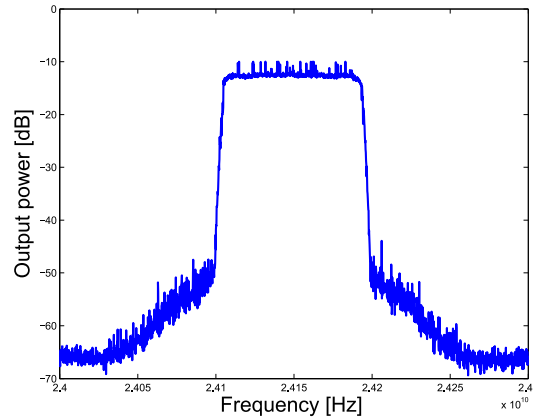


Fig. 6.3.: The signal of interest at 24 GHz, a close up of Fig. 6.2

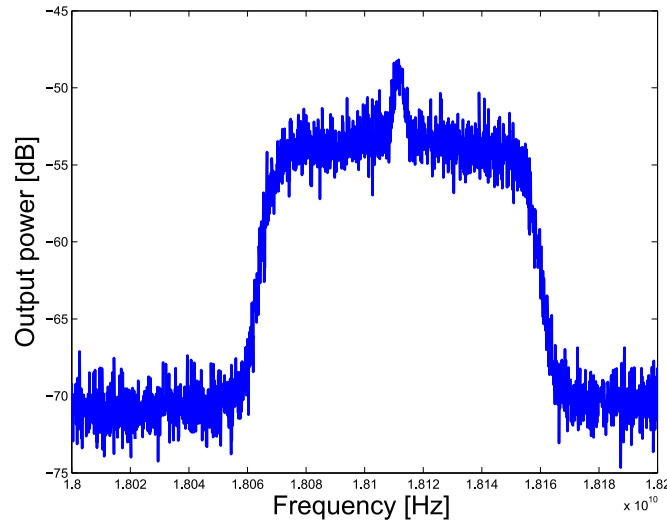


Fig. 6.4.: Unwanted intermodulation product at 18 GHz, a close up of Fig. 6.2

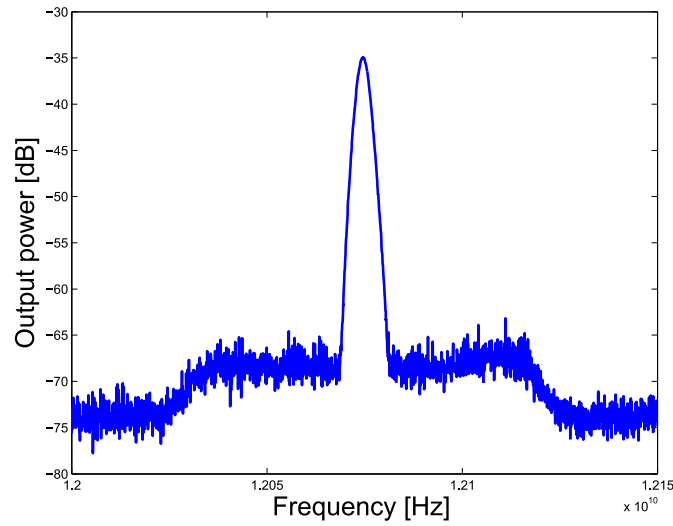


Fig. 6.5.: Unwanted intermodulation product at 12 GHz, a close up of Fig. 6.2

6.2. Analysis of the Signals from the FPGA

The prototype of the FPGA for OFDM-based radar has been designed and studied in [2]. To generate the OFDM signals with $N_c = 1024$ subcarriers, an IFFT operation with the length N_c has been performed. To do that, a total of ten radix-2 Cooley Tukey IFFT has been used and divided by inserting block RAM to each second radix-2. Finally, five pipeline groups can be formed as shown in Fig. 6.6. In order to prevent an overflow (of bits) in a fixed-point FFT design, an indexed-

	Bit vector	Decimal value	Loss in amplitude [dB]
H1]	[1010101011]	683	33
	[1010101010]	682	30
	[0110101010]	426	27
	[0101101010]	362	24
	[0101011010]	346	21
	[0101010110]	342	18

Table 6.1.: Available scaling factor for 1024 IFFT and the corresponding loss in amplitude

scaling method has been implemented for pipelined FFT processors. When the IFFT is performed in one stage, the pre-stored data from the previous IFFT stage in the memory are scaled and output to the next FFT stage. The scaling bit stream consists of 10 bits as $[N_4, N_3, N_2, N_1, N_0]$ with N_x representing 2 binary bits. N_x is the scaling factor for group 'x'. For example, if group 1 has the scaling factor $N_1 = (10)_2 = (2)_{10}$ then the value of IFFT calculation is shifted 2 bits which is equivalent to the division of that value by a factor of $2_2 = 4$. This method is good for preventing overflow in memory. However, when the scaling value is large, it also leads to a great reduction in the amplitude of the output signals.

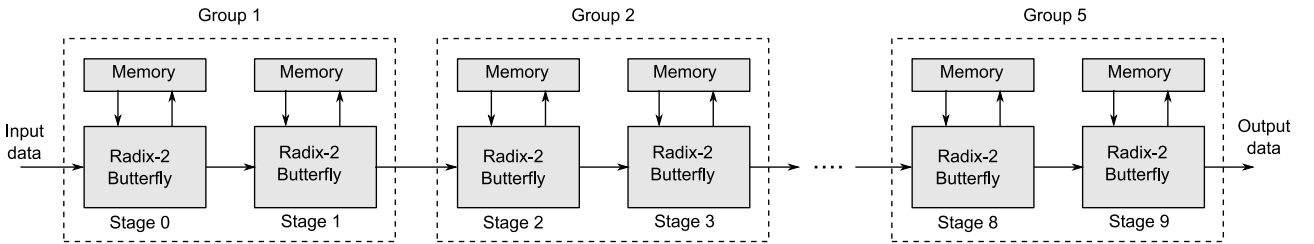


Fig. 6.6.: The scaling index of IFFT

Table 6.1 shows the available bit vector in the FPGA and the corresponding loss in amplitude of the output signal due to the bit vector scaling factor. The loss in the amplitude also leads to a reduction in the total output power of the output signal.

6.2.1. Measurement for the Signals from the FPGA

In this part, the measurement for the signal from FPGA for one transmitter is conducted. The input parameters of the FPGA is shown in Table 6.2. The OFDM signal has only one symbol without CP therefore the time duration of one symbol is $T_{sym} = 10.24 \mu s$. The I and Q signal after the DACs are measured by an oscilloscope and a spectrum analyzer as shown in Fig. 6.8. The digital I and Q signals generated by the FPGA are passed through the DACs to generate analog I and Q signals. The IFFT scaling factor as mentioned previously must be set to be at least 346 in order to avoid an overflow.

Symbol	Parameter	Value
N_c	Number of subcarriers	1024
N_{sym}	Number of symbols	256
Δf	Subcarrier spacing	97.656 kHz
T	Elementary OFDM symbol duration	$10.24 \mu s$
T_{CP}	Cyclic prefix duration	$1.28 \mu s$
T_{sym}	Transmit OFDM symbol duration	$11.52 \mu s$
B	Total signal bandwidth	100 MHz

Table 6.2.: MIMO OFDM-based system parameters

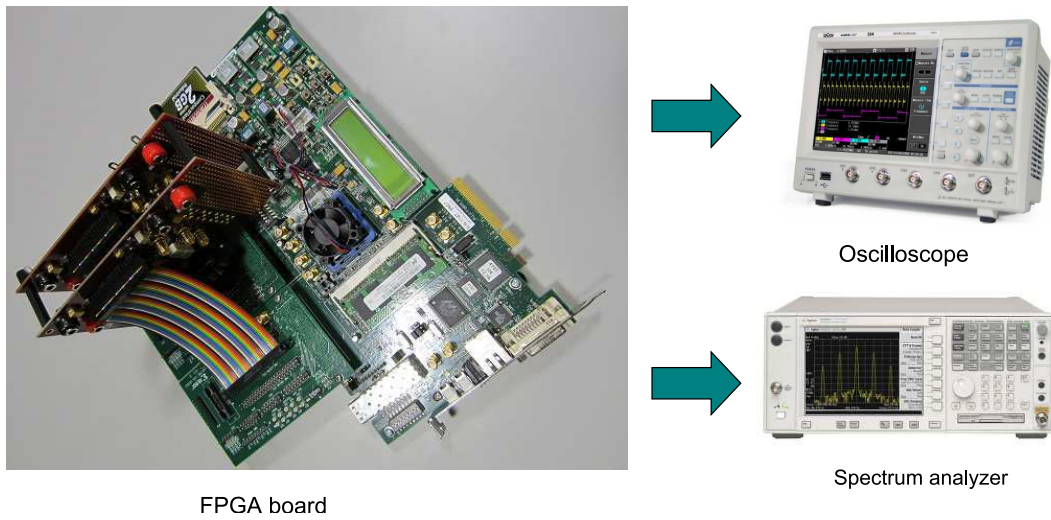


Fig. 6.7.: Measurement setup to measure the signals generated by the FPGA

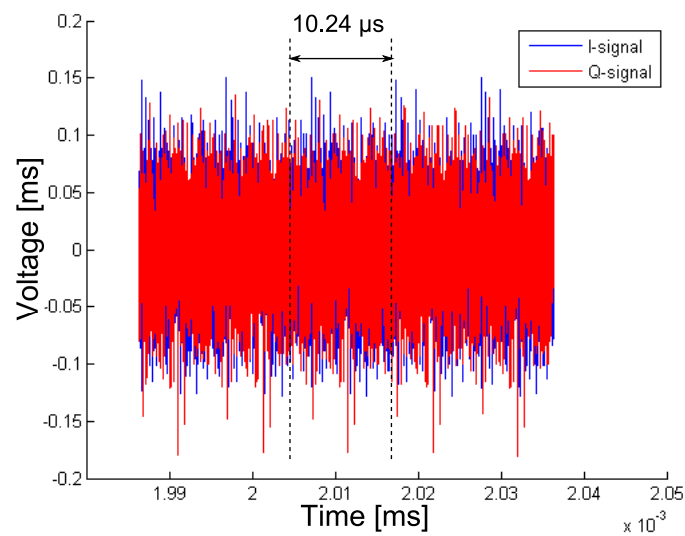


Fig. 6.8.: The I and Q signals from the FPGA in time domain

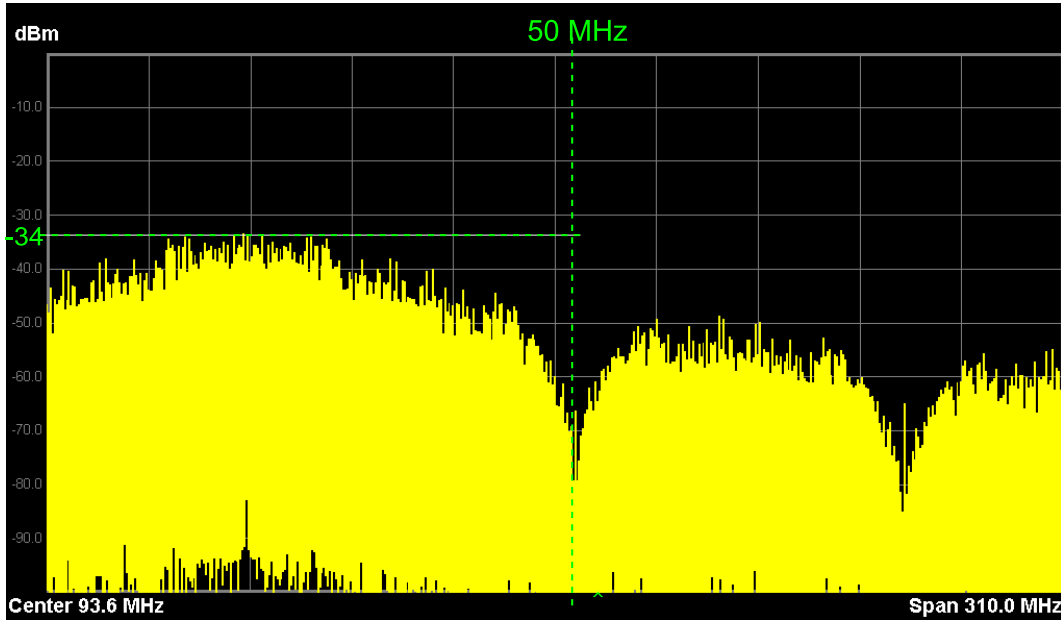


Fig. 6.9.: The OFDM spectrum measured from the spectrum analyzer

The I and Q signals after the DACs are then represented in time domain in Fig. 6.8. The OFDM symbols are sent repeatedly and continuously. There is a repetition of every $10.24 \mu\text{s}$ in the time-domain I and Q signals, which is the time duration of one OFDM symbol. The spectrum of the OFDM signal is shown in Fig. 6.9. Since no oversampling is implemented in the FPGA, the OFDM spectrum is shaped by the hold function of the DAC as described in section 5.2. The spectrum near the frequency 50 MHz degrades because of the multiplication of the OFDM spectrum with the $\sin x/x$ function, which is the frequency response of the hold function of the DAC. In addition, the images due to aliasing from the out-of-band signals also fall into the band of interest. The output power at a specific frequency is lower than -34 dBm , which is relatively low.

One OFDM symbol is then extracted from the measured data taken at the oscilloscope and put in Matlab. A correlation operation between the original signal generated from Matlab and the measured data is done. The QPSK modulation symbols are then recovered by implementing the IFFT process. Fig. 6.10 shows the scatter plot of the recovered QPSK symbols in the baseband. One cloud represents one group of QPSK modulation symbols. The clouds stretch in one direction because of the interference of the images (which have lower amplitudes than the signals at the band of interest) at the multiples of Nyquist sampling. In this case, the Nyquist sampling is $f_s = 100 \text{ MHz}$. The recovered QPSK symbols are then implemented as the input QPSK symbols for the MIMO radar system simulation as described in chapter 3.

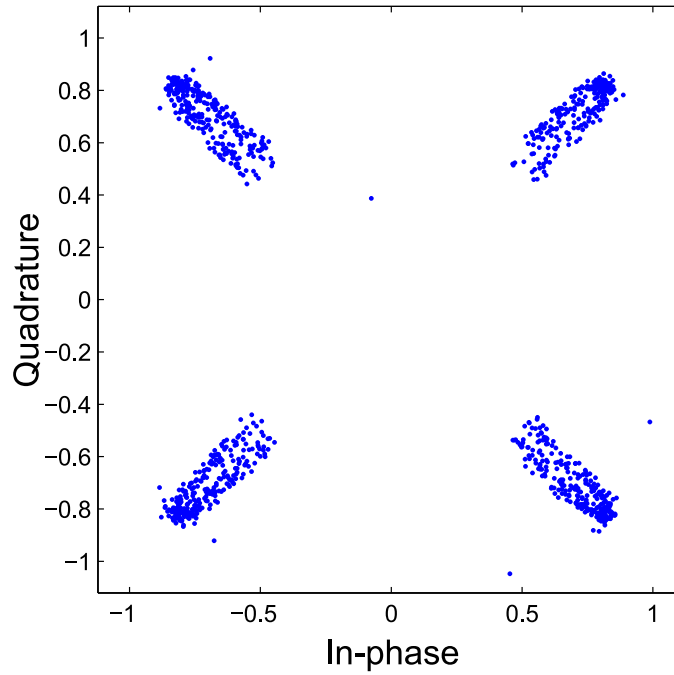


Fig. 6.10.: The scatter plot of the transmitted QPSK symbols in baseband

3D Radar Imaging with the Signals from the FPGA

Consider now an $8\text{Tx} \times 8\text{Rx}$ MIMO radar system, where the antenna geometry are arranged as mentioned in 3.3.2. The element spacing of transmit and receive array is chosen to be $d_T = d_R = \lambda/2$. The objects are listed in Table 4.1 in section 4.3.2 and the $\text{SNR} = 5\text{ dB}$ at the receiver. The signal from the FPGA (DAC output) is put into Matlab and these signals are processed with the spectral masks for 8 transmitters to separate the signals. These signals are then put through the MIMO OFDM system simulation as described in chapter 3.

After applying the MUSIC algorithm as described in section 4.1, the radar image is shown in Fig. 6.11. It shows clearly two objects A and B but the other objects are not clearly shown. In addition, there are a lot of random peaks in the MUSIC spectrum due to the wrong detection of objects.

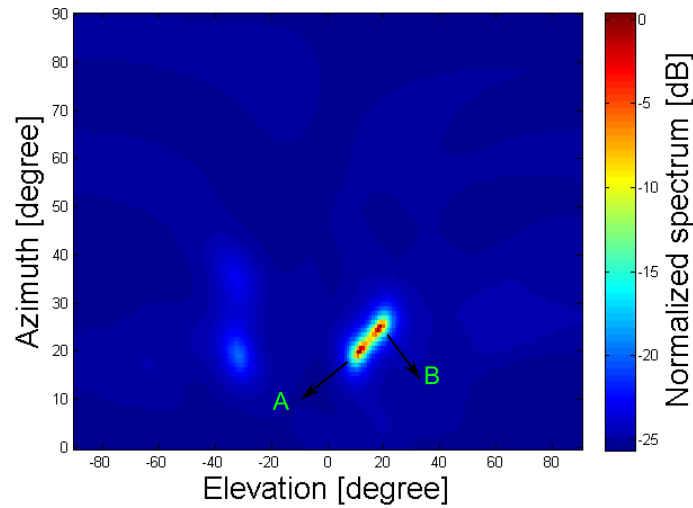


Fig. 6.11.: The 3D radar image using the signal generated from the FPGA

6.2.2. Measurement of The Signal Generated by FPGA for Multiple Transmitters

For the MIMO radar system, the spectrally interleaved multi-carrier signals as described in section 3.4 is used with the parameters listed in table 6.2. The total 1024 subcarriers are distributed among the 4 transmitters/subchannels. Therefore, there are only 256 subcarriers per subchannels. When generating the signal for 4 transmitters, the IFFT scaling factor must set to be at least 426 to avoid an overflow.

Fig. 6.12 shows the I and Q signals from transmitter 1 in the time domain. As discussed in section 6.3, the IFFT scaling vector leads to a reduction in the amplitude of the analog I and Q signals. The average peak amplitude is around 0.03 V. The spectrum for an OFDM signal with sideband suppression of 16 subcarriers per side (equivalent to the deduction of 1.56 MHz per side). The peak output power is -63 dBm

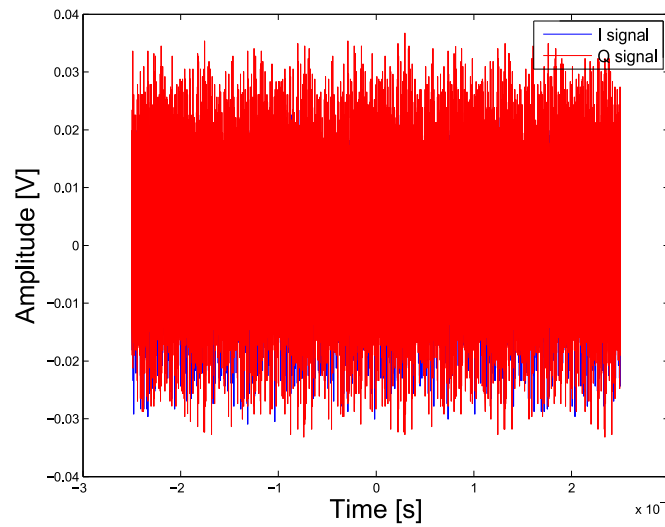


Fig. 6.12.: The I and Q signal from transmitter 1 (out of 4 transmitters)

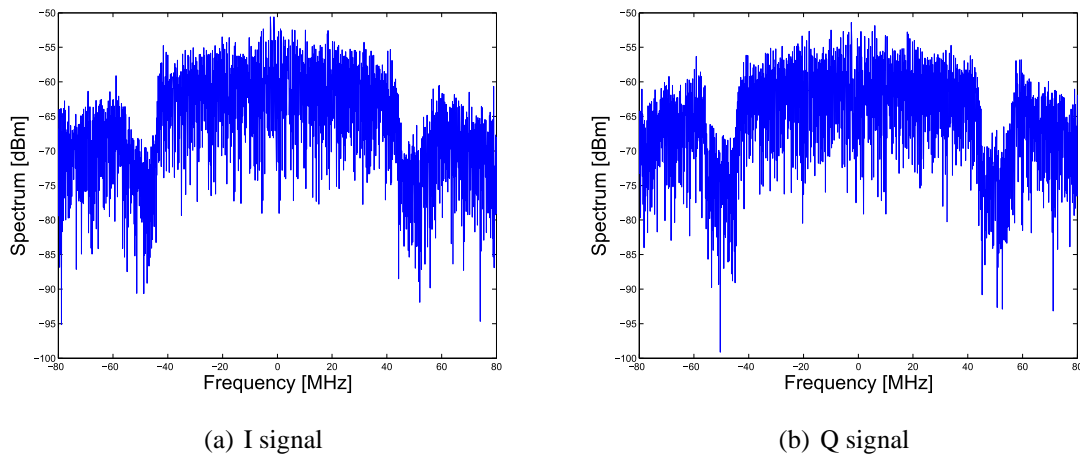


Fig. 6.13.: Spectrum of I and Q analog signals for transmitter 1

One OFDM symbol is then extracted from the measured data taken at the oscilloscope in Matlab by a correlation operation between the original signal generated from Matlab and the measured data. The QPSK modulation symbols are then recovered by implementing the IFFT. Fig. 6.14 shows the scatter plot of the signal transmitted from transmitter 1. It can be seen that the QPSK symbols can not be recovered and the scatter plot shows a noise-like signal. This might be due to the scaling factor which reduces the amplitude too much for the signals to be correctly recovered.

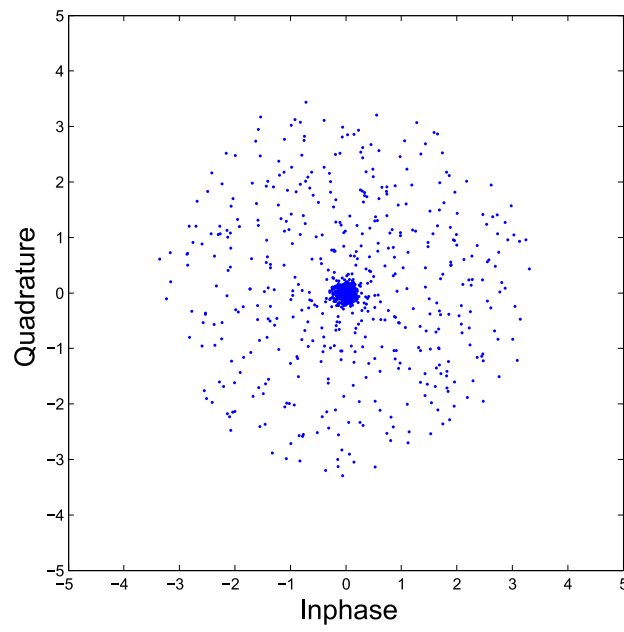


Fig. 6.14.: The scatter plot of one OFDM symbol from transmitter 1

7. Conclusion

The main goals of this thesis were to implement an DOA estimation algorithm for 2D and 3D Radar Imaging and also to build a RF frontend to integrate with the FPGA (designed in another work) and verify the radar imaging algorithm, several works have been done.

The first main work was to investigate in the MIMO radar concept. A general model for MIMO radar was derived for a better understanding of MIMO radar. The fundamentals of the OFDM-based SISO radar system RadCom were represented. The novel radar processing has been discussed. The functionality of this system has been proved. The arbitrary antenna geometry have been analyzed to give a set of general equations for later analysis. After that, the 2D antenna geometry has been discussed. Since the application for automotive radars have been changing over time, the information of elevation angle is required. To estimate the elevation angle, the antenna geometry has been extended to a simple geometry in which the receive and transmit arrays are orthogonal to each other. Finally, in order to send uncorrelated signal, the signal modification from the original OFDM signal in RadCom system was represented. The parameters for MIMO radars were calculated and analyzed.

The second main work, the DOA estimation algorithms has been studied. Among them, we chose the most promising one, MUSIC algorithm. A MIMO radar system has been implemented in Matlab, including transmitter, receiver, channel model and the radar processing unit. The system parameters are adjustable in all components. At the radar processing unit, MUSIC algorithm with virtual steering vector was successfully applied. The results for two cases, first, 2D radar and then 3D, are shown and analyzed for different scenarios. The performance of the MUSIC algorithm for 2D and 3D radar is good for an $\text{SNR} \geq -10$ dB. The separation of objects in both azimuth and elevation angle are 5° separable in 2D radar and 14° separable in 3D radar. Its performance is also influenced by a number of parameters such as the SNR, the number of antenna elements, the antenna geometry of receive and transmit antennas. However, the noise statistics must be measured or characterized analytically in order to set the sufficient threshold to detect objects.

The third main work was the realization of hardware for RF front end and measurement. The transmitter with direct conversion architecture was considered based on its simplicity and cost. Inverse Chebyshev LPFs have been designed, fabricated and measured to suppress the images caused by the DACs. The theory of DACs, PLL synthesizer and I/Q upconverter were studied. A 4:1 Wilkinson divider is built to feed the LO signal from the PLL synthesizer to 4 I/Q upconverter.

The inverse Chebyshev LPF at 50 MHz was designed to suppress the image after to suppress the images after the DAC processing. Since the signal of interest occupies almost the entire bandwidth up to $f_s/2$, where f_s is the sampling rate of the DAC, the requirements for a steep roll-off LPF with cutoff frequency ω_c after each DAC to suppress the images in other Nyquist zones are critical. The inverse Chebyshev lumped-element LPF is decided because three reasons: first, the ripple in the stop band is not important, second, it requires less lumped elements than other types of filter and third, the microstrip filter is not suitable at this operating frequency. The LPF was designed in ADS Agilent and was fabricated. It was shown in measurement to have a steep roll-off. The filter characteristics for the simulated and measured results have a difference of 3 MHz due to the non-ideal lumped elements. Since the FPGA can perform carrier suppression to adjust the bandwidth, the designed LPF are sufficient for the current usage.

The 4:1 Wilkinson power divider was designed to feed the LO signal into the I/Q upconverter. Its design was based on the transmission line theory. The dimension of the circuit was taken into account for the soldering of the four SMA output ports. The power divider was simulated in ADS and fabricated on substrate Roger4003C. The measured return loss has a shift of approximately 600 MHz in the resonance frequency from the simulated result. The cause of the shift is due to the nonlinear change of the dielectric constant of the substrate at high frequencies and the coupling between transmission line of the circuit which cannot be modeled correctly by ADS. However, for the use at 12.075 GHz, the result is sufficient. The insertion loss at 12.075 GHz is -8.8 dB. This means that it is 2.2 dB lower than the simulated insertion loss. In order to provide a 3 dBm LO signal to each I/Q modulator, a low noise power amplifier with gain 5 dB is required to amplify the LO signal before passing through the Wilkinson divider.

The measurement for the PLL frequency synthesizer at $f_r = 12.075$ GHz was conducted. Since the prescaler frequency f_r is $f_r = 6037.5$ MHz, the spurs are actually the harmonics at f_r and appear in the output signals due to the leakage in the VCO. From the measured data, since the spurs generated by the PLL synthesizer have low output power, their interference to the band of interest is negligible. The measured phase noise for 10 kHz is -76.7 dBc/Hz, which can be considered low and sufficient for current use.

The measurement for one whole transmitter was conducted with the signal source from a signal generator. The spectrum of the output signals are discussed. The intermodulation products between the OFDM signals and the LO leakage signals are shown in the measurement results. The upconverted OFDM signal has the output power of -10 dBm before passing the antenna. Due to the unclear of the output power from the FPGA, a power amplifier after the I/Q modulator may be needed.

Finally, the measurement for the signal generated by the FPGA for two cases, for one transmitter and four transmitters, are conducted. For the case of one transmitter, the QPSK symbols were successfully recovered however, the group of one modulation symbol in the scatter plot stretches

out in one direction due to aliasing. The output power of the OFDM signal is below -34 dBm, which is relatively low. This due to the IFFT scaling factor designed in the FPGA. The baseband signal generated by the FPGA was analyzed in Matlab for radar processing. For the case of four transmitters, a higher IFFT scaling factor has to be set. This leads to a significant reduction in the output power of the output signal from one transmitter (-63 dBm). The scatter plot shows a noise-like signal. Therefore more analysis needs to be done to the FPGA before integration with the RF frontend can be done.

Overall, the goals of designing the superresolution algorithm for 2D and 3D radar imaging has been achieved. The 2D radar shows the ability to estimate the relative velocity along with the distance and azimuth angle. With the extension in the geometry of the transmit and receive antenna arrays, a 3D MIMO radar system has been realized with the capability to estimate one more parameter, the elevation angle. Due to the long processing time, the velocity estimation for the 3D case was not demonstrated in this work. Nevertheless the current implemented algorithm is capable of estimating the velocity. The MUSIC algorithm has given a reasonable angular resolution for DOA estimation.

In addition, the signal separation technique in the RF frontend has also been demonstrated to work. As we mentioned in section 1.2, the full integration for the RF frontend might not be possible within this limited time frame, its analysis however is a step towards the integration of the whole MIMO OFDM radar system.

8. Future works

Listed below according to categories are some of the most important aspects.

8.1. Characteristics of MUSIC algorithms

First, MUSIC algorithm is sensitive to the position of antenna array. Thus, the array calibration must be taken carefully. For a real antenna array, a true steering vector $\tilde{\mathbf{v}}$ deviates from the ideal one \mathbf{v} . The real antenna array should be modeled as

$$\tilde{\mathbf{v}} = \mathbf{C}\mathbf{v} \quad (8.1)$$

where \mathbf{C} is a square calibration matrix. The method to estimate \mathbf{C} can be found in [12], [19]. The estimated calibration matrix $\hat{\mathbf{C}}$ is then can be used to correct the steering vector in MUSIC algorithm. In addition, for antenna arrays, mutual coupling between antenna elements can degrades the performace of array signal-processing algorithms. A calibration is also required to process the mutual-coupling compensation.

Secondly, MUSIC is based on the assumption that the signal subspace and noise subspace are orthogonal. However, in practice, when multipath propagation occurs, instead of line-of-sight signals, the non LOS ones, which are correlated with the wanted signals, also arrives at the receivers. This leads to a wrong DOA estimation. The solution for that is based on a preprocessing scheme referred as spatial smoothing which can decorelates the signals and eliminates the effect of coherent signals to DOA estimation. The studies for spatial smoothing is introduced in [16]. A ray-tracing scenario can be implemented to have a set of data which is close to the real data.

Finally, a study of the threshold to detect objects in real scenarios, such as on highway, can be studied to improve the performance of MUSIC algorithm.

8.2. Improvement for FPGA prototype

First of all, oversampling should be implemented on the FPGA. Fig. 8.1 shows the comparison between Nyquist sampling and oversampling. Nyquist rate simply defines the minimum rate at which the signal has to be sampled so that it can be reconstructed successfully. In this project, the baseband bandwidth is $B/2 = 50$ MHz and the sampling rate is $f_s = 100$ MHz. This setup leads to a great degradation of the signal near the edge of 50 MHz because of the multiplication of the signal

and the transfer function of the DAC, $\sin x/x$, in the frequency domain. In addition, the OFDM signal also suffers from the aliasing interference. In the case of Nyquist sampling, the requirement of a low pass filter is critical. Oversampling, on the other hand, increase the sampling rate of the signal significantly. The oversampling factor can be an integer or rational fraction greater than unity (so-called "upsampling"). It can be shown that a higher sampling rate to relax the transition band requirements for analog low pass filter. Moreover, it also reduced the baseband quantization noise power and improves the resolution.

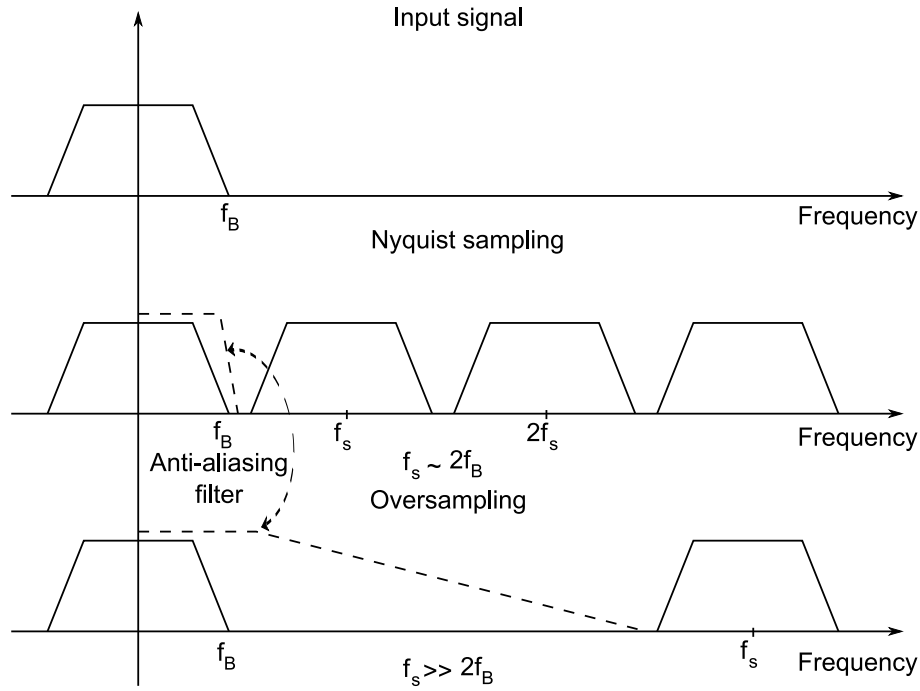


Fig. 8.1.: Nyquist sampling vs. Oversampling

However, after the implementation of oversampling in FPGA, new DACs with higher sampling rate are also needed. Secondly, the scaling method to avoid overflow in the calculation of IFFT can be studied more since it reduces significantly the output power of the baseband signals.

8.3. Measurement for MIMO radar

The design of receiver can be investigated. After that, the FPGA will be integrated the full RF front end and take the measurement with the patch antennas.

A. Mathematical Notations

A.1. Dot Product

The dot product of two vectors $\mathbf{a} = [a_1, a_2, \dots, b_n]$ and $\mathbf{b} = [b_1, b_2, \dots, b_n]$ is defined as:

$$\mathbf{a} \cdot \mathbf{b} = \sum_{i=1}^n a_i b_i = a_1 b_1 + a_2 b_2 + \dots + a_n b_n \quad (\text{A.1})$$

where n is the dimension of the vector space.

A.2. Kronecker Product

The Kronecker product, denoted by \otimes , is an operation on two matrices of arbitrary size resulting in a block matrix. If \mathbf{A} is an $m \times n$ matrix and \mathbf{B} is a $p \times q$ matrix, then the Kronecker product $\mathbf{A} \otimes \mathbf{B}$ is the $mp \times nq$ block matrix:

$$\mathbf{A} \otimes \mathbf{B} = \begin{bmatrix} a_{1,1}\mathbf{B} & a_{1,2}\mathbf{B} & \cdots & a_{1,n}\mathbf{B} \\ a_{2,1}\mathbf{B} & a_{2,2}\mathbf{B} & \cdots & a_{2,n}\mathbf{B} \\ \vdots & \vdots & \ddots & \vdots \\ a_{m,1}\mathbf{B} & a_{m,2}\mathbf{B} & \cdots & a_{m,n}\mathbf{B} \end{bmatrix} \quad (\text{A.2})$$

A.3. Hermitian Transpose

An Hermitian matrix is a square matrix with complex entries that is equal to its own conjugate transpose. The Hermitian transpose of \mathbf{A} is denoted by \mathbf{A}_H . It is obtained by taking the transpose and then taking the complex conjugate of each entry.

$$(\mathbf{A}^*)_{i,j} = \overline{\mathbf{A}_{ji}} \quad (\text{A.3})$$

where the subscripts denote the i, j -th entry, and the overbar denotes a scalar complex conjugate.

A.4. Positive Semidefinite Hermitian Matrix

An Hermitian matrix is a square matrix with complex entries that is equal to its own conjugate transpose. This means that the element in the i -th row and j -th column is equal to the complex

conjugate of the element in the j -th row and the i -th column, for all indices i and j .

$$a_{ij} = \bar{a}_{ji} \quad (\text{A.4})$$

A Hermitian matrix is positive-semidefinite if and only if all of its eigenvalues are non negative. Considering a $n \times n$ Hermitian matrix \mathbf{M} , it said to be postive-semidefinite if

$$\mathbf{x}^* \mathbf{M} \mathbf{x} \geq 0 \quad (\text{A.5})$$

for all matrix $\mathbf{x} \in \mathbb{C}^3$, where \mathbf{x}^* is the conjugate transpose of \mathbf{x} .

B. Circuits

B.1. PCB for LPF

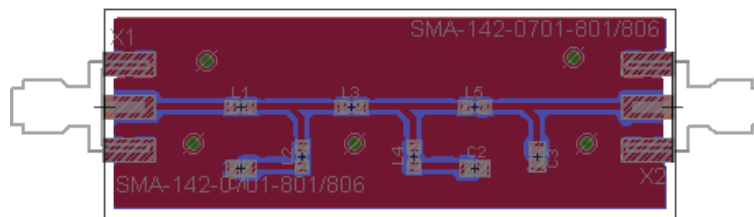


Fig. B.1.: Layout for LPF

B.2. Schematic for Wilkinson power divider

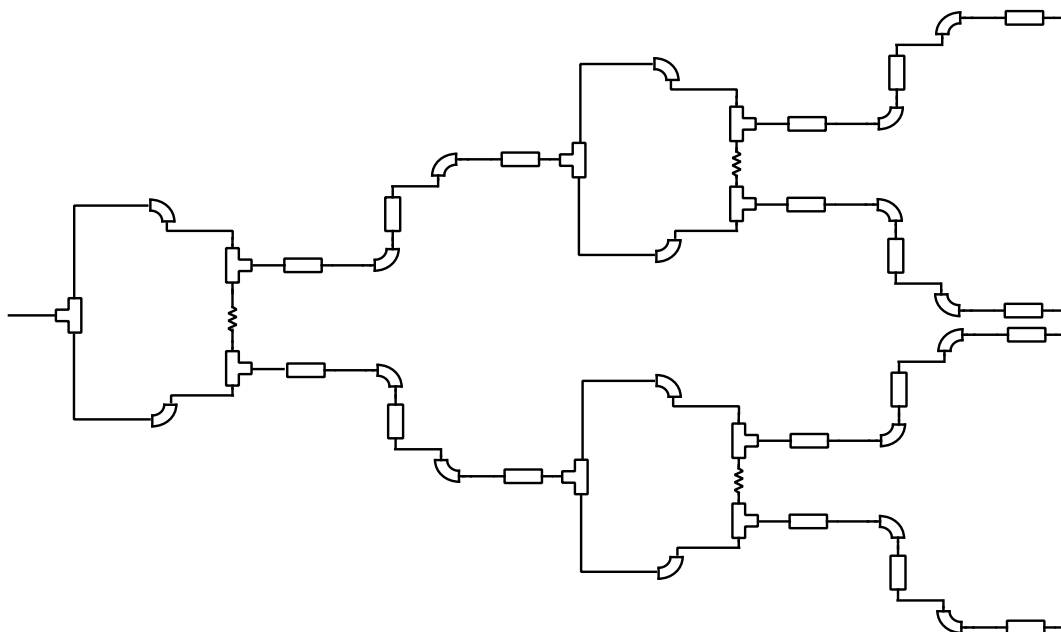


Fig. B.2.: Schematic for Wilkinson power divider

Bibliography

- [1] M. Abramowitz and I. A. Stegun. *Handbook of Mathematical Functions: with Formulas, Graphs, and Mathematical Tables*. Dover Publications, 1965.
- [2] Johannes Baier. Analysis and Design of an FPGA-based OFDM Transmitter for MIMO Radar Application, 2012.
- [3] C.A. Balanis. *Antenna Theory*. John Wiley & Sons, Inc, New York, 1997.
- [4] Chun-Yang Chen. *Signal processing algorithms for MIMO Radar*. PhD thesis, Department of Electrical Engineering, California Institute of Technology, 2009.
- [5] E. Fishler, A. Haimovich, R. Blum, D. Chizhik, L. Cimini, and R. Valenzuela. MIMO Radar: an idea whose time has come. *Proceedings of the IEEE Radar Conference*, pages 71–78, April 2004.
- [6] K.W Forsythe, D.W. Bliss, and G.S. Fawcett. Multiple-input multiple output (MIMO) radar: performance issues. *Conference on Signals, Systems and Computers*, 1:310–315, November 2004.
- [7] Qizheng Gu. *RF system design of transceivers for wireless communications*. Springer, 2005.
- [8] European Telecommunications Standards Institute. Intelligent transport systems.
- [9] J. Li and P. Stoica. MIMO Radar with Colocated Antennas. *IEEE Signal Processing Magazine*, 24:106–114, September 2007.
- [10] M. Marlene, S. Shameem, A. Andreas, and Z. Thomas. Realization of an innovative 3D imaging digital beamforming radar system. *2011 IEEE CIE International Conference on Radar*, 1:186–189, October 2011.
- [11] Richard van Nee and R. Prasad. *OFDM for wireless multimedia communications*. Artech House, 2000.
- [12] J. Pierre and M. Kaveh. Experimental performance of calibration and direction-finding algorithms . *International Conference on Acoustics, Speech, and Signal Processing, ICASSP*, 2:1365–1368, 1991.
- [13] David M. Pozar. *Microwave Engineering*. Wiley, 2005.
- [14] T.S. Rappaport and J. Liberti. *Smart Antennas for Wireless Communications: IS-95 and Third Generation CDMA Applications*. Prentice Hall, 1999.
- [15] P. Robertson and S. Kaiser. Analysis of the effects of phase-noise in orthogonal frequency division multiplex (OFDM) systems . *IEEE Conference on Communications*, 3:1652–1657, June 1995.
- [16] Tie-Jun San, M. Wax, and T. Kailath. On spatial smoothing for direction-of-arrival estimation

- of coherent signals . *IEEE Transactions on Acoustics, Speech and Signal Processing*, 33:806–811, August 1985.
- [17] R. Schmidt. Multiple emitter location and signal parameter estimation . *IEEE Transactions on Antennas and Propagation*, 3:276 – 280, March 1986.
 - [18] Karin Schuler. *Intelligente Antennensysteme für Kraftfahrzeug-Nahbereichs-Radar-Sensorik*. PhD thesis, Forschungsberichte aus dem Institut für Höchsthfrequenztechnik und Elektronik der Universität Karlsruhe (TH), 2007.
 - [19] C. M. S. See. Sensor array calibration in the presence of mutual coupling and unknown sensor gains and phases. *Electronics Letters*, 30:373–374, March 1994.
 - [20] L. Sit, C. Sturm, L. Reichardt, T. Zwick, and W. Wiesbeck. The OFDM Joint Radar-Communication System: An Overview. *SPACOMM 2011, The Third International Conference on Advances in Satellite and Space Communications*, April 2011.
 - [21] Y. L. Sit, C. Sturm, J. Baier, and T. Zwick. Direction of Arrival Estimation using the MUSIC algorithm for a MIMO OFDM Radar. *IEEE Radar Conference*, May 2012.
 - [22] M. I. Skolnik. *Introduction to Radar Systems*. McGraw-Hill, 1962.
 - [23] C. Sturm, M. Braun, T. Zwick, and W. Wiesbeck. A multiple target doppler estimation algorithm for OFDM based intelligent radar systems. *European Radar Conference (EuRAD)*, October 2010.
 - [24] C. Sturm, M. Braun, T. Zwick, and W. Wiesbeck. Performance verification of symbol-based OFDM radar processing . *IEEE Radar Conference (EuRAD)*, May 2010.
 - [25] C. Sturm and T. Zwick. *Smart Antennas for Wireless Communications: IS-95 and Third Generation CDMA Applications*. Patent DE 10 2011 009 874, Jul 2001.
 - [26] C. Sturm, T. Zwick, and W. Wiesbeck. An OFDM System Concept for Joint Radar and Communications Operations. *IEEE Vehicular Technology Conference*, 2009.
 - [27] Christian Sturm. *Gemeinsame Realisierung von Radar-Sensorik und Funkkommunikation mit OFDM-Signalen*. PhD thesis, Forschungsberichte aus dem Institut für Höchsthfrequenztechnik und Elektronik der Universität Karlsruhe (TH), 2011.
 - [28] Texas Instruments (TI). Fractional/Integer-N PLL Basics, August 1999.
 - [29] Texas Instruments (TI). Dual, 14-bit, 125MSPS Digital-to-Analog Converter, October 2009.
 - [30] Mac E. VanValkenburg. *Analog filter design*. Holt, Rinehart and Winston, 1982.
 - [31] E.J. Wilkinson. An N-Way Hybrid Power Divider. *IRE Transaction on Microwave Theory and Techniques*, 8:116–118, January 1960.

Thanh Thuy Nguyen**Master Thesis: Design and Analysis of Superresolution Algorithm and Signal Separation Technique for an OFDM-based MIMO Radar****Zeitraum: 01.05.2012 – 31.10.2012****Betreuer: Prof. Dr. -Ing. Thomas Zwick , Prof. Dr. Antonio Broquetas****Abstract:**

Recently, the concept of MIMO (multiple-input multiple-output) radar has been proposed. MIMO radar has the capability to transmit orthogonal (or incoherent) waveforms at multiple transmit antennas. It offers promising potentials for resolution enhancement, interference suppression and against multipath fading. Many research about MIMO radar in signal processing have been conducted. However, the implementation of MIMO radar in practice is still uncommon. In this thesis, the SISO (single-input single-output) OFDM radar and communication system (RadCom), a previous project at Institut für Hochfrequenztechnik und Elektronik (IHE), KIT, Germany, is extended to MIMO configuration using the idea of spectrally interleaved multi-carrier signals to estimate the direction of arrival (DOA) of objects in 2D and 3D radar. The main aim of this thesis is to implement and evaluate a MIMO OFDM-based radar system.

The thesis consists of two parts, the software and hardware part. In the first part of the thesis, the MIMO radar is studied. A signal modeling is derived along with the analysis of suitable antenna geometries for 2D and 3D radar. The MIMO radar with the ability to form virtual array can increase significantly the resolution of DOA estimation. For that purpose, numerous algorithms based on different mathematical approaches exist. The numerical results show that the MUSIC (Multiple Signal Classification) algorithm based on subspace method is simple to implement and have good resolution. We combine the OFDM-based signal model with MUSIC to perform 2D and 3D radar sensing. The DOA estimation with MUSIC along with the simulation results are presented.

The second half of this thesis focuses on the realization of the hardware design for MIMO radar systems. A RF frontend for four transmitters with direct conversion architecture was considered. One transmitter includes 2 low pass filters (LPFs), an Inphase/Quadrature (I/Q) upconverter, a phase-locked loop (PLL) frequency synthesizer, a 4:1 Wilkinson power divider. Inverse Chebyshev LPFs at 50 MHz with lumped elements were built and measured. In addition, a sufficient 4:1 Wilkinson divider was simulated and fabricated to feed the local oscillator (LO) signal into the I/Q upconverters. The other individual elements of the transmitter was measured and analyzed. Several measurement have been taken to test one whole transmitter. In addition, the signals generated by

the FPGA, which is planned to integrate with the transmitters, are analyzed.

Postanschrift: Institut für Hochfrequenztechnik und Elektronik
Kaiserstraße 12
D-76131 Karlsruhe

Gebäude: Engesserstraße 5, Geb. 30.10

Tel.: +49 (0) 721 608 4 2522
Skr.: +49 (0) 721 608 4 2523
Fax: +49 (0) 721 608 4 5027
E-Mail: info@ihe.kit.edu
Web: www.ihe.kit.edu

